

^{10}Be in polar ice cores and ^{14}C in tree rings: Separation of production and system effects, comparison with past climate changes and implications for solar physics

A dissertation submitted to
ETH ZÜRICH

for the degree of
DOCTOR OF SCIENCES

presented by
Abreu Castiñeira José Ángel
Licenciado en Ciencias Físicas, University of Vigo
born in March 24, 1976
citizen of Galiza, Spain

accepted on the recommendation of
Prof. Dr. Jürg Beer, examiner
Prof. Dr. Antonio Ferriz Mas, co-examiner
Prof. Dr. Stefan Brönnimann, co-examiner
Prof. Dr. Werner Schmutz, co-examiner

2009

Abstract

Understanding the Sun's magnetic activity is important because of its impact on the Earth's environment. The sunspot record since 1610 shows irregular 11-year cycles of activity; they are modulated on longer timescales and were interrupted by the Maunder minimum in the 17th century. Recent activity has been abnormally high for at least 8 cycles: is this grand maximum likely to terminate soon or even to be followed by another (Maunder-like) grand minimum? Cosmogenic radionuclides stored in natural archives such as ^{10}Be in ice cores and ^{14}C in tree rings have proven to be very useful in reconstructing past solar activity, and changes in the geomagnetic field intensity over many millennia. At present, this is the only method to extend the records of solar activity proxies beyond the instrumental period. To answer the previous questions we use, as a measure of the Sun's open magnetic field, a composite record of the solar modulation potential ϕ , reconstructed principally from the record of cosmogenic ^{10}Be abundances in the GRIP ice core from Greenland. However, the cosmogenic radionuclide signal contains also a climate component introduced by the transport of the radionuclides from the atmosphere to the archive where they are stored. In order to employ cosmogenic radionuclides in astrophysical or climate studies, first these two components must be separated. Fortunately, theory shows that the response of ^{10}Be and ^{14}C systems to climate variations is very different. Thus comparing both radionuclides makes it possible to distinguish between climate induced variations and solar/geomagnetic ones. In this work, we apply PCA (Principal Component Analysis) to ^{10}Be from ice cores as well as to ^{14}C from tree rings in order to isolate and remove the climate effects in the records. In this way ^{10}Be and ^{14}C become much better tools for climate as well as for astrophysical applications, for instance in form of solar modulation potential ϕ . The ϕ composite used in this work extends back for almost 10,000 years, showing many grand maxima and grand minima. We carry out a statistical analysis of this record and calculate the life expectancy of the current grand maximum. We find that it is only expected to last for a further 15–36 years¹, and we therefore predict a decline in solar activity within the next two or three cycles. In addition, we also estimate the probability that the current grand maximum will be followed by a (Maunder-like) grand minimum. The spectral analysis of the solar modulation potential ϕ reveals strong modulation at well defined periods, namely ~ 2200 , 980 and 200. Comparison of the afore mentioned open-flux proxies with sunspots, points to the existence of a magnetic threshold below which, the sunspots do not reach the solar surface. We suggest two separate full dynamos operating in two separate layers. The possible decoupling between both dynamos could be the explanation for activity minima such as the Maunder minimum.

¹Starting in 2004, hence, 2019-2040 A.D.

Zusammenfassung

Die Sonnenaktivität zu verstehen ist wichtig, da sie ein wichtiger Antreiber für das Klima der Erde ist. Die gemessene Anzahl der Sonnenflecken seit 1610 weist einen unregelmässigen 11-Jahreszyklus auf. Dieser Zyklus variiert auch auf längeren Zeitskalen und war sogar im 17. Jahrhundert während des Maunder-Minimums unterbrochen. Hingegen war die Sonnenaktivität während der letzten acht 11-Jahreszyklen aussergewöhnlich hoch. Es stellen sich also die Fragen: Wann wird die momentane Phase hoher Aktivität zu Ende gehen? Was passiert danach? Kommt im Anschluss ein Maunder Minimum?

Kosmogene Radionuklide, gespeichert in natürlichen Archiven wie, z.B., ^{10}Be in Eisbohrkernen und ^{14}C in Baumringen, können verwendet werden, um einerseits die Vergangenheit der letzten Jahrtausende der Sonnenaktivität und andererseits der Erdmagnetfeldstärke zu rekonstruieren. Zur Zeit ist das die einzige verfügbare Methode, um direkte Proxydaten (wie Sonnenflecken) der Sonnenaktivität vor der Beobachtungsperiode zu erweitern. Um die obigen Fragen zu beantworten, wird in dieser Arbeit als Proxy für das offene solare Magnetfeld ein Datensatz des solaren Modulationspotentials verwendet. Dieser Datensatz wurde aus ^{10}Be Konzentrationen gemessen im GRIP Eisbohrkern ermittelt. Das im Eisbohrkern enthaltene Signal besteht jedoch nicht nur aus einer solarer Komponente, sondern auch aus einer klimatischen Komponente. Diese klimatische Komponente wird aufgrund des Transports der Radionuklide von der Atmosphäre zum Archiv (z.B. Eisbohrkerne oder Baumringe) verursacht. Um kosmogene Radionuklide in Astrophysik so wie in Klimauntersuchungen anwenden zu können, müssen folglich zuerst diese zwei Komponenten voneinander getrennt werden. Die Theorie zeigt, dass die durch Sonnenvariabilität verursachten Produktionsänderungen sich auf ^{10}Be und ^{14}C gleich auswirken. Klimaänderungen (Systemeffekte) dagegen drücken sich in den ^{10}Be und ^{14}C Daten verschieden aus. Der Vergleich beider Nuklide erlaubt es, das Produktionssignal von den Systemeffekten zu trennen; diese Trennung erfolgt mit Hilfe der "Hauptkomponentenanalyse". Das abgetrennte Klimasignal ermöglicht, die systematische Identifizierung der Klimaänderungen im Holozän. Ein detaillierter Vergleich des solaren Signals wie auch des klimatischen Signals mit verfügbaren Klimadaten sollte es ermöglichen, Rückschlüsse auf den Einfluss der Sonnenaktivität auf das Klima zu ziehen. Durch die Eliminierung der klimatischen Komponente, wird eine realistischere Rekonstruktion des solaren Modulationspotentials ermöglicht, wobei ein wertvoller Proxy für die Sonnenaktivität zur Verfügung steht. Der in dieser Arbeit verwendete Datensatz des solaren Modulationspotentials geht mehrere Jahrtausende zurück. Deutlich zu sehen sind das Auftreten grosser solarer Minima (wie das Maunder Minimum) und grosser solarer Maxima (wie die jetzige Zeit). In dieser Arbeit wurde eine statistische Auswertung der Zeitreihe durchgeführt. Damit konnte die Lebenserwartung des momentan grossen solaren Maximum abgeschätzt werden. Es wird erwartet, dass es innerhalb von 15-36 Jahren zu Ende geht. Daraus wird gefolgert, dass Sonnenaktivität innerhalb der nächsten zwei Zyklen abnehmen wird. Eine weitere Auswertung erlaubt eine Voraussage über das Auftreten des nächsten Maunder Minimum.

Hier wird erwartet, dass rund um das Jahr 2100 ein grosses solares Minimum auftreten wird. Der Vergleich von Daten von kosmogene Radionukliden und Sonnenflecken deutet auf zwei unterschiedliche Dynamos in der Sonne hin. Wir stellen die Hypothese auf, dass es die Auskopplung zwischen diese zwei Dynamos, die Ursache für Grosse Minima ist.

Contents

1	Introduction	13
2	^{10}Be and ^{14}C as a tool to study climatic variability and solar activity	15
2.1	The production of cosmogenic radionuclides	17
2.2	^{10}Be and ^{14}C	21
2.3	Natural archives	22
3	Timescale of EDML Ice Core	31
3.1	EDML Ice Core	31
3.2	Synchronization by means of tree rings	31
4	The EDML Accumulation rate	37
4.1	Introduction	37
4.2	Accumulation	37
4.3	Conclusions	39
5	^{10}Be in ice cores and ^{14}C in tree rings: Separation of production and climate effects	41
5.1	Introduction	41
5.2	^{10}Be and ^{14}C systems	42
5.2.1	The production of cosmogenic radionuclides	42
5.2.2	^{10}Be and ^{14}C in the climate system	42
5.2.3	The data	43
5.3	Separation of production and system effects using PCA	44
5.4	Results	44
5.5	Conclusions	46
6	From ^{10}Be in ice to solar activity	49
6.1	The <i>force field parameter</i> ϕ and the <i>modulation function</i> Φ	49
6.2	^{10}Be Production rate as a function of geomagnetic field and solar activity . .	51
7	For how long will the current grand maximum of solar activity persist?	53
7.1	Introduction	53
7.2	The Solar Modulation Function from the GRIP ^{10}Be Record	56
7.3	Statistical Analysis	57
7.4	Conclusion	60

8	Can we forecast the next grand minimum in solar activity?	61
8.1	Introduction	61
8.2	Long-term modulation of solar solar activity	62
8.3	Statistical analysis	63
8.4	A solar dynamo model: Data interpretation in the framework of dynamo theory.	64
8.5	Conclusion	66
9	Conclusion and Outlook	75
9.1	Conclusion	75
9.2	Outlook	75
A	Influence of the residence time on the amplitude and the phase of the production signal	77
B	Basics on <i>Principal Component Analysis</i> (PCA), definitions and notation	81
B.1	Properties of the Principal Components	83
C	Error estimation for Paper: Grand maxima in solar activity	85
C.1	Measurement error & fit error	85
C.2	conclusions	87
	Bibliography	90
	Acknowledgements	97
	Curriculum Vitae	99

List of Figures

2.1	Change of the solar constant relative to today's value expressed in percent. In order to produce this figure we used formula 2.4 along with Berger's reconstruction of the Earth's past eccentricity (Berger & Loutre 1991).	18
2.2	Histogram of the relative change of the solar constant to today's value. The relative change of the solar constant takes values in the interval $[0, 0.16]$ in the last 5 Myr. This interval was divided into 100 subintervals before the frequency of each subinterval was calculated.	18
2.3	Comparison of the calculated eccentricity by Berger & Loutre (1991) with the SPECMAP $\delta^{18}\text{O}$ record (Imbrie 1993).	19
2.4	Composite of the evolution of the total solar irradiance for the period 1979–2000, as measured by radiometers on board of different satellites (Fröhlich 2000).	20
2.5	Average monthly Sunspots Number since 1750 (<i>e.g.</i> , http://sidc.oma.be/sunspot-data/)	21
2.6	^{10}Be and ^{14}C radionuclides in the Earth's system. This picture depicts the similarities and differences between ^{14}C and ^{10}Be systems. <i>Similarities</i> : Both radionuclides are produced in the same way, modulated by the Sun and Earth's magnetic fields. <i>Differences</i> : As a consequence of different geochemical behaviours, after production ^{10}Be becomes attached to aerosols and is removed from the atmosphere after a mean residence time of 1 to 2 years, while ^{14}C enters the carbon cycle. Therefore, climate changes influence the two radionuclides differently.	23
2.7	Ring widths of trees growing in the same area display common patterns. By matching these patterns from different trees, a dendrochronology can be constructed. Figure from: http://www.ncdc.noaa.gov/paleo/treering.html	25
2.8	Vertical axis shows ^{14}C activities. Horizontal axis shows time in years BP (where 1950 is taken as origin of times). $A(t)$ is the specific activity of ^{14}C in the atmosphere (green line). The black horizontal line corresponds to $A(0)$. t_d is the so-called true age, that is the actual age of the sample. t_r is the radiocarbon age and represents the age that a sample would have if the atmospheric ^{14}C content had always been $A(0)$ and $T_{1/2}^{(1)}$ 5568 years. $S_1(t) = A(t_r)e^{-\lambda_1(tr-t)}$ is the law of radioactive decay assumed by the dating laboratories. $S_2(t) = A(t_d)e^{-\lambda_2(td-t)}$ represents the true decaying law with the true half-life equal to $T_{1/2}^{(2)}$ equal to 5730 years. Note that formula 2.7 is a particular case for $S_1(t)$ with $t = 0$	27
2.9	Atmospheric $\Delta^{14}\text{C}$ against calendar years (errors indicated by vertical red lines) from tree rings (Hughen <i>et al.</i> 2004).	29

2.10	Relationship between radiocarbon age and true age (also dendro age or calendar ages). This curve consists mainly of decadal tree ring measurements (Hughen <i>et al.</i> 2004). The green line depicts the relationship between radiocarbon and calendar years if the concentration of ^{14}C had remained constant in the past and equal to the standard value of 1950.	29
3.1	^{10}Be (raw data) concentration and ^{14}C production rate normalized. A binomial filter of grade 31 was applied.	32
3.2	The ^{10}Be and ^{14}C data after applying the wiggle matching dating method (time scale 1).	34
3.3	The same ^{10}Be data set synchronized by two different persons for the interval 2500-3000 BP.	35
3.4	This plot represents the difference between the two times scales against time scale 1. The choice of time scale 1, rather than time scale 2 as a reference was arbitrary. For most points the differences are smaller than 40 years.	35
4.1	Estimation of EDML accumulation rate based on the time scale 1.	39
4.2	Estimation of EDML accumulation rate based on the time scale obtained by Beer.	40
5.1	a: $\Delta^{14}\text{C}$ (Per mil) as measured in tree rings. b: Standardized (<i>i.e.</i> , subtracting the mean, then dividing by the standard deviation) of ^{14}C production rate calculated from $\Delta^{14}\text{C}$ (Per mil) by using a carbon cycle model. c: Standardized ^{10}Be concentrations (GRIP ice core) after being linearly interpolated to 1 year and low-pass filtered with a cutoff 40 years. d: Standardized ^{10}Be fluxes (GRIP ice core) after being linearly interpolated to 1 year and low-pass filtered with cutoff 40 years.	46
5.2	Standardized time series of ^{10}Be and ^{14}C data after being linearly interpolated to 1 year, resampled with 10 years, and low-pass filtered with a cutoff 40 years. Here we only depict the interval 4400 to 5800 BP to show the structure of the data.	47
6.1	Global ^{10}Be production rate against Earth's magnetic field (relative to present value) and solar modulation ϕ . We normalized the production rate by assuming the production rate = 1, for the magnetic field = 1 and the solar activity $\phi = 550$ MV.	52
7.1	Records of solar activity. (a) Timeseries for ϕ constructed from the GRIP ice-core and filtered to eliminate the 11 year Schwabe cycle (Vonmoos <i>et al.</i> 2006). (b) Composite timeseries showing the modulation potential ϕ , after compensating for the use of different Local Interstellar Spectrum (LIS) models (Steinhilber <i>et al.</i> 2008). Shown are the smoothed annual means of ϕ from the GRIP ice-core – red), from the South Pole (green), and the annual means from direct measurement of cosmic rays.	55
7.2	(a) Section of the filtered composite timeseries for the modulation potential ϕ , after imposing a 3000 year high pass filter and a 40 year low-pass filter. (b) Probability distribution for the measured values of the modulation potential ϕ , compared with a normal distribution. The data are normally distributed about a mean 477.8 MV and standard deviation 174 MV.	58

7.3	Distribution of the durations of grand maxima in activity. (a) Scatter plot for durations of grand maxima, listed consecutively back in time. Note that there are only two examples with durations longer than that of the current grand maximum. (b) Binned distribution for durations of grand maxima. Superimposed are the fitted gamma (green) and lognormal (red) distributions. (c) Scatter plot relating the level of a grand maximum in ϕ (as ordinate) to that of the subsequent relative minimum. Grand minima lie to the left of the heavy vertical line. No significant correlation is visible in the data	59
8.1	Records of solar activity. The green curve shows the composite of the solar modulation potential ϕ (Steinhilber <i>et al.</i> 2008). Shown in red is the NGRIP data (Berggren <i>et al.</i> 2009) after being linear interpolated to 0.4 y and smoothed with binomial filter over 61 points. The dash-dotted blue curve shows the ^{14}C production rates, while the solid blue curve depicts the sunspot numbers.	68
8.2	Band-pass filtered ^{10}Be fluxes from NGRIP ice core (Berggren <i>et al.</i> 2009). The solid blue curve depicts the sunspot numbers.	69
8.3	The red curve shows the time evolution of the long-term in solar modulation potential ϕ and is given by the superposition of the three most significant frequencies found in the spectral analysis (Table 8.1) (standardized data). The blue curve shows the ϕ composite. The two horizontal green lines correspond to the maximum/minimum levels used to define a grand maximum/minimum as explained in the text.	70
8.4	Same as Fig. 8.3 but covering the entire time span of ϕ to show the long-term modulation.	71
8.5	An extrapolation into the future of the fitted long-term curve. It shows that mean level activity will reach levels similar to the <i>Little ice age</i> around 3500. Note the decrease in recent dates around 2107.	72
8.6	Binned distribution for waiting times between grand minima. Superimposed is the fitted gamma (green) distribution.	73
A.1	Relative change of ^{14}C production rate and $\Delta^{14}\text{C}$ against time. The red line depicts a sinusoidal production rate with a periodicity of 300 years. The blue line represents the corresponding atmospheric $\Delta^{14}\text{C}$, which was calculated using a carbon cycle model. The original amplitude is very strongly attenuated. In addition, the $\Delta^{14}\text{C}$ curve is delayed by ~ 25 years.	79
A.2	Relative change of ^{14}C production rate and $\Delta^{14}\text{C}$ against time. The red line depicts a sinusoidal production rate with a periodicity of 10 years. The blue line represents the corresponding atmospheric $\Delta^{14}\text{C}$, which was calculated using a carbon cycle model. The atmospheric amplitude is even more strongly attenuated than in the previous figure. The $\Delta^{14}\text{C}$ curve is delayed ~ 3 years. Note the different scales. . .	79

A.3	Relative change of ^{10}Be production rate and atmospheric ^{10}Be concentration against time. The red line depicts a sinusoidal production rate with a periodicity of 10 years. An atmospheric residence time of 2 years for ^{10}Be was assumed. The blue line represents the corresponding atmospheric ^{10}Be concentrations. It can be observed how the amplitude of the atmospheric ^{10}Be concentration is attenuated and delayed by ~ 2 years. However, these two effects for ^{10}Be concentrations are less important than for the ^{14}C concentrations.	80
A.4	Relative change of ^{10}Be production rate and atmospheric ^{10}Be concentration against time. The red line depicts a sinusoidal ^{10}Be production rate with a periodicity of 300 years. The blue line represents the corresponding atmospheric ^{10}Be concentration. There are no significant differences between the amplitudes.	80
C.1	Blue points represents the best gamma fit with parameters (a,b). Red curves A and B represents the corresponding gamma distributions by taking as parameters the extreme values (1.6, 9) and (3, 18.8) respectively. The solid green curve, was obtained by assuming that the $\phi(t)$ measurement errors are normal distributed. The black error bars depict the $1-\sigma$ deviations (see explanation in text)	86
C.2	Blue points depict $\bar{r}(t_0)$ and red error bars depict $\Delta r(t_0)$ for each run	88
C.3	Distribution of remaining times corresponding to the gamma distribution. The parameters of gamma distribution $a \in [1.60, 3.02]$ and $b \in [9.18, 18.79]$ were assumed to be lognormal distributed in their respective intervals. Here we took into account the fit errors only	89

List of Tables

2.1	Cosmogenic radionuclides which are produced in the atmosphere along with main target elements, the half-life, the estimated mean global production rates and the total global inventories (from Masarik & Beer 1999). The corresponding inventories were calculated from this data assuming steady state conditions.	22
5.1	$\alpha_{i,j}$, $R(C_j, X_i)^2$ and λ_i before synchronization	45
5.2	$\alpha_{i,j}$, $R(C_j, X_i)^2$ and λ_i after synchronization.	45
8.1	First nine most dominant spectral lines obtained from the spectral analysis of ϕ . The period, phase and amplitudes were estimated by using Bayesian probability theory as described in Bretthorst (1988b). This table illustrates that the solar activity is modulated on longer time scales than the eleven year cycle. The three first lines are the main contributors to the long-term oscillation in the ϕ time series. They were used to generate the red curve in Fig. 8.4 and Fig. 8.5. The last line is the Gleissberg cycle which is also seen in the sunspots record.	67
B.1	Matrix of data	81

Chapter 1

Introduction

^{10}Be stored in ice cores is the central object of study in the present work. It belongs to the so called cosmogenic radioisotopes. As their name points out (from Greek *kosmos*, world, universe and *gen-*, *genēs*, born of a specified kind), they are produced when high energetic cosmic ray particles collide with the atoms of the Earth's atmosphere. Shortly after production, ^{10}Be becomes attached to aerosols and after a residence time of 1-2 years it is removed from the atmosphere by precipitation and some ^{10}Be is finally stored in natural archives, for instance, in polar caps. Its production depends on the level of solar activity as well as the geomagnetic field intensity. As a consequence, ^{10}Be in ice cores has the potential to provide us with valuable information about past solar activity, and the history of the Earth's magnetic field. Because of its long half-life (1.5 million years), ^{10}Be record extends thousands of years back in time, which exceeds by far the time span covered by direct proxies of solar activity. Direct observation of solar activity, in the form of sunspots, began with the invention of the telescope in 1609. Before this date, we must rely on proxies data. In addition, ^{10}Be abundances preserved in ice cores, also contain a climatic component. This is due to the influence of the climate on the transport from the place of production in the atmosphere to the ice cores. Fortunately, the climate during the Holocene (last 10.000 years) has been relatively stable, and therefore the climate component constitutes a minor contribution compared with the production component. Nevertheless it is important to separate these components to correctly interpret them separately and therefore learn about the past solar activity, the climate and the possible relationship between them, for instance the role played by the Sun in past climate changes. This, of course, may help to understand the present climate change because understanding the past may be the key to predict the future. The various manifestations of the solar activity is an area of intensive research, not only because of its connection with the Earth's climate, but also because of its inherent importance for solar physics. Understanding the processes taking place below the solar surface, for obvious reasons, are inferred mainly from theoretical models¹. The information derived from ^{10}Be can, therefore help to constrain that models. Chapter 2 gives an introduction to cosmogenic isotopes. Their production, their transport through the Earth system are described. They are considered as a tool to study climatic variability and solar activity. Chapter 3 gives an introduction to the problematic of ice core dating. Since the ^{14}C data were dendrochronologically dated, the ^{14}C time scale is used as the reference to calibrate the ^{10}Be data set from GRIP ice core by Wiggle-Match Dating.

¹Helioseismology, however represents an exception. This tool allows for monitoring the physical processes taking place within the sun, in the same way that seismologists learn about the Earth's interior by monitoring waves caused by earthquakes

In chapter 4 two estimates of the accumulation rate from EDML are presented. It is found that these values deviate very little from the average accumulation rate for EDML for the last 6000 years BP provided by the EPICA project. Therefore, it is assumed in next chapters that, as a first approximation, the accumulation rate for EDML during the Holocene can be regarded as constant. In chapter 5 the method of *Principal Component Analysis* (PCA) will be employed to decompose the ^{10}Be from two ice cores (EDML and GRIP), as well as ^{14}C data from tree rings, into a *production signal* and a *system signal*. The *production signal* represents the common production rate for both isotopes, ^{10}Be and ^{14}C , while the *system signal* represents the environmental effect on each nuclide. Since cosmogenic radionuclides are often used in solar activity reconstructions, it is crucial to eliminate the climate component to allow a better interpretation of the reconstructed solar activity indices. In chapter 5 it is shown that PCA is an adequate tool to achieve that goal. Chapter 6 introduces the *force field parameter* ϕ (also known as solar modulation potential). The concept of force field parameter arises from a simplified version of the transport equation (Gleeson & Axford 1968) and describes the modulation of the galactic cosmic rays by the solar wind. Since in the present work the *force field parameter* is used as a proxy for solar activity, chapter 6 provides the reader with some basic concepts to facilitate the comprehension of subsequent chapters. Chapters 8 and 9 are devoted to applications. Recent solar activity has been abnormally high for at least 8 cycles. In chapter 8 a statistical analysis of a 10000 years ϕ record is carried out that enables us to estimate the duration of the current grand maximum in solar activity. It is expected to last for further 15–36 years. In chapter 9 we follow a similar approach to predict the likelihood of a subsequent grand minimum. It is found that the solar activity will reach a minimum within the next 80–100 years. In this chapter we interpret our data in the framework of dynamo theory and hypothesize about the possible origin of grand minima.

Chapter 2

^{10}Be and ^{14}C as a tool to study climatic variability and solar activity

In order to make the text more readable, the following basic concepts are defined at the beginning:

- **The solar constant**, S ; is the power collected at the top of the atmosphere at an average distance of 1 AU¹ by a surface of unit area perpendicular to the energy flow. Historically it was assumed to be a constant.
- **The spectral solar irradiance**, $I(\lambda)$; is the electromagnetic energy flux across a surface of unit area at the top of the Earth's atmosphere at an average distance of 1 AU at a given wavelength per unit wavelength (λ is the wave length).
- **The total solar irradiance**, I_{TS} ; is the spectral solar irradiance integrated over all wavelengths.

Since it was found that the solar constant is not a “constant”², the question of how solar variability is related to climatic variability has become an important issue in climatic research. In this work, cosmogenic radionuclides are used as a tool to find a possible connection between climatic changes and changes in solar activity. In this chapter a brief explanation is given of what cosmogenic radionuclides are, how they are produced and how they can be used to learn about the Earth's climate and the Sun's variability. When modelling a complex system such as the climate system, one important parameter to be taken into account is the energy input. In the case of the present Earth, the Sun is by far the most important source of energy which drives the climate system. Useful concepts related to the solar constant are the **spectral solar irradiance** and the **total solar irradiance**. The *total solar irradiance* was assumed to be constant, but when radiometers outside of the atmosphere (*i.e.*, satellite based) began to monitor the solar constant, small changes of about 0.1 % from the minimum of solar activity to the maximum were discovered (Fröhlich & Lean 2004). Is, however, such a small change enough to affect the climate noticeably? In order to address this question let us introduce first the concept of feedback. The climate is constantly adjusting to forcing perturbations, and while it adjusts, the climate varies. The climate system can be considered as consisting of different interlinked subsystems. A change in any part of the climate system

¹Astronomical Unit, equal to the mean distance between Earth and Sun; *i.e.*, 149.596 10⁹ m.

²Reliable and continuous measurements of the total solar irradiance started in 1978 (Willson *et al.* 1981).

will have an effect on the other parts. As the effect is transferred from one sub-component of the system to another, the effect will be modified. In some cases it may be amplified (*positive feedback*), while in others, it may be reduced (*negative feedback*). A short introduction to climatic feedback concepts can be found in Peixoto & Oort (1992). The following example illustrates how a small change in the radiative forcing can perceptibly affect the climate. One source of variation of the total energy entering the Earth system is the change in the eccentricity of the Earth's orbit, which occurs with a periodicity of approximately 100 kyr (Hays *et al.* 1976). This forcing can be accurately calculated because it is based on celestial mechanics. In order to work out the change in the solar constant due to this forcing, we take into account that:

1. The Earth's orbit is described by

$$r(\nu) = a \frac{1 - e^2}{1 + e \cos \nu}, \quad (2.1)$$

where r is the distance between the Sun and the Earth, e is the eccentricity of the Earth's orbit, ν is the angle between the vector Sun-Perihelion and vector Sun-Earth and a is the mean distance between Sun and the Earth.

2. We estimate the solar constant at the point r of the orbit as

$$S(e, \nu) = S(0) \left[\frac{a}{r(\nu)} \right]^2, \quad (2.2)$$

where $S(0)$ ($= 1365 \text{ Wm}^{-2}$) is the estimated value of the solar constant for today's eccentricity.

3. We take into account *Kepler's Second Law*, *viz.*

$$r^2(\nu) \frac{d\nu}{dt} = \text{const.} \quad (2.3)$$

4. We calculate the average of the solar constant over all angles ν , keeping e constant, as follows:

$$\langle S(e) \rangle = \frac{\int_0^{2\pi} S(0) \left(\frac{a}{r(\nu)} \right)^2 r^2(\nu) d\nu}{\int_0^{2\pi} r^2(\nu) d\nu} = \frac{S(0)}{(1 - e^2)^{\frac{1}{2}}}. \quad (2.4)$$

In Fig. 2.1 we see our reconstruction of the changes of the solar constant relative to today's value³. As can be seen in Fig. 2.1, the relative change remains smaller than 0.16 % (in Fig. 2.1 we plotted only the interval 0 to 2000 kyr BP), which can also be seen in Fig. 2.2, where the corresponding histogram of relative frequencies is displayed. The histogram shows that most of the time the solar constant was smaller than 0.16 % because most of the time the orbit was almost circular.

³This estimation is based on the reconstruction of the eccentricity by Berger & Loutre (1991) for the last 5 Myr BP.

Although this forcing seems to be very small, we see that the 100 kyr frequency can be observed during the last 600 kyr in most paleoclimate records (Fig. 2.3). In Fig. 2.3 it is apparent how the $\delta^{18}\text{O}$ ⁴ data set displays a dominant periodicity of 100 kyr. This may indicate that small changes in the energy input must be amplified by feedback processes.

Therefore, through such feedback processes, a change of 0.1% in the solar constant can be amplified and may induce large changes in climate. In addition, studies of historical data show that solar forcing indeed has played an important role in past and present climate change (Beer *et al.* 2000). For example, there is growing evidence that periods of low solar activity such as the Maunder minimum (1645 to 1715 A.D.) coincide with relatively cool periods, and therefore point to a causal relationship between solar variability and climate. On the other hand, satellite based measurements of the solar irradiance for the last 20 years have shown that the solar constant varies in phase with the sunspots record (see Fig. 2.4 and 2.5). Since the primary energy source of the Earth is of solar origin and this energy input is almost exclusively in form of electromagnetic radiation, solar effects on the climate are usually thought to be connected with changes in the solar irradiance. Moreover, one has to take into account that while changes in the total solar irradiance within one solar cycle amount to approximately 0.1%, measurements of the spectral composition of the solar radiation show that the amplitude of the change in the ultraviolet part of the spectrum between the minimum and maximum of the solar cycle is much larger than the change in the total irradiance. Using data sets from the Solar Mesosphere Explorer (SME) and the Upper Atmosphere Research (UARS), Fröhlich & Lean (2004) show that the UV radiation in the band from 160 nm to 208 nm varies by an order of magnitude more than the total solar irradiance. In this context, a two-dimensional radiative-chemical-transport model was developed by Haigh (1994) in order to find the relationship between solar activity and the Earth's climate. This model shows that a highly non-linear relationship exists between the extraterrestrial and cross-tropopause solar radiative flux. It was found that an increase of 1 % in UV radiation at the peak of a solar activity cycle leads to strengthened stratospheric winds, to a poleward displacement of the tropospheric westerly jet streams, and to a relocation of the mid-latitude storm tracks. Therefore, we have to reconstruct solar irradiance as far back as possible and compare this data with paleoclimate records in order to study the connection between solar activity and climate. However, since there are no direct observational data to study the solar irradiance over such long periods of time, we have to rely on proxy data such as cosmogenic radionuclides.

2.1 The production of cosmogenic radionuclides

Cosmic rays are composed mainly of ionized nuclei, roughly 91 % protons, 8 % helium nuclei, and 1 % made up of heavier nuclei. When the highly energetic particles of galactic cosmic rays interact with N and O in the atmosphere, they generate a cascade of secondary particles.

⁴ $\delta^{18}\text{O}$ is the ratio of the stable isotopes $^{18}\text{O}/^{16}\text{O}$.

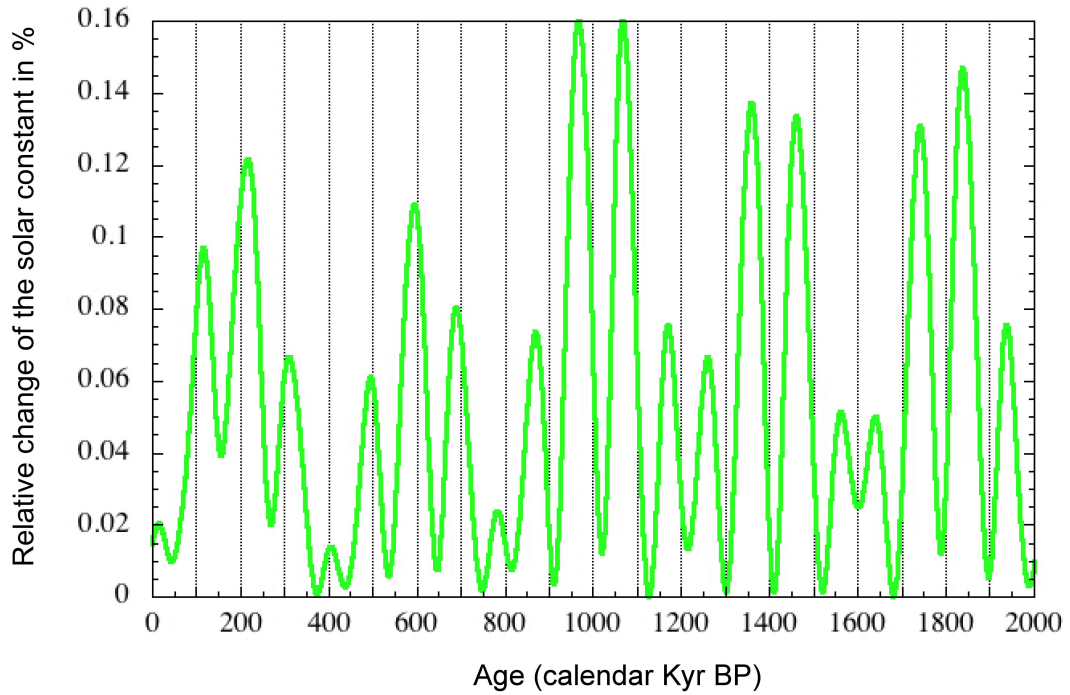


Figure 2.1: Change of the solar constant relative to today's value expressed in percent. In order to produce this figure we used formula 2.4 along with Berger's reconstruction of the Earth's past eccentricity (Berger & Loutre 1991).

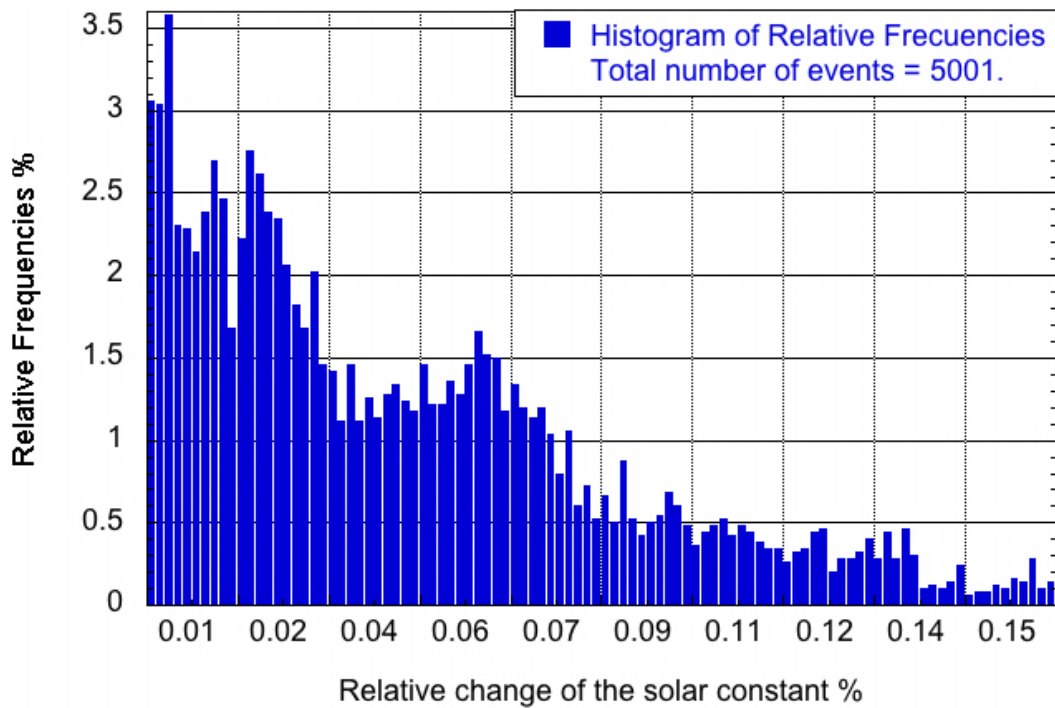


Figure 2.2: Histogram of the relative change of the solar constant to today's value. The relative change of the solar constant takes values in the interval $[0, 0.16]$ in the last 5 Myr. This interval was divided into 100 subintervals before the frequency of each subinterval was calculated.

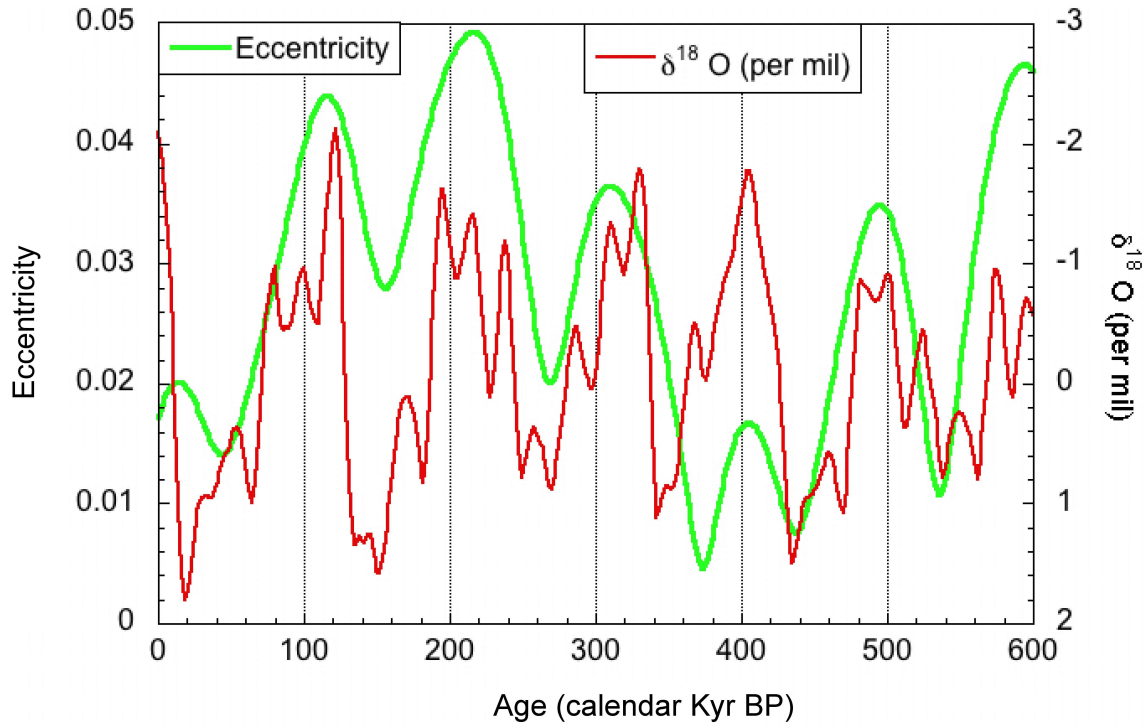
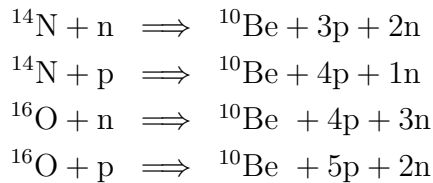
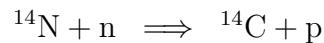


Figure 2.3: Comparison of the calculated eccentricity by Berger & Loutre (1991) with the SPECMAP $\delta^{18}\text{O}$ record (Imbrie 1993).

The following spallation reactions are responsible for the production of ^{10}Be and ^{14}C :



^{14}C is produced in the atmosphere by the interaction of thermal neutrons (*i.e.*, neutrons with energies less than 0.025 eV) with nitrogen, *viz.*



There are several processes which can change the production rate of cosmogenic radionuclides in the atmosphere *i.e.*, changes in the galactic cosmic ray flux, changes in solar activity and changes in the Earth's magnetic field (Masarik & Beer 2009). However, the analysis of meteorites shows that the intensity of the galactic cosmic rays has been constant $\pm 10\%$ (Vogt *et al.* 1990) on time scales of millions of years and therefore the main sources of variations are oscillations in solar activity and the Earth's magnetic field. Therefore, the records of cosmogenic radionuclides measured in natural archives can be interpreted in terms of solar activity, the Earth's magnetic field and, as will be shown in the next section, the climate system.

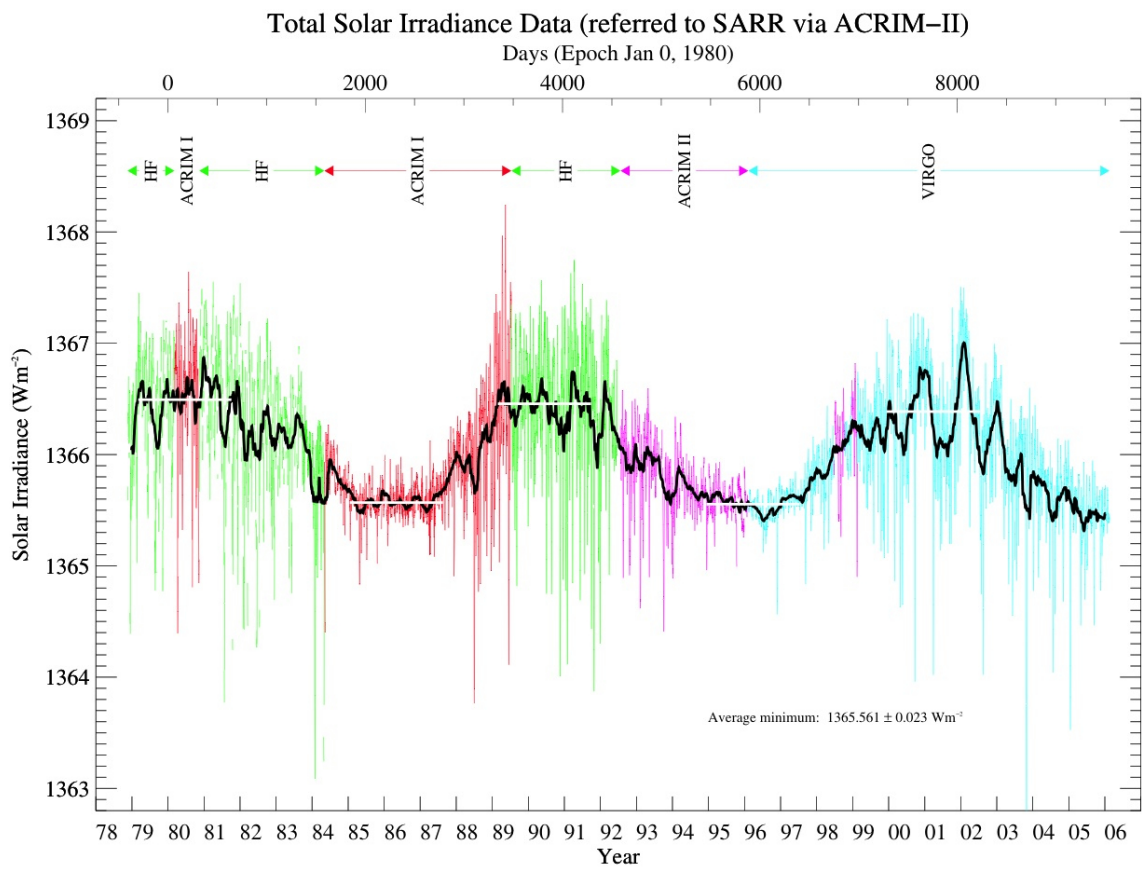


Figure 2.4: Composite of the evolution of the total solar irradiance for the period 1979–2000, as measured by radiometers on board of different satellites (Fröhlich 2000).

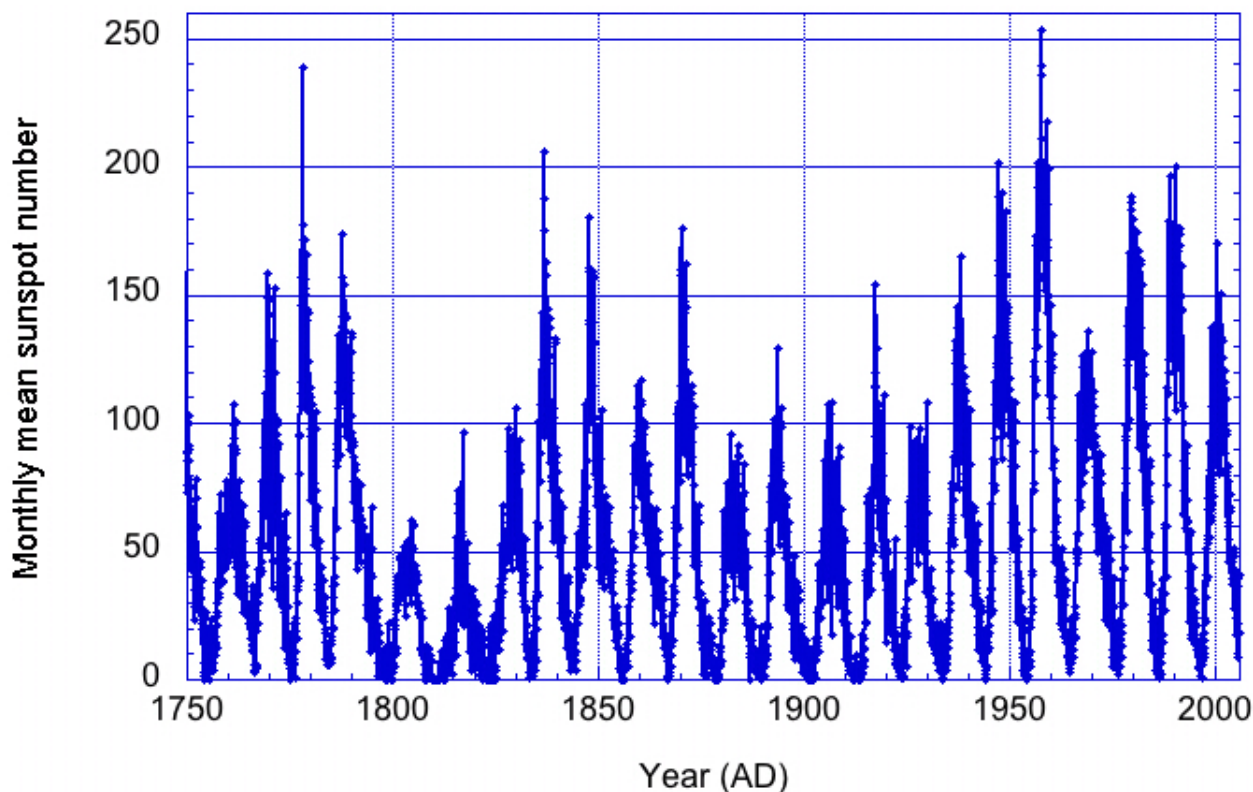


Figure 2.5: Average monthly Sunspots Number since 1750 (e.g., <http://sidc.oma.be/sunspot-data/>)

2.2 ^{10}Be and ^{14}C

In Table 2.2 some basic properties of the main cosmogenic radionuclides produced in the atmosphere are listed. The production rates are given as estimated mean global values. Based on these values, the global inventory can be estimated assuming steady state conditions.

^{14}C is optimal for dating organic material: it has a high production rate, a suitable half-life, it oxidizes to $^{14}\text{CO}_2$ and gets therefore involved in exchange processes among the atmosphere, the biosphere and the ocean, and has a long enough atmospheric residence time to be globally well mixed (the atmospheric residence time of ^{14}C is about 10 years). Due to these properties, the dating method based on ^{14}C can be uniformly applied throughout the world. In contrast, ^{10}Be has a very short atmospheric residence time (1 to 2 years) and it is stored in the geosphere. Therefore, the atmospheric ^{10}Be concentration reflects changes in production rate more directly than atmospheric ^{14}C concentrations; this is illustrated by means of a simple model of the atmosphere in appendix B.

All these properties make the two cosmogenic radionuclides a powerful tool to distinguish between production and system effects. By virtue of the similarities in the production rate of both radionuclides and of the different geochemical behaviours, ^{10}Be and ^{14}C records are composed of a production signal, which is common to both radionuclides, and a system signal, which in general is not a common signal (see Fig. 2.6).

Isotope	Target	Half-life	Production Rate	Inventory
			$[cm^{-2}s^{-1}]$	
^3H	N, O	12.4 y	0.28	4 kg
^7Be	N, O	53 d	0.035	0.0137 kg
^{10}Be	N, O	$1.5 \cdot 10^6$ y	0.018	104 tons
^{14}C	N	5730 y	2.02	62 tons
^{26}Al	Ar	$7.3 \cdot 10^5$ y	0.00014	1 tons
^{32}Si	Ar	145 y	0.00016	0.28 kg

Table 2.1: Cosmogenic radionuclides which are produced in the atmosphere along with main target elements, the half-life, the estimated mean global production rates and the total global inventories (from Masarik & Beer 1999). The corresponding inventories were calculated from this data assuming steady state conditions.

This can be represented as follows:

$$^{10}\text{Be signal} = \text{Production effects} + \text{System effects}_1$$

$$^{14}\text{C signal} = \text{Production effects} + \text{System effects}_2$$

This system is very complicated to solve due to the difficulties in evaluating the second terms on the right. Therefore global models showing how the climate system influences the ^{10}Be distribution around the world are needed in order to distinguish between the changes in ^{10}Be concentration caused by a change in the production rate, on the one hand, and changes caused by the climate system, on the other (*e.g.*, Heikkilä *et al.* 2008).

In Chapter 6 the method of *Principal Component Analysis* (PCA) was employed to separate the ^{10}Be data set from two ice cores as well as ^{14}C data set from tree rings, into a *production signal* and a *system signal*. The *production signal* represents the common production rate for both isotopes, ^{10}Be and ^{14}C , while the *system signal* represents the climate/environmental effects on each nuclide. Of course, in order to solve the system, there is always the possibility of using simplified equations instead of the original set by making certain assumptions about the behaviour of the two cosmogenic isotopes ^{14}C and ^{10}Be (an example is shown in Chapter 3).

2.3 Natural archives

In order to reconstruct the history of changes in production and system effects, archives providing the necessary information are needed. Fortunately, ice sheets and glaciers, on the one hand, and tree rings, on the other, turn out to be excellent natural archives for ^{10}Be and ^{14}C respectively. A very important aspect of all archives is dating: while tree rings can be dated accurately using dendrochronology, dating of ice cores is less straightforward. Since the accuracy of the dating is crucial for the discussion in the next section, we give here a brief description of the ^{14}C dating method.

Ice cores

Ice cores are extracted from ice sheets and glaciers. These are continuously formed by the snow accumulated yearly. While the thickness of the annual layers is reduced under the

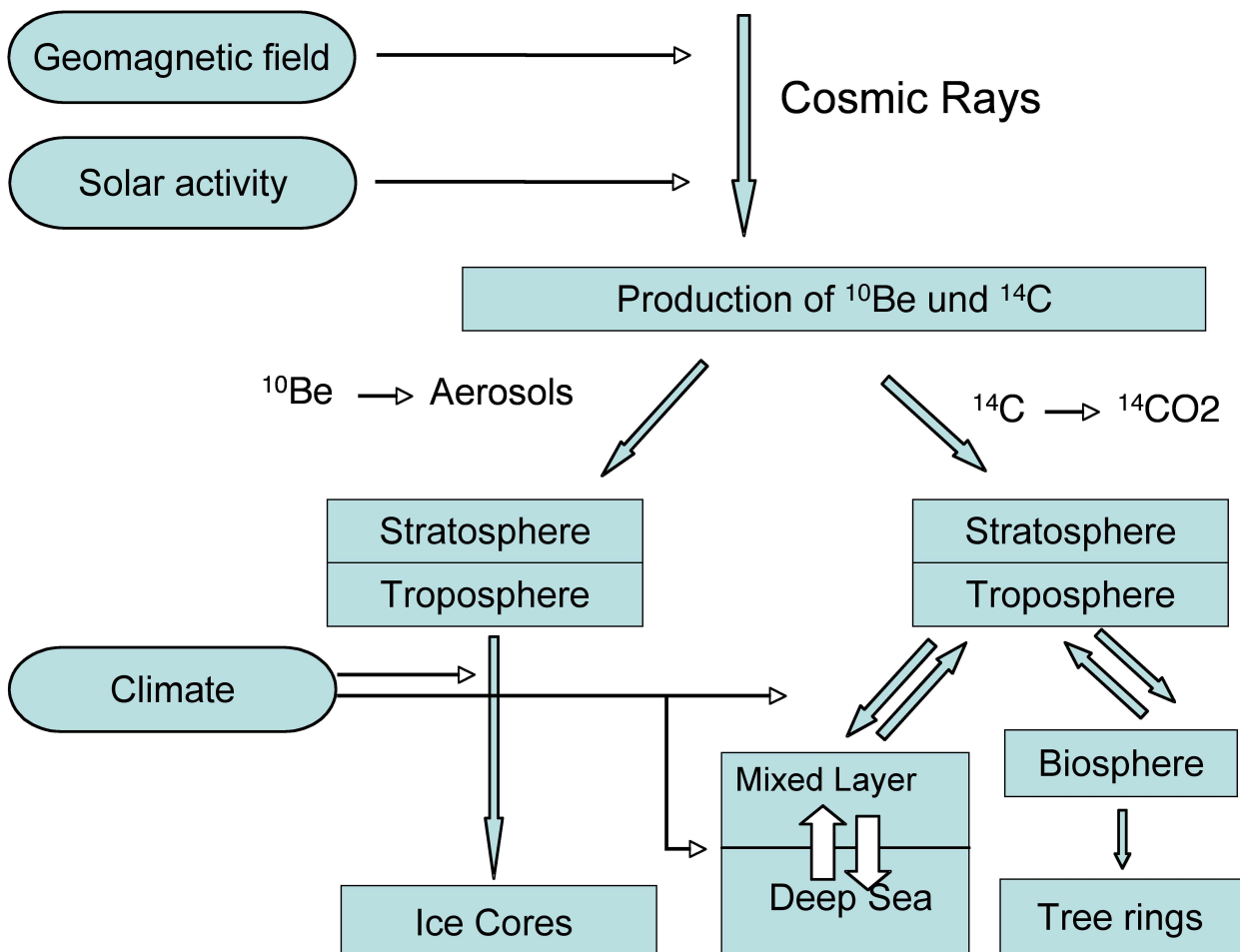


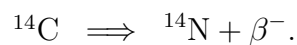
Figure 2.6: ^{10}Be and ^{14}C radionuclides in the Earth's system. This picture depicts the similarities and differences between ^{14}C and ^{10}Be systems. *Similarities*: Both radionuclides are produced in the same way, modulated by the Sun and Earth's magnetic fields. *Differences*: As a consequence of different geochemical behaviours, after production ^{10}Be becomes attached to aerosols and is removed from the atmosphere after a mean residence time of 1 to 2 years, while ^{14}C enters the carbon cycle. Therefore, climate changes influence the two radionuclides differently.

pressure of previous snow layers, the density of the aggregate of firn grains increases and, finally, snow is transformed into ice. Through this process, atmospheric constituents are stored in each layer of ice. Not only solid, but also gaseous constituents are stored in tiny air bubbles which get captured in the ice. Polar ice sheets are the only archive that potentially store information about all climate forcing factors (greenhouse gases, aerosols, dust, solar activity), as well as information about the corresponding climatic responses (temperature, wind speed and precipitation). However, one difficulty in using this natural archive is that ice flows slowly. As a consequence of the horizontal movement, annual layers become thinner with increasing depth and, therefore, the use of ice flow models is needed to account for the non linear relationship between depth and age.

Dendrochronology and Radiocarbon dating

In mid- to upper latitudes, trees are sensitive to seasonal environmental conditions. During the growing season, some environmental climatic conditions are recorded as variations in the width and the density of the annual rings. Dendrochronology is the science or technique of dating events, environmental change, and archaeological artifacts by using the characteristic patterns of annual growth rings in timber and tree trunks. Regional trees are influenced by similar climatic conditions, therefore the pattern of ring widths are also similar from tree to tree. This allows the construction of a dendrochronology by matching older tree ring patterns with newer ones for overlapping periods (see Fig. 2.7).

The important role that tree rings play in climatology can be better understood within the context of radiocarbon dating. Radiocarbon dating is the technique which assigns radiocarbon years to samples. There are three principal isotopes of carbon which occur naturally: ^{12}C , ^{13}C (both stable) and ^{14}C (unstable). The radiocarbon method is based on the study of the decay rate of the radioactive carbon isotope ^{14}C . Once a ^{14}C atom is formed, it rapidly oxidises to $^{14}\text{CO}_2$ and enters the carbon cycle. Plants and animals take up ^{14}C in the biological food chain during their lifetimes. Their ^{14}C content is in equilibrium with the ^{14}C of the atmosphere so that the $^{14}\text{C}/^{12}\text{C}$ ratio in the organism is equal to that of the atmosphere except for fractionation. As soon as a plant or an animal dies, the replenishment of radioactive carbon ceases and the only cause of changes in the ^{14}C concentration is the decay. The ^{14}C decays as follows



In order to date a material containing carbon we make use of the law of radioactive decay, *viz.*

$$S(t) = S(t_0)e^{-\lambda(t_0-t)}, \quad (2.5)$$

where:

1. $S(t)$ is the measured specific activity⁵ of the sample at time t , which is the number of decays per unit time and unit mass.
2. t_0 is the time when the ^{14}C exchange with the atmosphere is interrupted.

⁵i.e., the activity of ^{14}C per unit mass of total carbon. In this sense, the term “concentration” is used to refer to mass of ^{14}C per unit mass of total carbon.

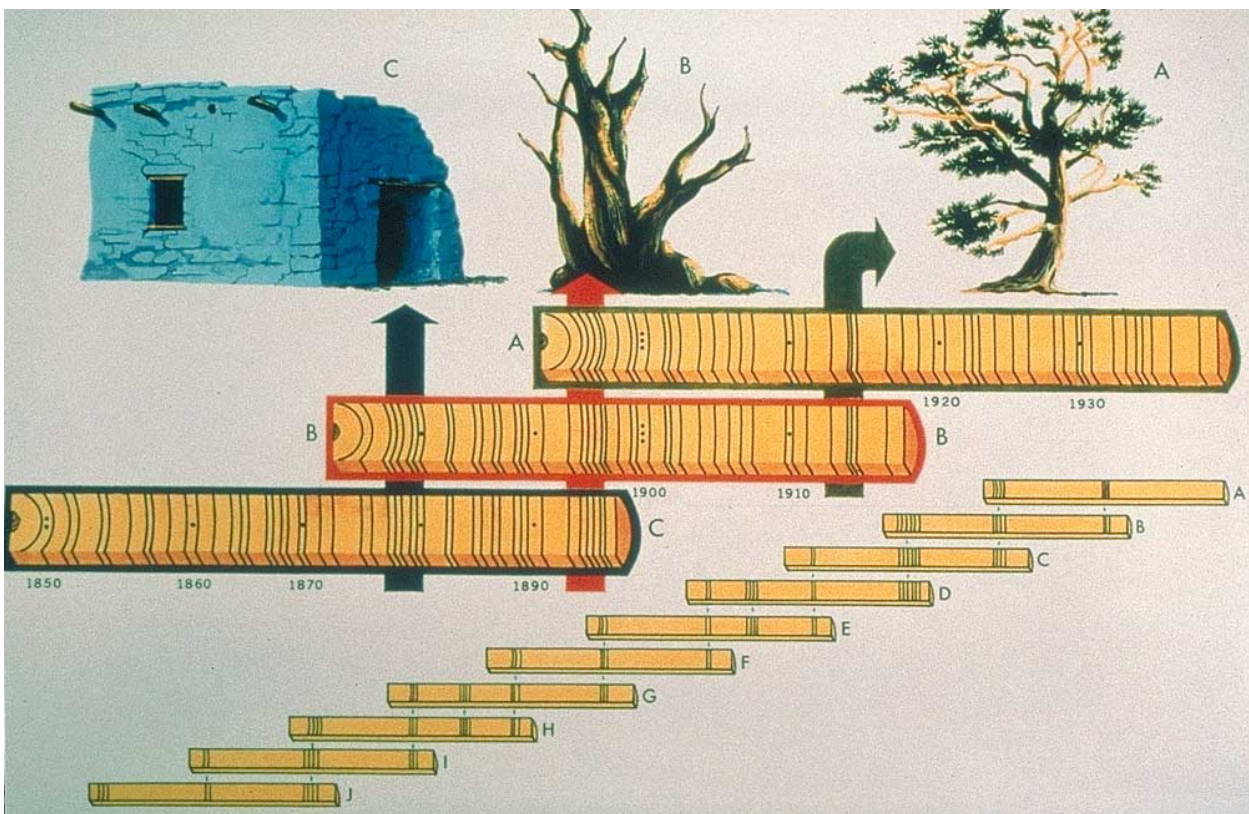


Figure 2.7: Ring widths of trees growing in the same area display common patterns. By matching these patterns from different trees, a dendrochronology can be constructed. Figure from: <http://www.ncdc.noaa.gov/paleo/treering.html>.

3. λ is the decay constant which is related to the half-life as $\ln(2)/\lambda = T_{1/2}$, where $T_{1/2}$ is the time for which $S(T_{1/2}) = S(t_0)/2$.
4. $S(t_0)$ is the specific activity of the sample at time t_0 and therefore equal to the atmospheric specific activity of ¹⁴C at that time.
5. If we denote the specific activity of ¹⁴C in the atmosphere (*i.e.*, $\frac{^{14}\text{C}}{^{12}\text{C}}(t)$) as $A(t)$ we have $A(t_0) = S(t_0)$.

Therefore, if we know $S(t)$, $S(t_0)$ and λ , we can calculate the time t_0 and therefore date the sample. Radiocarbon measurements are always reported in terms of ¹⁴C *years BP*, *radiocarbon years BP* or simply *BP*⁶ denoted as t_r . This time t_r is calculated by means of the expression

$$S(0) = A(0)e^{-\lambda_1 t_r}, \quad (2.6)$$

on the assumptions that:

1. The specific activity of atmospheric ¹⁴C has always been the same as it was in 1950 (*i.e.*, the value $A(0)$). $S(0)$ is the actual specific activity of the sample at the time 0 BP.
2. The half-life $T_{1/2}^{(1)}$ (λ_1 is the corresponding decay constant) of ¹⁴C is 5568 years.

It is important to note that t_r is a fixed number and is independent of the time of measurement (see Fig. 2.8). When the measurement takes place at a time⁷ $t < 0$, in order to calculate t_r , first $S(0)$ must be calculated. In this case the following formula is employed

$$S(0) = S(t)e^{\lambda_2 t}, \quad (2.7)$$

where in this case the true half-life $T_{1/2}^{(2)} = 5730 \pm 40$ years (λ_2 is the corresponding decay constant) is used. In other words, the ¹⁴C sample content $S(t)$ has to be corrected for decaying between 0 and time t . On the other hand, it is known that the atmospheric ¹⁴C has varied with time and that the actual half-life of ¹⁴C is 5730 y and not the 5568 y as initially measured (Godwin 1962). Hence the radiocarbon age provided by a radiocarbon laboratory is different from the true age of the sample and for this reason we need a relationship between *radiocarbon age* and *true age*. Tree rings allow to solve this problem by providing us with the temporal evolution of the atmospheric ¹⁴C concentration, $A(t)$. Figure 2.9 shows the $\Delta^{14}\text{C}$ curve (Reimer *et al.* 2004) which is defined as

$$\Delta^{14}\text{C}(t) = \left[\frac{A(t)}{A(0)} - 1 \right] \times 1000 \text{‰}. \quad (2.8)$$

Therefore, the quantity $\Delta^{14}\text{C}$ reflects the relative deviation of the atmospheric ratio $A(t)$ from a reference value $A(0)$ expressed in per mil (Stuiver & Polach 1977). Usually the age provided by tree rings is called *true age*, *dendro age* or *calendar age*. We refer to it as t_d . Hence, making use again of the exponential law,

⁶In a radiocarbon context, *BP* is a symbol meaning *conventional radiocarbon years before 1950 AD* (Stuiver & Polach 1977).

⁷I have defined the time previous to 1950 as negative.

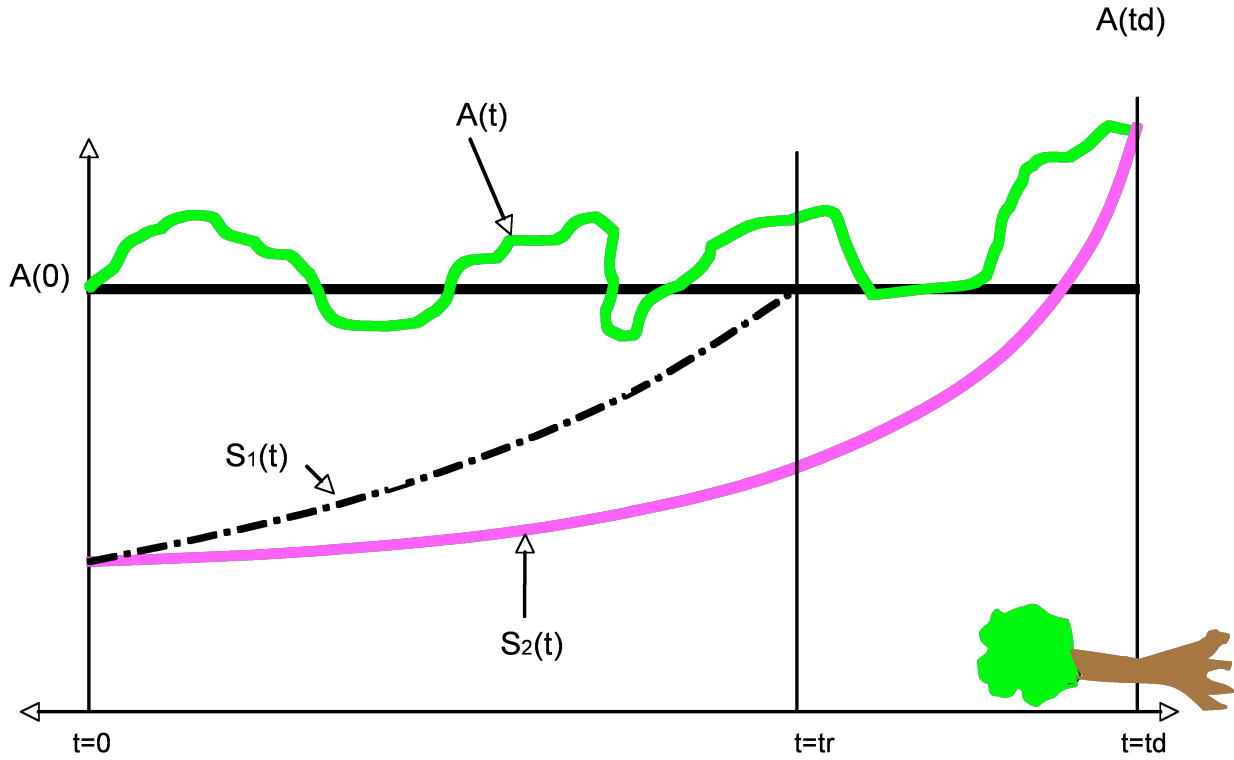


Figure 2.8: Vertical axis shows ^{14}C activities. Horizontal axis shows time in years BP (where 1950 is taken as origin of times). $A(t)$ is the specific activity of ^{14}C in the atmosphere (green line). The black horizontal line corresponds to $A(0)$. t_d is the so-called true age, that is the actual age of the sample. t_r is the radiocarbon age and represents the age that a sample would have if the atmospheric ^{14}C content had always been $A(0)$ and $T_{1/2}^{(1)}$ 5568 years. $S_1(t) = A(t_r)e^{-\lambda_1(tr-t)}$ is the law of radioactive decay assumed by the dating laboratories. $S_2(t) = A(t_d)e^{-\lambda_2(td-t)}$ represents the true decaying law with the true half-life equal to $T_{1/2}^{(2)}$ equal to 5730 years. Note that formula 2.7 is a particular case for $S_1(t)$ with $t = 0$.

$$S_2(t) = A(t_d)e^{-\lambda_2(td-t)}, t \geq 0 \quad (2.9)$$

where:

1. $A(t_d)$ is the true ^{14}C activity of the atmosphere at the moment when the ^{14}C exchange with of the atmosphere was interrupted.
2. $S_2(t)$ represents the actual temporal evolution of the sample's activity.

We are now in a position to derive the desired relationship between t_d and t_r . From Eqs. (2.6), (2.8) and (2.9), and taking into account that $S_2(0) = S(0)$ (see geometrical interpretation displayed in Fig. 2.8), it follows that

$$\Delta^{14}\text{C}(t_d) = [e^{\lambda_2 t_d - \lambda_1 t_r} - 1] \times 1000 \text{‰}. \quad (2.10)$$

If we use the value of $\Delta^{14}\text{C}$ obtained from tree rings as an input in equation 2.10 we fi-

nally obtain the relationship between radiocarbon and calendar years⁸. This is displayed in Fig. 2.10. At this point it is worth remarking that one should always keep in mind the difference between $\Delta^{14}\text{C}$ and ^{14}C production rate. $\Delta^{14}\text{C}$ shows the time evolution of atmospheric ^{14}C concentration. It can change if the production rate change or/and if there is a transfer of ^{14}C concentration between the different reservoirs of the carbon cycle. According to Peristykh & Damon (2003) the physical relationship between $\Delta^{14}\text{C}$ and ^{14}C can be represented as a convolution integral:

$$\Delta^{14}\text{C}(t) = \int_{-\infty}^t h_A[t - \tau, K(t - \tau)] \mathbb{P}[\tau, \phi(\tau), M(\tau)] \quad (2.11)$$

where $h_A(t)$ is a kernel time function of system response of the Earth's distributive system of carbon; $\mathbb{P}[\tau, \phi(\tau), M(\tau)]$ is the production rate of ^{14}C , which is a function of the level of solar activity ϕ and the intensity of geomagnetic field $M(t)$ (see chapter 6); $K(t)$ is a time function of representing the climate of the Earth which could influence the transport processes from the location of production to the natural archives. The dependence of \mathbb{P} on M is the dominant factor causing the long-term trend in $\Delta^{14}\text{C}$ Fig. (2.9).

⁸In this work the adjectives *calendar* and *calibrated* are used in the following way: A *calendar age* is an absolute date while a *calibrated age* is an estimate date based on statistical probability, and is expressed as a range of calendar years, therefore, once we get the radiocarbon age of a sample, the obtained relationship (equation 2.10) is used in order to get the corresponding *calibrated age* of the sample. In addition, the symbol *cal* is used meaning *calibrated age*. See <http://www.radiocarbon.org>.

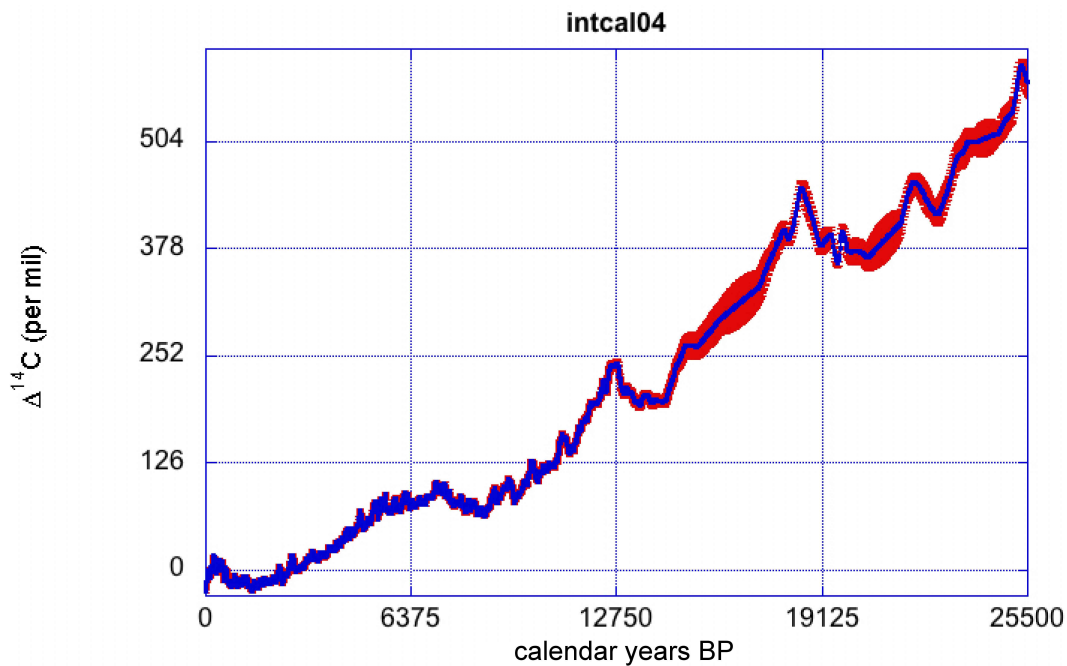


Figure 2.9: Atmospheric $\Delta^{14}\text{C}$ against calendar years (errors indicated by vertical red lines) from tree rings (Hughen *et al.* 2004).

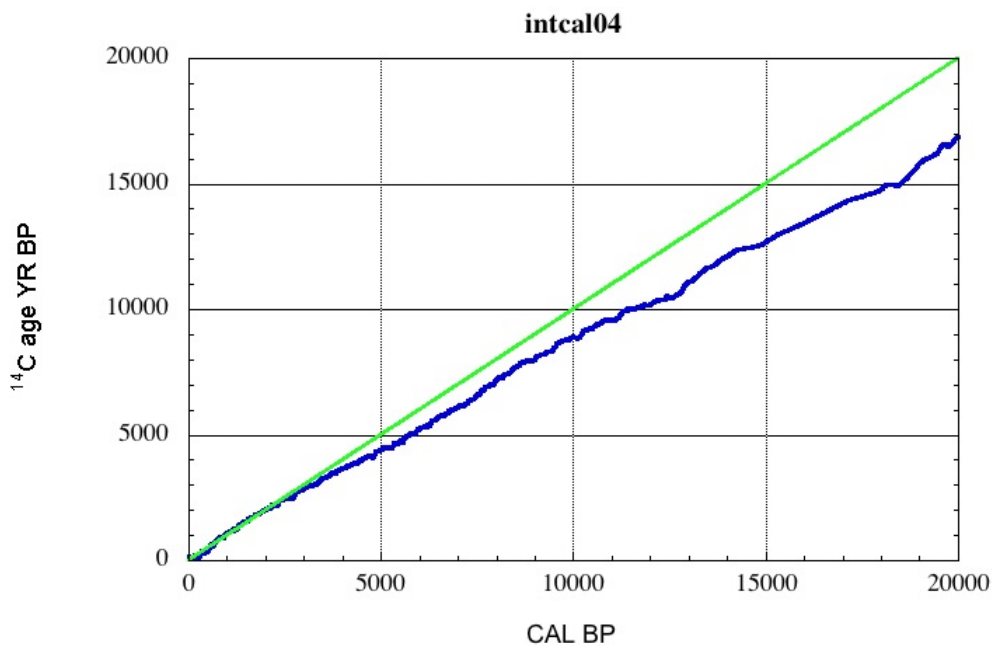


Figure 2.10: Relationship between radiocarbon age and true age (also dendro age or calendar ages). This curve consists mainly of decadal tree ring measurements (Hughen *et al.* 2004). The green line depicts the relationship between radiocarbon and calendar years if the concentration of ^{14}C had remained constant in the past and equal to the standard value of 1950.

Chapter 3

Timescale of EDML Ice Core

The cosmogenic radionuclides ^{10}Be from ice cores and ^{14}C from tree rings are the basis for this work. This chapter presents the ^{10}Be data of the EDML ice core from Antarctica. Additionally, ^{10}Be data of the GRIP ice core from Greenland and ^{14}C from tree rings are used to establish a precise time scale and to distinguish between production and system effects.

3.1 EDML Ice Core

During the period 2001-2005, a 2882 m long ice core was drilled in the Atlantic sector of Antarctica EDML (Dronning Maud Land 75°00'06" S; 00°04'04" E) within the *European Project for Ice Coring in Antarctica* (EPICA) covering more than a complete glacial cycle.

3.2 Synchronization by means of tree rings

The two main aims of this work are (i) to separate production and system effects and (ii) to find relationships between solar activity and past climate changes by comparing ^{10}Be and ^{14}C cosmogenic radionuclides. However, the ^{10}Be and ^{14}C raw data sets used in this work are not directly comparable for the following two reasons:

- The ^{14}C set used in this work was derived from measurements in tree rings; a *carbon cycle model* was used in order to calculate the corresponding production rate (Muscheler 2000). On the other hand, the ^{10}Be data set shows the ^{10}Be concentration in ice cores.
- The two data sets display different time scales.

In this chapter we solve the second problem by synchronizing both data sets. The reasons for the difference in the time scales are due to the different nature of the natural archives. The atmospheric ^{14}C data set was measured in tree rings and was dated by dendrochronology. Since dendrochronology is a very accurate technique, the time scale of the ^{14}C data set is taken as reference in order to calibrate the ^{10}Be data set. As a consequence of the ice-flow and variations in the accumulation rate, a non-linear relationship between depth and age exist for the ^{10}Be data set. While the tree rings can be relatively easily identified, in an ice core it is impossible to distinguish among annual layers and therefore to count them (layers are not visible at first sight). Thus, the assignment of dates to a depth can not be made

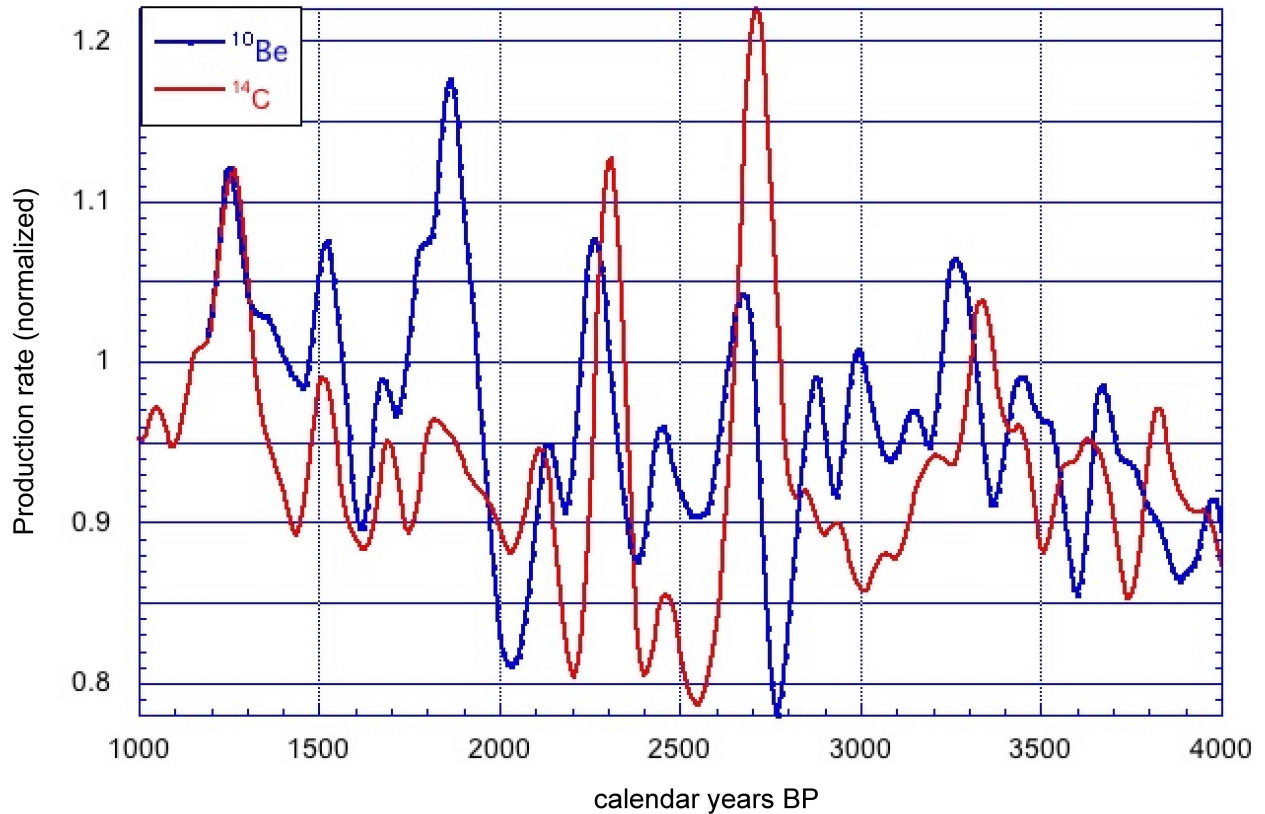


Figure 3.1: ^{10}Be (raw data) concentration and ^{14}C production rate normalized. A binomial filter of grade 31 was applied.

directly, and the dating of an ice core relies on ice flow models. However, the ice flow models are based on the accumulation rate, which is not known in detail.

An alternative approach of dating ice cores is based on the matching of the production signals of ^{10}Be and ^{14}C . The peaks in both time series correspond to solar events and, because of the similar production processes, both sets must show the same events at the same time. That means that in a graph, maxima and minima have to occur at the same time and that both graphs should have the same slope at each point. In reality, the two curves often appear slightly displaced (Fig. 3.1). Hence, the synchronization was carried out by shifting the ^{10}Be data in order to obtain an optimal match between the two records; this is the so-called *Wiggle-Match Dating* (WMD) method.

The data were normalized by dividing the data set by the mean value and the following assumptions were assumed that during the Holocene (approximately the past 11,500 years):

- the atmosphere was well mixed. That means that $\rho_{\text{Be}}(\vec{x}, t) = \rho_{\text{Be}}(t)$ (No spatial dependence) then $\text{grad}(\rho_{\text{Be}}) = \vec{0}$ and therefore $\text{div}(\vec{J}_{\text{Be}}) = \rho \cdot \text{div}(\vec{v})$ that is, flux is proportional to the concentration.
- the accumulation rate remained constant.
- owing to its very short atmospheric residence time (1-2 years), all the ^{10}Be which is produced in the atmosphere is rapidly removed from it. Since we are interested in processes which take place on time scales greater than 10 years, it can be assumed that the variation of the atmospheric ^{10}Be content is negligible.

In virtue of these assumptions changes in the production rate are equivalent to changes in concentrations. Hence, the ^{10}Be concentration was used instead of the production rate. In addition, the ^{10}Be data set was interpolated to produce a time series with the same time resolution as the ^{14}C set (10 years). Subsequently, both sets were filtered using a binomial filter of degree 31 and normalized in order to eliminate the noise and to allow for a better synchronization. Figure 3.2 shows both data sets after the records were matched as described above. As can be seen, although both curves are similar, there are some differences. On the one hand, the differences between the two graphs are due to the fact that ice flows and therefore the ^{14}C scale is more precise than the ^{10}Be scale. In addition, these differences are also a consequence of the assumptions made in the carbon cycle model used to obtain the ^{14}C production rate as well as the ^{10}Be system. Of course, this method is not perfect:

- for well structured time intervals, the error is smaller than for intervals with less clear features. For example, the peaks in Fig. 3.2 located around 2750 BP in ^{10}Be and ^{14}C data sets correspond unequivocally to the same solar event. Such peaks correspond to solar minima and cannot be due to measurement errors since the errors in the ^{10}Be set are in the order of 5 to 10%. With respect to the ^{14}C set, it can be shown by means of Monte Carlo simulations that, taking into account the errors in the measured $\Delta^{14}\text{C}$ and using the carbon cycle model, the errors in the corresponding ^{14}C production rate are smaller than the amplitudes of each of the peaks in question. However, in the interval between 2750 and 3250 there is no clear structure in either of the records; the matching in this interval is therefore ambiguous. This is illustrated with an example in Fig. 3.3 and 3.4. Figure 3.3 shows the same ^{10}Be data set synchronized by two different persons by means of the WMD method. The data set displayed in red was produced by displacing the points corresponding to the ^{10}Be set so that a good visual agreement between ^{10}Be and ^{14}C curves was achieved. The set displayed in blue was obtained in the following way: the points corresponding to the ^{10}Be set were shifted to maximize the correlation coefficient between ^{10}Be and ^{14}C curves. Figure 3.4 displays the comparison between the two time scales. It can be seen that the differences remain smaller than 50 years. However, these differences may play an important role, for example, when calculating the accumulation rate (this issue will be discussed in the next chapter.)
- It is very difficult to quantify the errors made by this method.

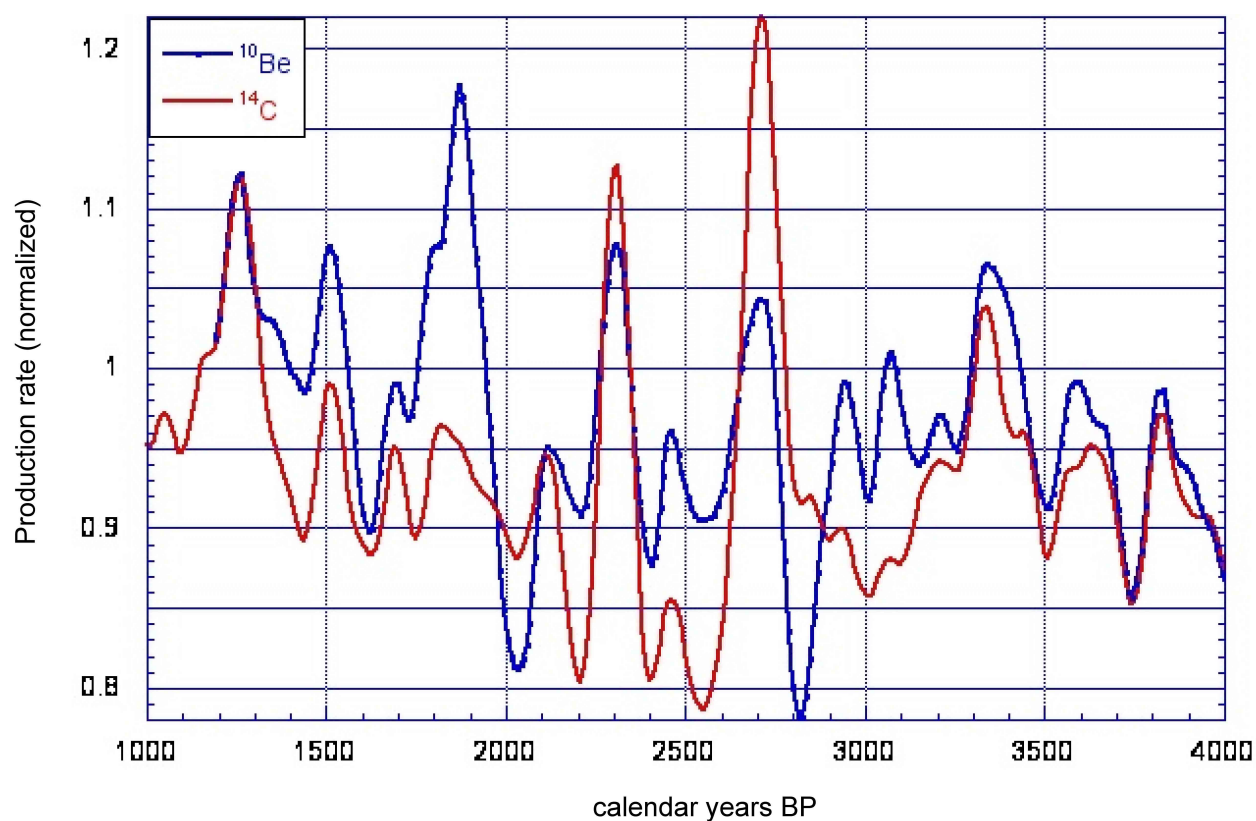


Figure 3.2: The ^{10}Be and ^{14}C data after applying the wiggle matching dating method (time scale 1).

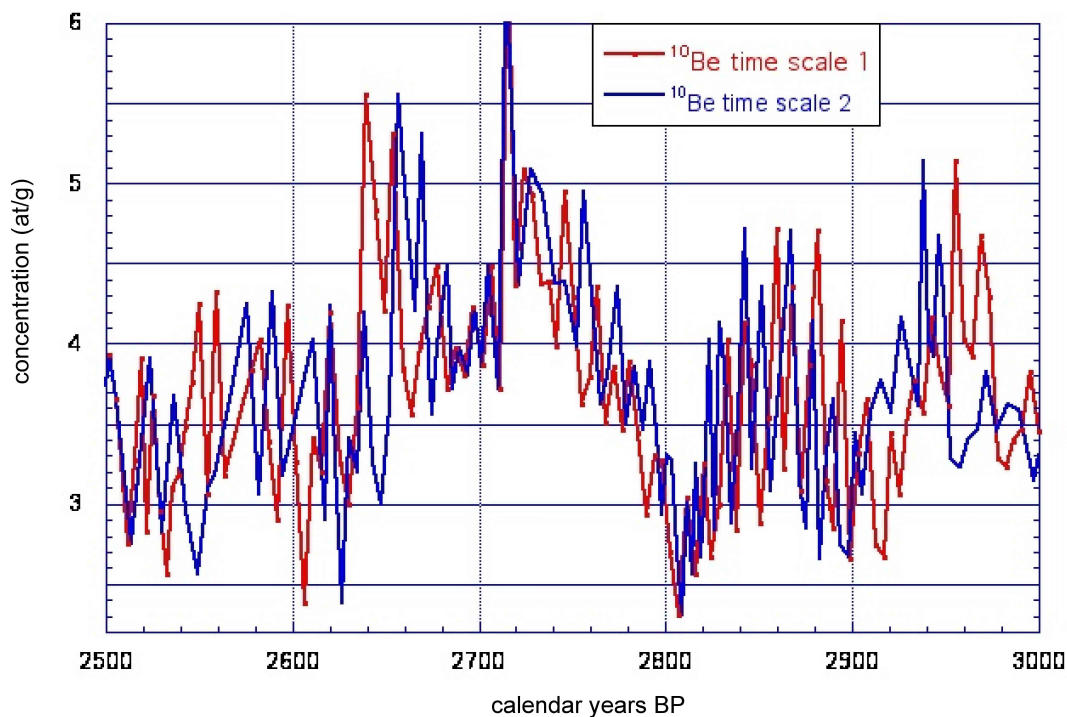


Figure 3.3: The same ^{10}Be data set synchronized by two different persons for the interval 2500-3000 BP.

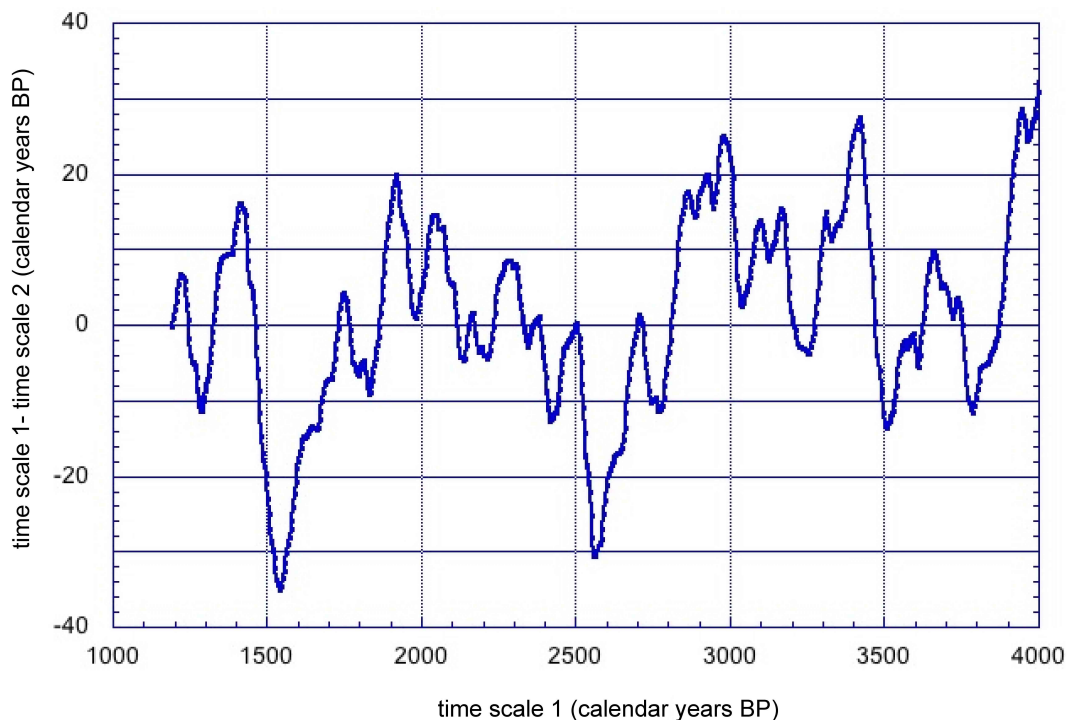


Figure 3.4: This plot represents the difference between the two times scales against time scale 1. The choice of time scale 1, rather than time scale 2 as a reference was arbitrary. For most points the differences are smaller than 40 years.

Chapter 4

The EDML Accumulation rate

In this section, an attempt to calculate the accumulation rate for the EDML ice core is presented.

4.1 Introduction

In order to compare ^{10}Be data with the ^{14}C production rate, we first need to calculate the corresponding ^{10}Be flux from the radionuclide concentrations, since as it was shown in the previous chapter, variations in ^{10}Be production rate can be assumed to be proportional to variations of the ^{10}Be flux. We shall make use of the expression

$$F_{\text{Radionuclide}} = \rho_{\text{ice}} \star Acc \star C_{\text{Radionuclide}}, \text{ where} \quad (4.1)$$

- $F_{\text{Radionuclide}}$: Flux of radionuclide ($\text{atom cm}^{-2} \text{y}$).
- ρ_{ice} : Density (g cm^{-3}).
- Acc : Accumulation rate (cm y^{-1}).
- $C_{\text{Radionuclide}}$: Concentration of radionuclide ($\text{atom g}_{\text{ice}}^{-1}$).

It is clear that the only unknown variables are the concentration of radionuclide and the accumulation rate; the density of ice is assumed to be constant. However, the determination of the past accumulation rate is not an easy task. The most simple method, from a conceptual point of view, is counting the annual layers¹. This procedure is hampered by the thinning effect, that is, the fact that annual layers become thinner with increasing depth and, therefore, flow models are needed to take this effect into account. In this work, a steady-state model is combined with ^{10}Be concentrations in EDML ice core.

4.2 Accumulation

In order to calculate the accumulation rate of the EDML ice core, the EDML time scale was first synchronized with the ^{14}C time scale as described in the previous chapter. The

¹This method is based on looking for parameters that vary with the season in a consistent manner (because the annual layers are not visible at all and therefore they cannot be counted). For example, parameters that depend on the temperature (colder in winter and warmer in summer). An example of a temperature proxy is the ratio $^{18}\text{O}/^{16}\text{O}$. The water molecules composed of H_2^{18}O evaporate less rapidly and condense more readily than water molecules composed of H_2^{16}O . As the water vapour travels towards inland, it becomes increasingly poorer in H_2^{18}O since the heavier molecules tend to precipitate first.

synchronized data set was then spline-interpolated in order to have annual resolution. Figure 4.1 represents the calculated accumulation rate. A simple visual inspection of this figure makes clear that this time series shows a trend. This trend is at least partly due to the thinning effect; another possibility could be that the actual accumulation rate has changed with time. In order to eliminate the component caused by the thinning effect the so-called Dansgaard-Johnsen (1969) model was used. This model makes the following assumptions:

1. the flow is in steady-state.
2. the flow is 2-dimensional.
3. the accumulation rate and the total ice thickness (H) are independent of time.
4. the vertical strain-rate is constant down to some distance h above the bed and from there decreases linearly to zero at the bed (the strain-rate is the strain per unit time).

Under steady-state conditions, the distance an ice particle moves downwards in a year must be equal to the thickness of an annual layer. If ω denotes the vertical velocity of an ice particle and z the vertical coordinate, the age t at distance z above the bed is thus

$$t = \int_H^z \omega^{-1} d\xi, \quad (4.2)$$

where H is the ice-equivalent thickness. With α being a positive constant and λ_H the annual accumulation rate at the surface, we obtain the following system

$$\frac{\partial \omega}{\partial z} = \alpha h \quad \text{if } h \leq z \leq H, \quad (4.3)$$

$$\frac{\partial \omega}{\partial z} = \alpha z \quad \text{if } 0 \leq z \leq h, \quad (4.4)$$

with the boundary conditions $\omega(H) = \lambda_H$ and $\omega(0) = 0$.

After solving the above system, we obtain the relationship between ω and z which allows us to integrate (4.3) and (4.4) to derive the desired time scale, that is

$$t(z) = \begin{cases} \frac{2H-h}{2\lambda_H} \ln\left(\frac{2H-h}{2z-h}\right) & \text{if } h \leq z \leq H \\ \frac{2H-h}{2\lambda_H} \left[\ln\left(\frac{2H}{h} - 1\right) + 2\left(\frac{h}{z} - 1\right) \right] & \text{if } 0 < z \leq h. \end{cases}$$

In this model H and h are taken as free parameters. In our case, however, we used $H = 2750 \pm 50$ m which is the measured thickness for EDML ice core, where h is of the order of $H/3$, and took h and λ_H as free parameters (Hammer *et al.* 1978). The regression curve of the time series was calculated and, finally, an estimate for h and the λ_H rate was obtained by comparing the model with the regression curve. Note that since the data employed correspond to the upper part of the core, a linear trend is obtained, as predicted by the model. From this comparison the accumulation value of 7,585 cm/y (ice equivalent) was obtained, while the official mean annual accumulation rate for the last 4000 years is 64.0 ± 0.5 kg m⁻² y⁻¹ (EPICA), *i. e.*, a value of 6.959 cm/y (ice equivalent). The values obtained are in relatively

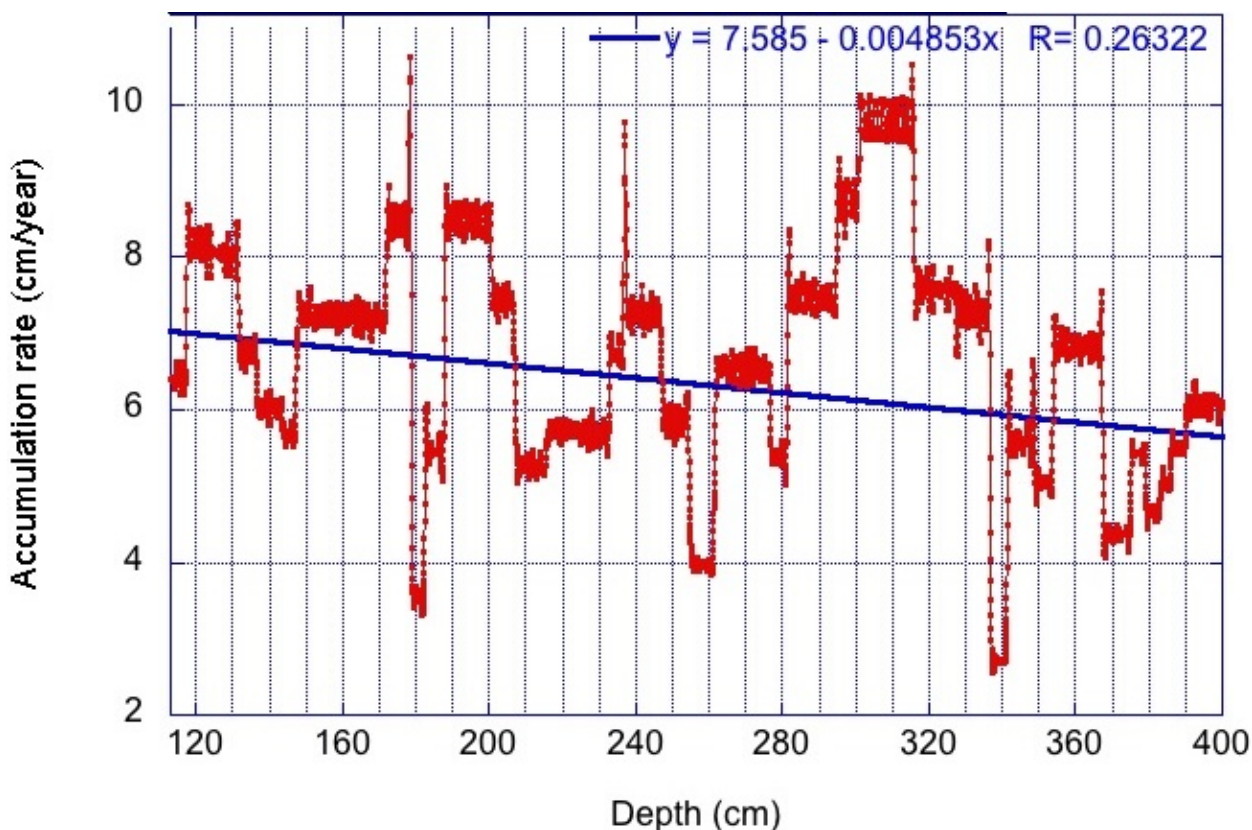


Figure 4.1: Estimation of EDML accumulation rate based on the time scale 1.

good agreement (the relative error is $\pm 8.9\%$) with the mean λ_H for EDML and, therefore, it seems reasonable to assume that the main component of the trend, at least for this interval, is the thinning effect. However, though the mean accumulation rate seems to be correct on long time scales, the same conclusion is not valid for short time scales. In order to illustrate this assertion, the same data set was synchronized by means of a computer program developed by Beer (personal communication); the results are plotted in Fig. 4.2. There, the time scale calculated by Beer is referred to as time scale 2, whereas time scale 1 refers to the time scale used in this work. Figure 3.4 displays the difference between time scale 1 and 2 against time scale 1, and shows that on long time scales both synchronizations agree quite well. From the data set corresponding to the second time scale, the accumulation rate was calculated in the same way as described previously (Fig. 4.2). From this new calculations the value of 7.614 cm/y was obtained (with a relative error of $\pm 9.4\%$).

4.3 Conclusions

The analysis described above leads to the following conclusions:

1. the calculated accumulation on time scales of years to centuries depends strongly on the dating (as was already shown in chapter 3). Thus, a better flow model is needed in order to properly take the thinning effect into account.
2. we should learn to interpret the changes in the ^{10}Be concentration in terms of climatic

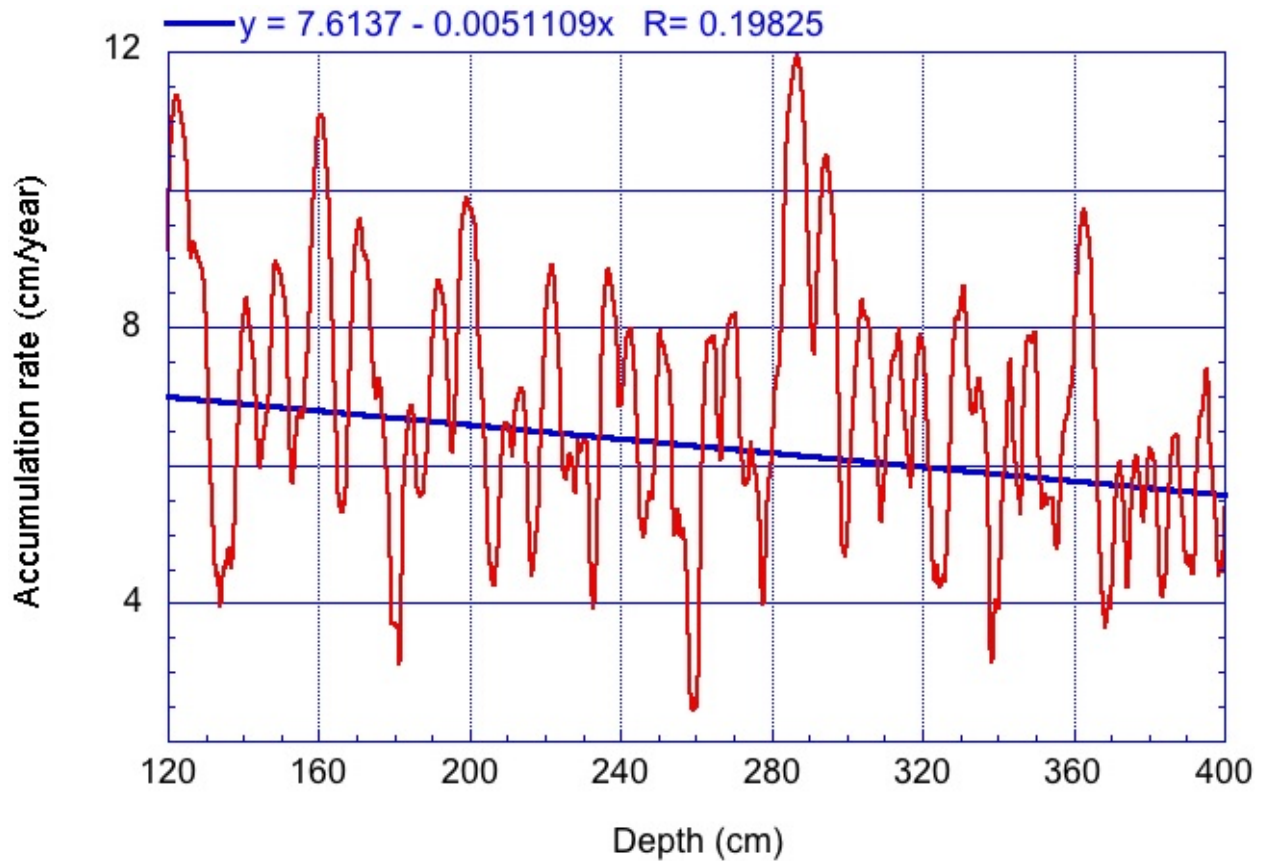


Figure 4.2: Estimation of EDML accumulation rate based on the time scale obtained by Beer.

effects; that is, to predict changes in the concentration due to changes in the ^{10}Be deposition, resulting for example, from changes in the global circulation.

3. the fact that the mean accumulation rate agrees relatively well with the estimated values for the last 6000 years BP seems to indicate that the average accumulation rate in EDML has remained relatively constant during the Holocene. Thus, as a first approximation we do not need to calculate the accumulation rate of the EDML data set in order to compare the ^{10}Be flux with the ^{14}C production rate. Therefore, the assumption that concentrations are proportional to flux should be adequate.

Chapter 5

^{10}Be in ice cores and ^{14}C in tree rings: Separation of production and climate effects

J. A. Abreu^{a,b}, J. Beer^b, F. Steinhilber^{a,b}, M. Christl^c, P. W. Kubik^c
submitted to *Geophysical Research Letters*, 2009

Abstract

Cosmogenic radionuclides are more and more used in solar activity reconstructions. However, the cosmogenic radionuclide signal also contains a climate component. It is therefore crucial to eliminate the climate information to allow a better interpretation of the reconstructed solar activity indices. In this paper the method of principal components is applied to ^{10}Be data from two ice cores from opposite hemispheres as well as to ^{14}C data from tree rings. The analysis shows that these records are dominated by a common signal which explains about 80% of the variance on multi decadal to multi millennial time scales, reflecting their common production rate. The second and third components are significantly different for ^{14}C and ^{10}Be . They are interpreted as system effects introduced by the transport of ^{10}Be and ^{14}C from the atmosphere where they are produced to the respective natural archives where they are stored. Principal component analysis improves significantly the production signal which is more appropriate for astrophysical and terrestrial studies.

5.1 Introduction

Cosmogenic radionuclides stored in natural archives such as ^{10}Be in ice cores and ^{14}C in tree rings have proven to be very useful in reconstructing past solar activity (Vonmoos *et al.* 2006) and changes in the geomagnetic field intensity over many millennia (Muscheler *et al.* 2005). At present, cosmogenic radionuclides are the only proxy to significantly extend the record of solar activity which is restricted to the past 400 years of sunspot observations. They offer the unique opportunity not only to study the long-term history of solar activity (Solanki

^aETH Zürich, 8092 Zürich, Switzerland

^bSwiss Federal Institute of Aquatic Science and Technology, Eawag, 8600 Dübendorf, Switzerland

^cIon Beam Physics, ETH Zürich, Zürich, Switzerland

et al. 2004; Vonmoos *et al.* 2006; Steinhilber *et al.* 2008) and solar forcing (Steinhilber *et al.* 2009), but also to make predictions about future trends in solar variability (Abreu *et al.* 2008). However, the cosmogenic radionuclide signal contains also a climate component introduced by the transport of the radionuclides from the atmosphere where they are produced to the archive where they are stored. In order to make full use of the large potential of cosmogenic radionuclides the climate signal must be removed. Fortunately, while both nuclides are produced in a similar way, the response of the ^{10}Be and the ^{14}C systems to climate variations is very different by virtue of their different geochemical properties. ^{14}C enters the global carbon cycle, whereas ^{10}Be is removed within 1-2 years from the atmosphere by precipitation. Thus, comparing both radionuclides makes it possible to distinguish between climate induced and production (solar/geomagnetic) variations. In this article, we propose to apply principal component analysis (PCA) to ^{10}Be from ice cores and ^{14}C from tree rings in order to decompose them into a production and a climate signal.

5.2 ^{10}Be and ^{14}C systems

5.2.1 The production of cosmogenic radionuclides

Cosmic rays are composed roughly of 90 % protons, 9 % helium nuclei, and 1 % of heavier nuclei. When these highly energetic primary particles of galactic cosmic rays interact with atmospheric N and O, a chain of secondary particles is generated which is responsible for the production of cosmogenic radionuclides. There are two main processes which modulate the production rate of cosmogenic radionuclides in the atmosphere: changes in solar activity and changes in the geomagnetic field intensity. Since ^{10}Be and ^{14}C are produced by similar nuclear reactions their production signals are also very similar. However, this production signal is modified by climate induced effects on the transport from the atmosphere into the respective archives as discussed in the next section.

5.2.2 ^{10}Be and ^{14}C in the climate system

Figure 2.6 illustrates the similarities and differences between ^{10}Be and ^{14}C radionuclides in the Earth's system. After production, ^{14}C oxidizes to CO_2 and enters in the carbon cycle. Within the carbon cycle, ^{14}C gets involved in exchange processes among the atmosphere, the biosphere and the ocean. Its atmospheric residence time of about 8 years regarding exchange with the ocean is long enough that it can be considered as globally well mixed (Siegenthaler *et al.* 1980). In contrast, ^{10}Be has an atmospheric residence time of 1 to 2 years. The fact that ^{14}C enters the carbon cycle constitutes a fundamental difference between the measured signal in tree rings and the ^{10}Be signal measured in ice cores. The carbon cycle acts like a filter (Peristykh *et al.* 2003) changing the original amplitude and phase of the ^{14}C production signal. As a consequence, direct comparison between $\Delta^{14}\text{C}$ measured in tree rings with ^{10}Be measured in ice cores is not possible. We must first remove the effect of the carbon cycle on ^{14}C . Figure 5.2a shows $\Delta^{14}\text{C}$ as measured in tree rings (Reimer *et al.* 2004). Figure 5.2b shows the corresponding ^{14}C production rate calculated after applying the carbon cycle model by (Oeschger *et al.* 1975). Figure 5.2c shows the ^{10}Be concentrations as measured in ice cores whereas Fig. 5.2d shows the corresponding ^{10}Be flux. Comparison of the four panels shows clearly that ^{10}Be reflects changes in production rate much more directly than

^{14}C . Furthermore, modelling shows that even a climate change from the present warm period with high solar activity to the Maunder minimum period with very low solar activity has only a small effect on the atmospheric transport and deposition processes of ^{10}Be , confirming that production is the dominant factor (Heikkilä *et al.* 2008). Our two main working hypotheses are: (I) the ^{10}Be and ^{14}C records can be interpreted as being composed of a production signal, which is common to both radionuclides, and (II) a system signal, which is, most likely, not a common signal. Due to the different geochemical properties the combination of these two cosmogenic radionuclides in a PCA study provides a powerful tool to disentangle production and system effects.

5.2.3 The data

In the present work we use ^{10}Be measured in EDML¹ (Antarctica) and GRIP² (Greenland) ice cores and ^{14}C production derived from tree rings³. The records employed in the analysis cover a common period of 8180 years from 1210 BP to 9390 BP (740 AD to -7440 AD). The averaged temporal resolution of the EDML time series is 4-5 years. The GRIP data have an average temporal resolution of 2-7 years. The ^{10}Be records were linearly interpolated to 1y, resampled to 10y, and 40y low-pass filtered. The ^{10}Be fluxes were calculated from ^{10}Be concentrations and the corresponding accumulation rates. The ^{14}C record has a constant time resolution of 10 years and was 40y low-pass filtered.

Based on the previous discussion, we assume that the three data sets are composed of a *production signal* $P(t)$, as well as a *system effect signal* $S(t)$. $P(t)$ takes into account the modulation effect of the sun and the geomagnetic field whereas $S(t)$ represents the effect that the climate exerts on the radionuclides including noise

$$\begin{aligned} {}^{10}\text{Be}_{\text{grip}}(t) &= P(t) + S_1(t), \\ {}^{10}\text{Be}_{\text{edml}}(t) &= P(t) + S_2(t), \\ {}^{14}\text{C}(t) &= P(t) + S_3(t), \end{aligned}$$

where the subscripts indicate that the radionuclides are influenced differently by the climate. Additionally, the $S_i(t)$ terms may be written as

$$S_i(t) = S_i[K(t)],$$

where $K(t)$ stands for *climate*, an idealized variable which takes into account the temporal evolution of the climate. If the *climate* remains unchanged, then ^{14}C changes must be equal to ^{10}Be changes. As can be seen in Fig. 5.2 (only the interval 4400 to 5800 BP is shown) the three curves are over all very similar, but there are some differences, which must be due to changes in the climate system. To separate the data into two components, we assume that $P(t)$ and $S_i(t)$ are uncorrelated. This assumption is supported by the following arguments: (1) the production does not depend on the climate and (2) although the climate components may correlate through solar modulation slightly with the production, climate change affects the ^{14}C and ^{10}Be systems very differently due to their different geochemical behaviors.

¹Ice core drilled in the framework of the European Project for Ice Coring in Antarctica (EPICA)

²Greenland Ice Core Project

³INTCAL04 (Reimer *et al.* 2004)

5.3 Separation of production and system effects using PCA

PCA finds a new set of variables (time series) $C_j, j = \{1, 2, 3\}$ which are uncorrelated. These new variables are known as the *principal components*. This allows us to decompose X_i , the original time series, into the desired form as

$$X_i(t) = \sum_j \alpha_{i,j} C_j(t) \quad (5.1)$$

where

1. $\alpha_{i,j} = \sigma(X_i)R(C_j, X_i)/\lambda_j^{0.5}$ with $R(C_j, X_i)$ the correlation coefficient between component j and nuclide i . σ is the standard deviation.
2. λ_j are the eigenvalues of the covariance corresponding to the data matrix. They give the fraction of the total variance explained by the component j .

5.4 Results

Table 5.1 shows the calculated coefficients $\alpha_{i,j}$, i.e. the contribution of component j to nuclide i as expressed by Eq. (5.1). Additionally, the squared correlation coefficients along with the eigenvalues are shown. The eigenvalue corresponding to the first component explains 65 % of the total variance whereas the second and third components are responsible for 22% and 14% of the total variance, respectively. Clearly, all the original data sets are well correlated with the first principal component supporting our hypothesis (I) that production dominates both radionuclides. Production changes are indeed responsible for most of the variance in the data. We attribute it to solar activity as well as to geomagnetic field variations⁴. It is remarkable that the α_2 coefficient corresponding to ^{14}C is significantly smaller than the corresponding α_2 of the two ^{10}Be records. We note that

1. The variance not explained by the first principal component for ^{14}C is explained only by the third component.
2. The variance not explained by the first principal component for both ^{10}Be records is mainly explained by the second component.

This confirms our initial hypothesis (II) that climate affects the ^{14}C and ^{10}Be systems differently. Hence, we attribute the second and third components to the climate effect on the ^{14}C and ^{10}Be systems, respectively.

The outcome of the PCA analysis depends critically on the accuracy of the time scales of the involved cosmogenic radionuclide records. While the time scale of ^{14}C is based on dendrochronology and therefore accurate to one year, the uncertainty of the time scales of the ice cores increases with age to a few decades. This is due to the fact that a perfect annual marker as in the case of trees is missing. In addition ice is flowing which leads to a decrease in the annual layer thickness with increasing depth. As a result of small time

⁴The effect of the Earth's magnetic field, can be removed by taking into account paleorecords of the geomagnetic field and production calculations (Masarik & Beer 2009)

Table 5.1: $\alpha_{i,j}$, $R(C_j, X_i)^2$ and λ_i before synchronization

	α_1	α_2	α_3
$^{10}\text{Be}_{\text{grip}}$	0.54	0.79	0.29
$^{10}\text{Be}_{\text{edml}}$	0.57	-0.60	0.56
^{14}C	0.62	-0.13	-0.77
	R^2	R^2	R^2
$^{10}\text{Be}_{\text{grip}}$	0.55	0.41	0.04
$^{10}\text{Be}_{\text{edml}}$	0.64	0.23	0.13
^{14}C	0.74	0.01	0.24
	λ_1	λ_2	λ_3
	65%	22%	14%

Table 5.2: $\alpha_{i,j}$, $R(C_j, X_i)^2$ and λ_i after synchronization.

	α_1	α_2	α_3
$^{10}\text{Be}_{\text{grip}}$	0.58	0.72	0.38
$^{10}\text{Be}_{\text{edml}}$	0.58	-0.70	0.42
^{14}C	0.57	-0.02	-0.82
	R^2	R^2	R^2
$^{10}\text{Be}_{\text{grip}}$	0.77	0.18	0.06
$^{10}\text{Be}_{\text{edml}}$	0.77	0.16	0.07
^{14}C	0.72	0.00	0.27
	λ_1	λ_2	λ_3
	76%	11%	13%

shifts, PCA interprets part of the common production changes as a different signal and assigns it to the second component. To test this effect, we slightly adjusted the two ^{10}Be time scales within the stated uncertainties to the ^{14}C time scale using wiggle matching (Ruth *et al.* 2007). The adjustments relative to the original time scales are smaller than 30 y for EDML and smaller than 50 y for GRIP. Now the first principal component explains 76% and the second component 11% of the total variance respectively (Table 5.2). However, the structure of the data remains relatively unchanged. The α_2 coefficient for ^{14}C is one order of magnitude smaller than the corresponding values for ^{10}Be . The third component is still the main non-production source of variability in ^{14}C , whereas the second component is the main non-production source of variability for both ^{10}Be data sets. We notice that in both calculations the sign of α_2 for GRIP and EDML are different. This is a mathematical consequence of the PCA method because of the limited number of ^{10}Be proxies used.

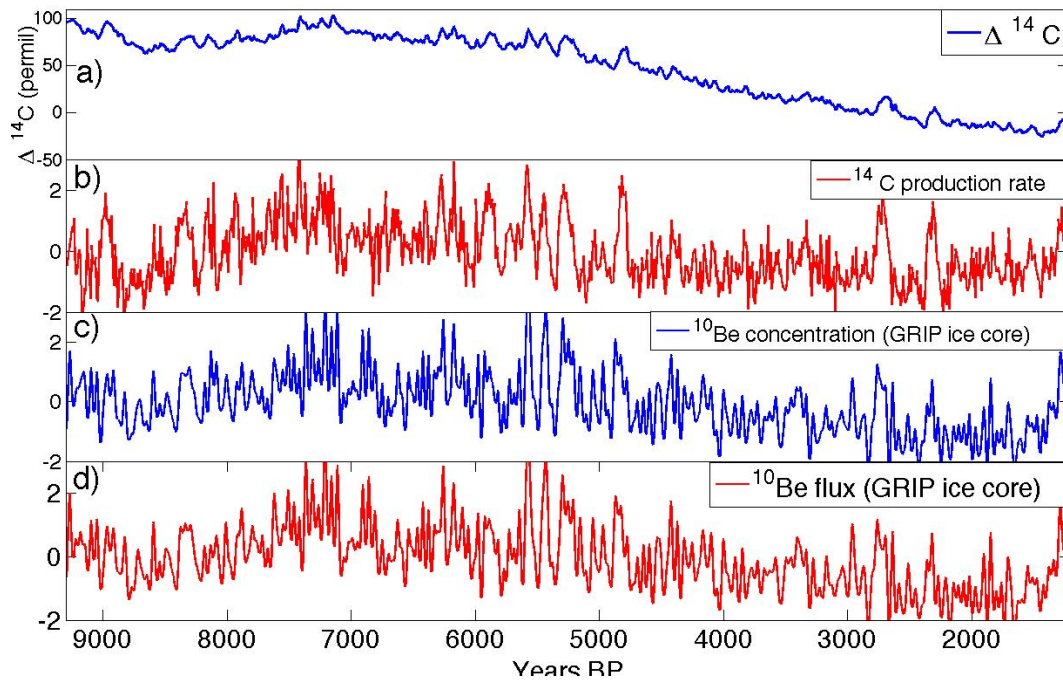


Figure 5.1: a: $\Delta^{14}\text{C}$ (Per mil) as measured in tree rings. b: Standardized (*i.e.*, subtracting the mean, then dividing by the standard deviation) of ^{14}C production rate calculated from $\Delta^{14}\text{C}$ (Per mil) by using a carbon cycle model. c: Standardized ^{10}Be concentrations (GRIP ice core) after being linearly interpolated to 1 year and low-pass filtered with a cutoff 40 years. d: Standardized ^{10}Be fluxes (GRIP ice core) after being linearly interpolated to 1 year and low-pass filtered with cutoff 40 years.

5.5 Conclusions

The method of PCA confirms that ^{10}Be and ^{14}C records which were all low-pass filtered with 40 years are dominated by a common signal which reflects the production rate and explains 76% of the variance on multi decadal to multi millennial time scales. The second and third components account for about 24% of the variance, which is significantly different for ^{14}C and ^{10}Be . This can be explained as system effects introduced by the transport of the respective radionuclides from the atmosphere where they are produced to the archive where they are stored (tree rings in the case of ^{14}C and ice cores in the case of ^{10}Be). The presence of such a high common variability is remarkable if we take into account that the ^{10}Be records are from different hemispheres, and that ^{10}Be and ^{14}C are characterized by completely different geochemical systems (compare panels a and c in Fig. 5.2). We have focused on the decomposition of cosmogenic radionuclides into production and system effects. Since cosmogenic radionuclides are the only tool to reconstruct past solar activity indices such as sunspots and total solar irradiance, it is crucial to eliminate the climate component. PCA is an adequate tool to achieve this aim.

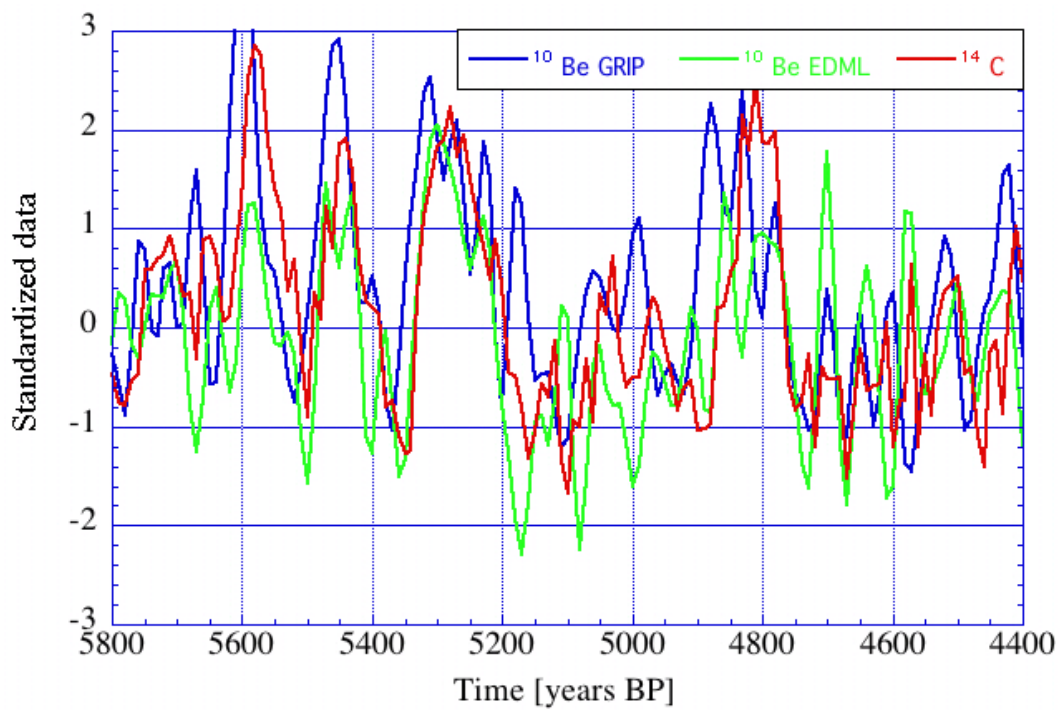


Figure 5.2: Standardized time series of ^{10}Be and ^{14}C data after being linearly interpolated to 1 year, resampled with 10 years, and low-pass filtered with a cutoff 40 years. Here we only depict the interval 4400 to 5800 BP to show the structure of the data.

Chapter 6

From ^{10}Be in ice to solar activity

The modulation of the galactic cosmic rays by the solar wind, can be described by a single parameter known in the literature as *force field parameter* or *solar modulation potential* ϕ . The concept of solar modulation potential arises from a simplified version of the transport equation (Gleeson & Axford 1968). Several authors have calculated the atmospheric production rate of cosmogenic radionuclides for different levels of solar activity (different values of ϕ) and geomagnetic field intensities, thus providing the relationship between ^{10}Be , ϕ and the geomagnetic field (Masarik & Beer 1999, 2009). In this chapter a short introduction is given to this subjects, in order to provide the reader with some basic concepts and facilitate the comprehension of future sections.

6.1 The force field parameter ϕ and the modulation function Φ

The evolution of cosmic rays within the heliosphere is described by the so-called transport equation, initially given by Parker (1965). If $f(t, \mathbf{r}, p)$ is the *omnidirectional part of the cosmic ray distribution function* with respect to particle momentum p , at time t and at position \mathbf{r} , its evolution is given by a continuity equation of the form (Caballero Lopez & Moraal 2004):

$$\frac{\partial f}{\partial t} = -(\mathbf{V} \cdot \nabla)f - \text{div}(\hat{\kappa} \mathbf{grad} f) + \frac{1}{3} \text{div} \mathbf{V} \frac{\partial f}{\partial \ln p} + Q, \quad (6.1)$$

where

$\hat{\kappa}$: is the diffusion tensor

\mathbf{V} : is the solar wind velocity

Q : is the local production of cosmic rays

Equation (6.1) tell us that the local time variation of cosmic rays is due to 1) advection 2) diffusion caused by irregularities in the background magnetic field 3) adiabatic energy changes depending on the sign of the divergence of the solar wind, and 4) due to local production of cosmic rays. Because the full solution of the transport equation is very complex, various levels of approximations are used instead. Gleeson & Axford (1968) developed the so called *force field approximation* showing that the level of modulation of galactic cosmic rays can be described by just one parameter. This approximation assumes that

1. There is no local production of galactic cosmic rays within the heliosphere: $Q = 0$
2. Steady state: $\frac{\partial f}{\partial t} = 0$
3. Adiabatic energy loss rate are negligible: $\frac{1}{3} \operatorname{div} \mathbf{V} \frac{\partial f}{\partial \ln p} = 0$.

If additionally spherical symmetry is assumed, *i.e.* $\hat{\kappa} = \kappa \hat{I}$, with \hat{I} the identity tensor, eq. (6.1) becomes

$$\frac{\partial f}{\partial r} + \frac{VP}{3\kappa} \frac{\partial f}{\partial P} = 0, \quad (6.2)$$

where the variable momentum p has been transformed to the variable *rigidity*, P , with $P = \frac{pc}{q} = \frac{A}{Ze} \sqrt{E^2 - E_0^2}$, where $E = T + E_0$ is kinetic energy plus rest energy per nucleon and A , Z and e are mass number, charge number and elementary charge, respectively. The solution of eq. (6.2) is

$$f(r, P) = \text{constant} = f(r_b, P_b), \quad (6.3)$$

along the contours of the characteristic equation $dP/dt = VP/3\kappa$ in (r, P) space. The subscript b refers to values on the outer boundary of the heliosphere. The name *force field* is due to the term $\frac{VP}{3\kappa}$, because it has the dimensions of an electric field. Equation 6.3 written in terms of cosmic ray intensities reads

$$J_Z(r, E) = J_Z(r_b, E_{r_b}) \frac{(E^2 - E_0^2)}{(E_b^2 - E_0^2)}, \quad (6.4)$$

where E was taken as independent variable instead P ¹.

With the additional hypothesis that the diffusion coefficient is separable in the form $\kappa = \beta\kappa_1(r)\kappa_2(P)$, integration of the characteristic equation reads

$$\int_P^{P_b} \frac{\beta(P')\kappa_2(P')}{P'} dP' = \int_r^{r_b} \frac{V(r')}{3\kappa_1(r')} dr' \equiv \phi(r), \quad (6.5)$$

where ϕ is called the *force field parameter*. In addition to ϕ , Gleeson & Axford (1968), introduced the concept of *modulation function*, which is written with the greek capital letter Φ . I first introduce the auxiliary function ζ as follows

$$\zeta(E, Z) \equiv \int_{E_0}^E \frac{\beta(E', Z)\kappa_2(E')}{E'} dE', \quad (6.6)$$

so that $\zeta^{-1} \equiv \psi$, and such as $E = \psi(\zeta, Z)$. Then Φ is given by

$$\Phi(r, E, Z) = \psi[\zeta(E, Z) + \phi(r)] - \psi[\zeta(E, Z)], \quad (6.7)$$

From eq. (6.5), we see that $\zeta(E_b, Z) = \zeta(E, Z) + \phi(r)$ and therefore

$$\Phi(r, E_b, Z) = E_b - E, \quad (6.8)$$

¹I have introduced the following notation $J_Z(r, E) \equiv J[r, P(Z, E)]$

6.2 ^{10}Be Production rate as a function of geomagnetic field and solar activity 51

we also see that Φ has dimensions of energy per nucleon and, physically, it can be identified with the mean energy loss experienced in coming from r_b to r . We also see that Φ is completely determined by E , Z , E_0 and ϕ . Therefore, Φ is a function of both energy and species, whereas ϕ and κ_2 are independent of the species of cosmic ray particles. The functional form of Φ requires the determination of κ_2 and ϕ . Unfortunately, this involves an integral over the region beyond the Earth's orbit, which is not easy to evaluate. Therefore eq. (6.7) is the more general form which can be given, relating Φ and ϕ . Fortunately, in the case of interest regarding ^{10}Be production, a simple relation between Φ and ϕ can be given. When $\kappa_2 = P$ then eq. (6.6) can be integrated

$$\Phi(r, E) = \frac{Z e}{A} \phi(r), \quad (6.9)$$

and this holds for relativistic as well as non-relativistic particles because no restriction on β has been made yet. In this conditions eq. (6.4) reads

$$J_Z(r, E) = J_Z(r_b, E + \frac{Z e}{A} \phi) \frac{E^2 - E_0^2}{[\frac{Z e}{A} \phi + E]^2 - E_0^2}, \quad (6.10)$$

Gleeson & Axford (1968) noted the *formal correspondence* between eq. (6.10) and that obtained for positively charged particles, assuming an heliocentric field $\mathbb{E}(r) = \frac{1}{3}V(r)/\kappa_1(r)$ with ϕ the electric potential. For this reason ϕ is also called the *modulation potential*. Note that the spectrum of cosmic rays at r_b is not know since no spacecraft has reached the end of the heliosphere yet. Therefore, available $J(r_b, E_{r_b})$ are based on theoretical considerations and observations within the heliosphere (Steinhilber *et al.* 2008). If $\beta = 1$ then, integration of eq. (6.5) reduces to $\phi = P_b - P$ and ϕ becomes a rigidity loss. It is worth noting that the force field approximation, has been shown to provide a good empirical fit to the observed modulation of cosmic ray spectrum for $E \geq 500$ MeV/nucleon at 1 AU (McCracken *et al.* 2004). Since the production rate of ^{10}Be peaks around 1-2 GeV/nucleon, the force field approximation provides a simple and straightforward description of the solar modulation of ^{10}Be .

6.2 ^{10}Be Production rate as a function of geomagnetic field and solar activity

The modulation function enables us to quantify the level of solar activity. However, galactic cosmic rays are not only modulated by the solar wind, but also by the geomagnetic field. The Earth's magnetic field (M) deviates incoming cosmic rays particles depending on their magnetic rigidity and angle of incidence, so that only particles with energy above a cutoff energy $E_k^0(M)$ can penetrate in the Earth's atmosphere. The functional dependence of cosmogenic production on the geomagnetic field and solar activity has been calculated by several authors (see Masarik & Beer 1999, 2009 and references therein). In this work I will refer only to the calculations performed by Masarik and Beer. In that calculations, the Earth's atmosphere was modeled as a spherical shell with an inner radius of 6378 *km* and a thickness of 100 *km*. This shell was divided into 34 concentric subshells of equal thickness. Each shell was divided into 9 latitudinal sections in steps of 10 degrees in magnetic latitude. The intensity of the geomagnetic field was assumed to depend on latitude only. The production rate \mathbb{P}_j of

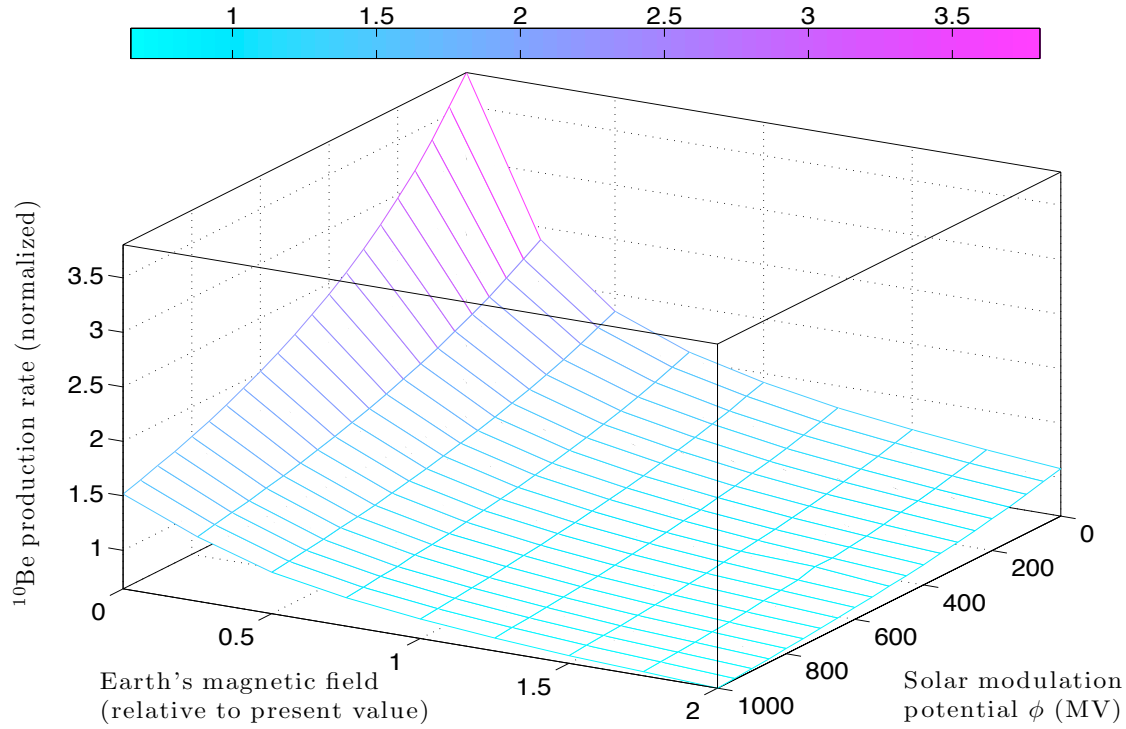


Figure 6.1: Global ^{10}Be production rate against Earth's magnetic field (relative to present value) and solar modulation ϕ . We normalized the production rate by assuming the production rate = 1, for the magnetic field = 1 and the solar activity $\phi = 550$ MV.

nuclide j at latitude λ , depth z , solar modulation ϕ and geomagnetic field intensity M was calculated as

$$\mathbb{P}_j(\lambda, z, \phi, M) = \sum_{i,k} N_i \int_0^\infty \sigma_{ijk}(E_k) J_k(E_k, \lambda, z, \phi, M) dE_k, \quad (6.11)$$

where, N_i is the number of atoms for target element i per mass in the sample, and σ_{ijk} is the cross section for the production of nuclide j from the target element i by particle type k with energy E_k . $J_k(E_k, \lambda, z, \phi, M)$ is the differential flux of particles of type k with energy E_k at latitude λ , at depth z and geomagnetic field intensity M . Note that $J_k(E_k, \lambda, z, \phi, M)$ is the differential flux within the Earth's atmosphere, *i.e.*, valid for $z \leq z_0$, z_0 being the maximal height of the atmosphere used in the calculations. The effect of the geomagnetic field was taken into account by imposing boundary conditions to the particle flux at the top of the atmosphere

$$J_k(E_k, \lambda, z_0, \phi, M) = \begin{cases} J_k(z_0, E_k), & \text{if } E_k \geq E_k^0[M(\lambda)] \\ 0, & \text{if } E_k < E_k^0[M(\lambda)] \end{cases} \quad (6.12)$$

where $J_k(z_0, E_k)$ is the particle flux of primary radiation at 1 AU given by eq. (6.10). Figure 6.1 depicts $\mathbb{P}_j(\lambda, z, \phi, M)$ after averaging in λ and z .

Chapter 7

For how long will the current grand maximum of solar activity persist?

J. A. Abreu^{a,b}, J. Beer^b, F. Steinhilber^{a,b}, S. M. Tobias^c, N. O. Weiss^d
Geophysical Research Letters, 2008

Abstract

Understanding the Sun's magnetic activity is important because of its impact on the Earth's environment. The sunspot record since 1610 shows irregular 11-year cycles of activity; they are modulated on longer timescales and were interrupted by the Maunder minimum in the 17th century. Future behavior cannot easily be predicted – even in the short-term. Recent activity has been abnormally high for at least 8 cycles: is this grand maximum likely to terminate soon or even to be followed by another (Maunder-like) grand minimum? To answer these questions we use, as a measure of the Sun's open magnetic field, a composite record of the solar modulation potential ϕ , reconstructed principally from the proxy record of cosmogenic ^{10}Be abundances in the GRIP ice core from Greenland. This ϕ record extends back for almost 10,000 years, showing many grand maxima and grand minima (defined as intervals when ϕ is within the top or bottom 20% of a Gaussian distribution). We carry out a statistical analysis of this record and calculate the life expectancy of the current grand maximum. We find that it is only expected to last for a further 15–36 years, with the more reliable methods yielding shorter expectancies, and we therefore predict a decline in solar activity within the next two or three cycles. We are not able, however, to predict the level of the ensuing minimum.

7.1 Introduction

Explosive events on the Sun, such as flares and coronal mass ejections, which are manifestations of solar magnetic activity, have an important impact on the heliosphere. They are the source of energetic particles, which are a hazard in space, and give rise to magnetic storms that interfere with communications both in space and on the ground. It is therefore

^aETH Zürich, 8092 Zürich, Switzerland

^bSwiss Federal Institute of Aquatic Science and Technology, Eawag, 8600 Dübendorf, Switzerland

^cDepartment of Applied Mathematics, University of Leeds, Leeds, UK

^dDepartment of Applied Mathematics and Theoretical Physics, University of Cambridge, Cambridge, UK

necessary to understand the origin of the Sun's cyclic activity, and – if possible – to predict its future course. The solar cycle is driven by an oscillatory hydromagnetic dynamo in the Sun's interior (*e.g.*, Tobias & Weiss 2007). As yet there is no realistic numerical model of this nonlinear dynamo, and only parameterized mean-field models are available. Predictions, even of the peak level of the next cycle, are notoriously controversial — see Schüssler (2007) and the references therein. Attempts using plausible, yet poorly constrained, mean-field dynamo models yield widely disparate forecasts (Dikpati *et al.* 2006; Choudhuri *et al.* 2007) demonstrating the sensitivity of such forecasts to details of the model and assumptions (Bushby & Tobias 2007). An alternative approach is to use precursor methods, based for example on measurements of the Sun's polar field or the geomagnetic *aa* index (*e.g.*, Schatten 2005; Hathaway & Wilson 2006), or else to rely on timeseries analysis, utilizing either neural networks, attractor reconstruction or statistical methods (*e.g.*, Sello 2001; Lundstedt 2006). These difficulties in prediction are paralleled by those faced by meteorologists attempting to predict the next day's weather.

One can also examine the record of solar activity since the invention of the telescope, as measured by the sunspot number R (*e.g.*, <http://sidc.oma.be/sunspot-data/>). Quite what one might then predict for the next cycle depends on the length of the past record that one chooses to examine. If one takes into account only the last half dozen cycles then one would predict an increase in the level of activity. If instead one takes the record back to the beginning of the 18th century one recognises that the eleven year (Schwabe) cycle is modulated on a longer ~ 90 years (Gleissberg) timescale, and one would therefore forecast a decrease in activity; indeed, there are suggestions, both from the activity record and from measurements of total solar irradiance (Lockwood & Fröhlich 2007), that this decline has already begun. However, the seventeenth century saw the occurrence of the Maunder minimum, when sunspots virtually disappeared (Ribes & Nesme-Ribes 1993), and one is also led to ask whether such a catastrophic drop in activity might recur in the immediate future.

Although there are no reliable records of sunspot activity prior to 1610, there are – fortunately – alternative proxy records that extend back for tens of thousands of years into the past. Galactic cosmic rays impinging on the Earth's atmosphere give rise to the production of cosmogenic radioisotopes such as ^{10}Be and ^{14}C . Cosmic rays are deflected by magnetic fields in the heliosphere and their incidence and hence the production rates of these isotopes are modulated by changes in solar magnetic activity. Variations in production rates of ^{14}C and ^{10}Be have been determined precisely for the last 10,000 years (Stuiver & Braziunas 1988; Vonmoos *et al.* 2006). Recurrent grand minima interspersed with grand maxima feature throughout both of these records.

Our aim in this paper is to carry out a statistical analysis of the ^{10}Be record that enables us to estimate the future duration of the current grand maximum and to predict the likelihood of a subsequent grand minimum. A different approach, using the ^{14}C record to reconstruct sunspot numbers, has been followed by Solanki *et al.* (2004) and Usoskin *et al.* (2006, 2007). In the next section we introduce the solar modulation potential ϕ as the relevant measure of solar magnetic activity and describe the record derived from the GRIP ice-core in Greenland, which extends over 9000 years with a mean temporal resolution of about 5 years. In section 7.3 we carry out a statistical analysis of the data and then summarise our conclusions in the final section.

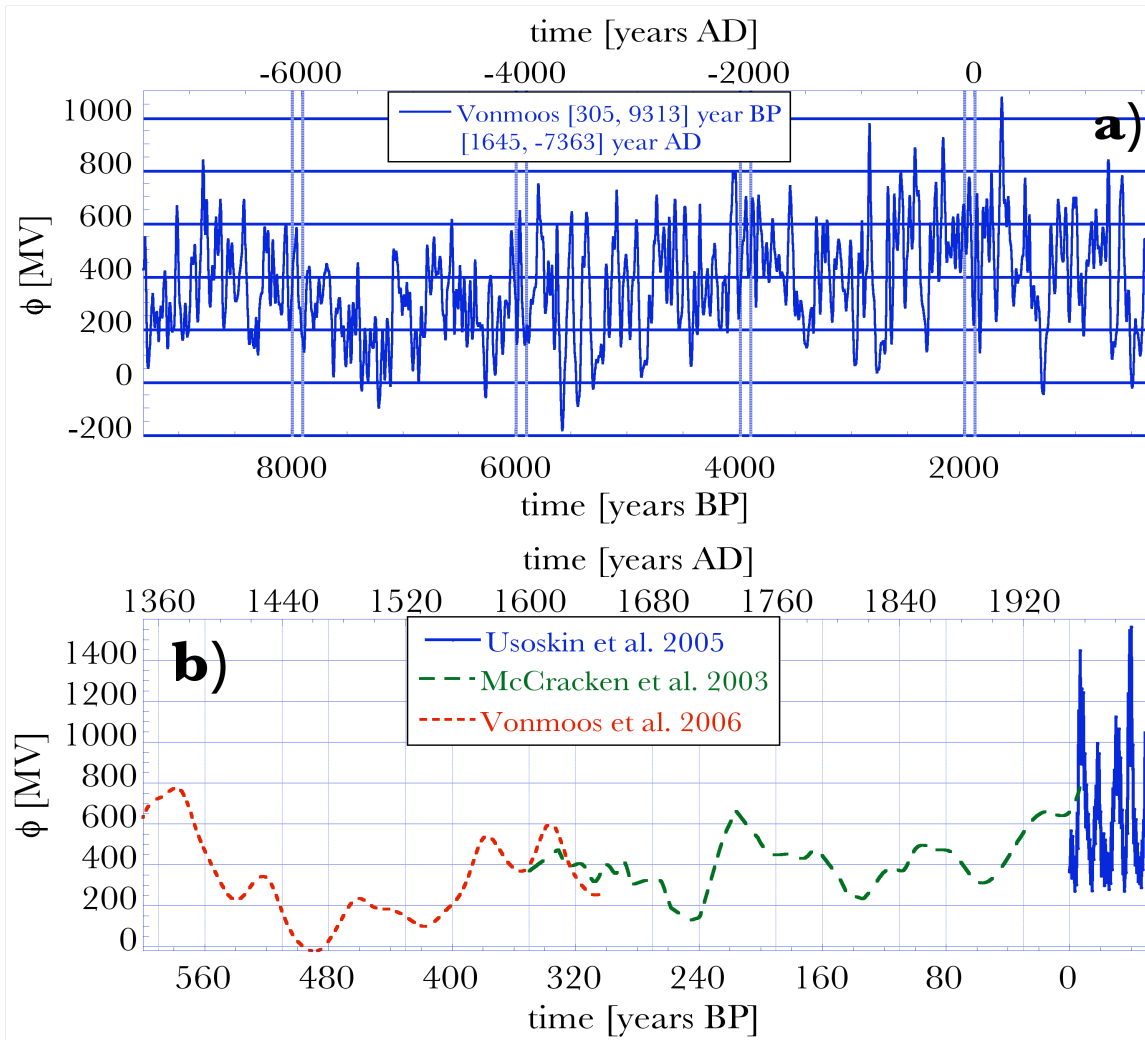


Figure 7.1: Records of solar activity. (a) Timeseries for ϕ constructed from the GRIP ice-core and filtered to eliminate the 11 year Schwabe cycle (Vonmoos *et al.* 2006). (b) Composite timeseries showing the modulation potential ϕ , after compensating for the use of different Local Interstellar Spectrum (LIS) models (Steinhilber *et al.* 2008). Shown are the smoothed annual means of ϕ from the GRIP ice-core – red), from the South Pole (green), and the annual means from direct measurement of cosmic rays.

7.2 The Solar Modulation Function from the GRIP ^{10}Be Record

The record that best represents the role of open solar magnetic fields in deflecting cosmic rays is the solar modulation potential ϕ , which can be derived from either the ^{10}Be or the ^{14}C production rates after correcting for variations in the geomagnetic field (see *e.g.*, Vonmoos *et al.* 2006; Usoskin *et al.* 2007). Figure 7.1(a) shows the GRIP timeseries for ϕ from 9313 to 305 BP (7363 BC to 1645 AD). This primary data-set has been subjected to smoothing with a binomial filter over 61 points, which corresponds approximately to a 40-year low-pass filter and eliminates the basic Schwabe cycle. It is apparent that there are many grand minima and maxima in this record. Frequency analysis reveals the presence of a number of significant periodicities, namely around 200 years (de Vries) and 2300 years (Hallstatt) (Tobias *et al.* 2004). In order to extend this record up to the present, we have constructed a composite timeseries $\phi(t)$ by combining the GRIP record with the ^{10}Be record from the South Pole spanning the interval from 1600 to 1957 (which has itself been filtered using a 22 year running mean) (McCracken *et al.* 2004) and the record derived from direct measurements of cosmic rays by neutron monitors from 1950 to 2004 (Usoskin *et al.* 2005) (see Fig. 7.1(b)). The latter records have been corrected to take account of the different Local Interstellar Spectrum Models that had been adopted and to ensure compatibility with the Local Interstellar Spectrum Model that was used to obtain the GRIP timeseries (Steinhilber *et al.* 2008).

Inspection of Fig. 7.1(a) indicates a long period trend which may contain climatic and geomagnetic components. This may be the cause of the slight divergence of the ^{10}Be from the ^{14}C reconstructions in the early parts of the records (Vonmoos *et al.* 2006). We therefore remove this linear trend from the composite data-set and add a constant offset so that the time series matches the accurately determined value of ϕ for 2004. We then impose a high-pass filter to remove periods longer than 3000 years, together with a 40 year low-pass filter. The most recent part of the composite filtered data-set is shown in Fig. 7.2(a). This record shows a marked double-hump structure which corresponds to the sunspot maxima around 1960 and 1980-1990. It is worth noting that in this composite reconstruction of the modulation potential the current grand maximum in activity (with $\phi \approx 700$ MV) is by no means unique – it has been exceeded three times in the past thousand years (McCracken *et al.* 2004) – in contrast to some reconstructions of R itself (Solanki *et al.* 2004; Usoskin *et al.* 2007). In this filtered record the variable ϕ is normally distributed, as shown by Fig. 7.2(b), with a mean of 478 MV and a standard deviation of 174 MV. The definition of a grand extremum is arbitrary, provided that the Maunder minimum appears as a grand minimum. We choose to adopt the following criterion: the variable ϕ should spend 60% of the time outside grand extrema, with 20% in grand maxima and 20% in grand minima. It follows then that a grand minimum is an event with $\phi \leq \phi_{min} = 340$ MV, while a grand maximum is an event with $\phi \geq \phi_{max} = 616$ MV. These levels are indicated as dashed lines in Fig. 7.2. Note that the Dalton minimum (at 1810) just survives.

Inspecting the records in Fig. 7.1(a) and 7.2, we observe that grand maxima and grand minima have a characteristic timespan of twenty to sixty years (*cf.* Steinhilber *et al.* 2008), and so we might naively predict that the current grand maximum, which has already lasted around eighty years, will terminate soon. The next section will contain a precise statistical analysis of the distributions in order to obtain an expected lifetime for this grand maximum.

7.3 Statistical Analysis

Figure 7.3(a) is a scatter-plot of the durations of the 66 grand maxima in the record, ordered from the most recent to the earliest. We see immediately that all but two of these have a duration of less than 80 years. The longest, with a duration of 95 years, occurred around 300 AD and is apparent in Fig. 7.2(a). The binned distribution for the lengths of maxima is shown as the heavy line in Fig. 7.3(b). Since the current grand maximum has already lasted for 80 years, it is not possible to make a very precise statement directly from the distribution, owing to the paucity of data at its high end. However, if the current maximum lasted for two more solar cycles then it would be the longest such event in the past 10,000 years. Is that likely? We answer this question by fitting the data to appropriate statistical distributions and calculating the life expectancy of the current grand maximum. Two statistical distributions are good candidates for this purpose (Ryan and Sarson 2007), the gamma distribution and the lognormal distribution. We estimate the parameters for the gamma distribution

$$f(x; a, b) = \frac{x^{a-1} \exp(-x/b)}{b^a \Gamma(a)}, \quad (7.1)$$

using the maximum likelihood method, to be $a = 2.20$, $b = 13.13$. Binned values for this distribution are also shown in Fig. 7.3(b). We carry out a χ^2 goodness of fit test on the binned distributions and find that the fit is highly significant at the 5% level. From this gamma distribution we find that the life expectancy of the current grand maximum, given its present duration, is 95 years, i.e. it is expected to end in fifteen years. Note that such a prediction is relative to given filtered data as well as to our arbitrary definition of a grand extremum. If ϕ_{max} is lowered (raised) then the life expectancy will be increased (decreased): for instance, if we were to set $\phi_{min} = 400$ MV and lift ϕ_{max} to 556 MV then the current lifetime would be 87 years, with a remaining life expectancy of 14 years.

There are two sources of error¹ in these predictions. Each of the original data points for ϕ has an estimated error of 10% (Vonmoos *et al.* 2006) but these errors are dominated by those introduced by fitting a gamma distribution. The 95% confidence intervals for a and b are [1.60, 3.02] and [9.18, 18.79], respectively. Using a Monte Carlo technique, we estimate that the resulting rms error in the life expectancy is 3 years (Fig. C.3). We have also confirmed that the remaining life expectancy is not significantly altered if the 40-year low-pass filter is replaced by a 60-year low-pass filter, or if the high-pass filter is omitted. Thus these estimates, based on a gamma distribution, are apparently robust. We have carried out a similar procedure for the lognormal distribution, which is also shown in Fig. 7.3(b). The fit for this distribution is less satisfactory than for the gamma distribution, as is obvious from the figure, and is barely significant at the 5% level. The corresponding life expectancy for this poorly matched case is 116 years, with an estimated error of about 7 years. Thus we have estimates of the remaining lifetime of the current grand maximum that range from fifteen to thirty-six years, based on these statistical tests. Given the relatively short timescale associated with the ending of the current grand maximum we may ask how deep the next relative minimum is likely to be, and speculate whether it will be deep enough to qualify as a grand minimum. Figure 7.3(c) shows a scatter-plot of the level of each grand maximum in the filtered ϕ record versus that of the subsequent relative minimum. Clearly there is no correlation between these variables and so it is impossible to make any precise predictions

¹In Appendix C, I discuss the the procedure followed to estimate the errors

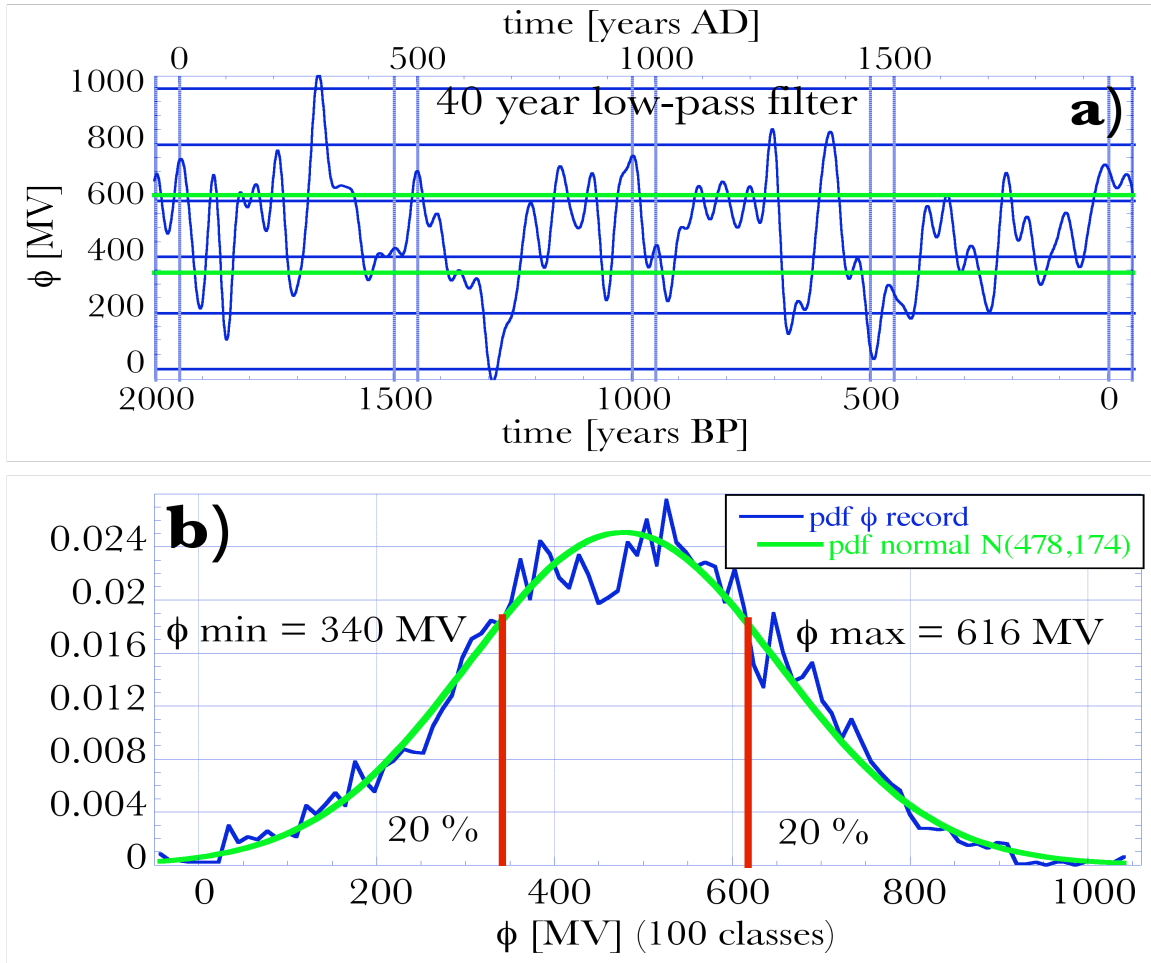


Figure 7.2: (a) Section of the filtered composite timeseries for the modulation potential ϕ , after imposing a 3000 year high pass filter and a 40 year low-pass filter. (b) Probability distribution for the measured values of the modulation potential ϕ , compared with a normal distribution. The data are normally distributed about a mean 477.8 MV and standard deviation 174 MV.

for the depth of the ensuing minimum. We can only infer that there is a 40% probability that the current grand maximum will actually be succeeded by a grand minimum. Our treatment here has focused on the history of the solar modulation function ϕ , as derived from the ^{10}Be record. While these results agree qualitatively with those of Solanki *et al.* (2004) and Usoskin *et al.* (2007), direct comparison is not straightforward because of the different data-sets used, different definitions of grand maxima and different filtering techniques applied. These authors likewise find that the current grand maximum has lasted unusually long (65 years) and they expect that it will terminate within the next half-century. They compare the distribution of the sunspot number R with a normal distribution and fit both power law and exponential distributions to the durations of grand maxima and grand minima, as well as to the intervals between them. We consider that the gamma distribution is more appropriate and, unlike them, we have gone on to predict the life expectancy of the current episode of extreme activity.

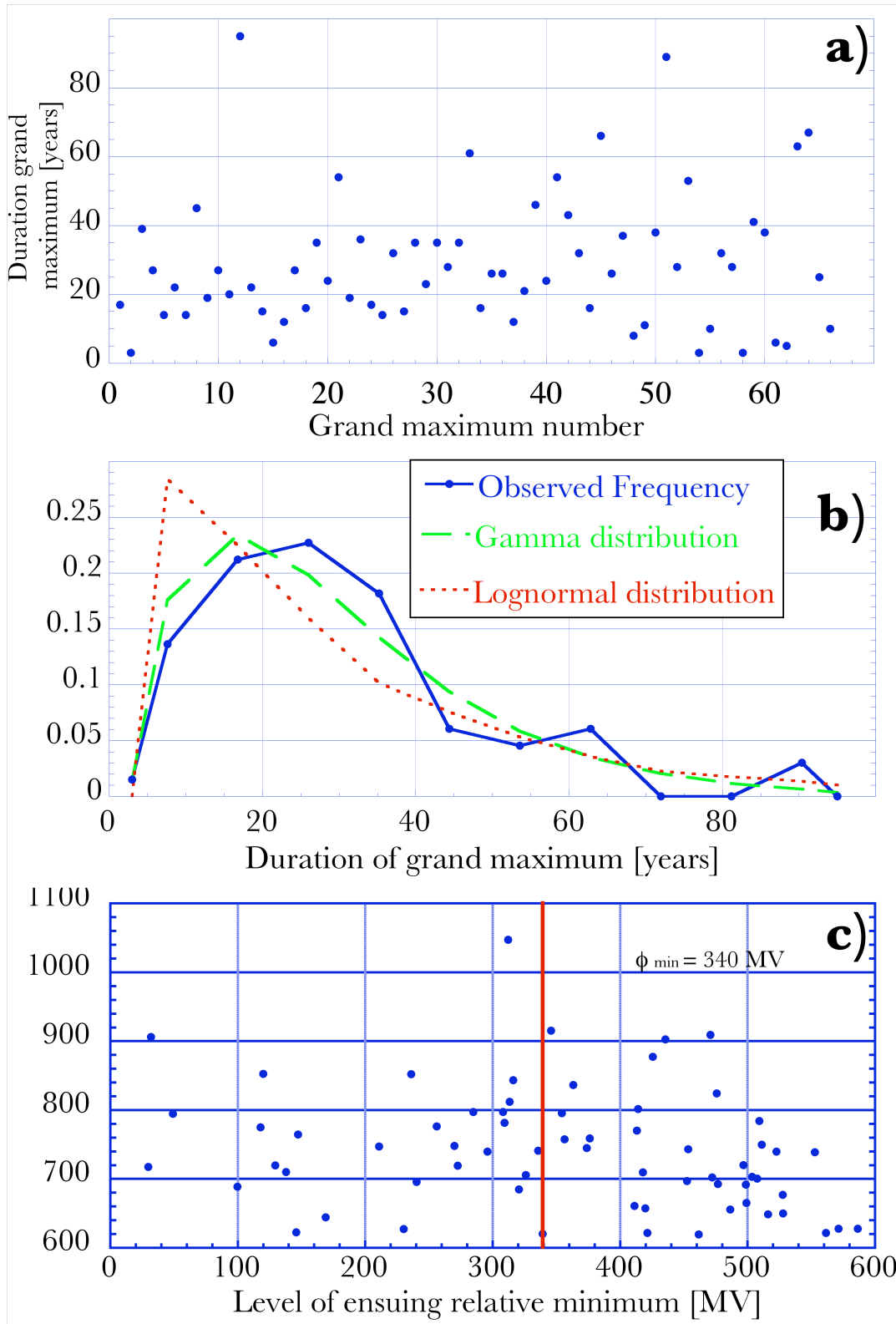


Figure 7.3: Distribution of the durations of grand maxima in activity. (a) Scatter plot for durations of grand maxima, listed consecutively back in time. Note that there are only two examples with durations longer than that of the current grand maximum. (b) Binned distribution for durations of grand maxima. Superimposed are the fitted gamma (green) and lognormal (red) distributions. (c) Scatter plot relating the level of a grand maximum in ϕ (as ordinate) to that of the subsequent relative minimum. Grand minima lie to the left of the heavy vertical line. No significant correlation is visible in the data

7.4 Conclusion

We have attempted to estimate the future life expectancy of the current grand maximum in solar magnetic activity using three methods: visual inspection of the data, comparison with the duration of the longest maximum and, most reliably, estimation from two different statistical distributions. Although there is some scatter in our estimates of the future life expectancy, all three methods predict that this bout of enhanced activity will not last longer than two or three cycles, with the more reliable methods giving shorter predictions. We therefore expect that the current grand maximum will come to an end within the next few solar cycles. If the next maximum of the Schwabe cycle (around 2012) continues the downward trend of its predecessors then the message will be clear. Although it is possible that the activity level will just cross the threshold for being considered a grand maximum, to return almost immediately, we consider it more likely that the level of activity will either regress to the mean or plunge into the next grand minimum. We await the outcome with keen interest. If it turns out that there is a precipitate decline in solar magnetic activity, it may be expected to have a slight cooling effect on the earth's atmosphere; this will, however, be insignificant compared with the global warming caused by greenhouse gases.

Chapter 8

Can we forecast the next grand minimum in solar activity?

J.A. Abreu^{a,b}, J. Beer^b, A. M. Berggren^c, A. Ferriz-Mas^{d,e}
submitted to *The Astrophysical Journal*, 2009

Abstract

In a previous work we carried out a statistical analysis of the solar modulation potential ϕ as reconstructed from the proxy record of cosmogenic ^{10}Be abundances in the GRIP ice core; we found that the current grand maximum in solar activity is only expected to last for a further 15–36 years. In the present paper, we have made use of the same run of ϕ in order to study the likelihood of a subsequent grand minimum following the current grand maximum (such as the Maunder minimum from 1645 to 1715). Here we have applied to the intervals between consecutive minima of ϕ the same statistical procedure as in the previous paper. Our main result is that we expect the current decline in solar activity to reach a minimum within the next 80–100 years. We also hypothesize about the possible origin of grand minima in the framework of a dynamo model consisting of two separate dynamos operating each in a separate layer; the decoupling between both dynamos would be the explanation for the prolonged activity minima that have occasionally appeared in the Sun’s magnetic history.

8.1 Introduction

The sunspot record since 1610 shows cycles of magnetic activity with an irregular distribution of amplitudes and with a period around 11 years; they are modulated on longer timescales and were interrupted by the Maunder minimum in the 17th century. Solar magnetic activity is associated with the emergence of magnetic flux at the solar surface, giving rise to sunspots, flares, coronal mass ejections and other magnetic manifestations; solar activity is also thought to be responsible for changes in solar irradiance. Evidence based on paleoclimate records points to a causal relationship between solar activity variations and climate changes (*e.g.*,

^aETH Zürich, 8092 Zürich, Switzerland

^bSwiss Federal Institute of Aquatic Science and Technology, Eawag, 8600 Dübendorf, Switzerland

^cEnvironment and Landscape Dynamics Uppsala University, Uppsala, Sweden

^dInstituto de Astrofísica de Andalucía (IAA/CSIC), Granada, Spain

^eDepartamento de Física Aplicada, Universidade de Vigo, Ourense, Spain

Wanner *et al.* 2008). In order to understand how the Sun can affect the climate, there is a number of questions which need to be answered first. The sensitivity of climate to solar irradiance changes is not well understood, as it is not yet understood how physical processes taking place inside the Sun lead to irradiance variations (*e.g.*, Lean *et al.* 1995). The use of proxy data for solar activity –such as cosmogenic radioisotopes– may shed some light.

The main aim of this paper is to estimate the likelihood that the current *grand maximum* will be followed by a subsequent *grand minimum*. Predictions, even of the peak level of the next cycle, are notoriously controversial (see, *e.g.*, Schüssler 2007 and references therein). The ultimate reason for the difficulty of tackling this problem is that up to date no realistic model for the operation of the solar dynamo exists (actually, there is not even agreement among solar physicists on where the dynamo process takes places; see *e.g.*, Brandenburg 2005). Most studies of the dynamo problem rely on the so-called *mean-field approach*, which is highly parameterized, cannot be derived from first principles and is not generally accepted. Some recent attempts of predictions employing more or less plausible dynamo models (but, in any case, based on the mean-field approach), yield widely disparate forecasts (*e.g.*, Dikpati *et al.* 2006; Choudhuri *et al.* 2007) demonstrating the sensitivity of such forecasts to details of the model and to the assumptions involved (Bushby & Tobias 2007).

An alternative approach is to use *precursor methods* based, for example, on measurements of the Sun’s polar field, or the geomagnetic *aa* index (*e.g.*, Schatten 2005; Hathaway & Wilson 2006), or else to rely on time series analysis, utilizing either neural networks, attractor reconstruction or statistical methods (see *e.g.*, Sello 2001; Lundstedt 2006). These difficulties in prediction are similar to those faced by meteorologists attempting to predict weather for the next few days. In contrast to the sunspot record, alternative proxies like cosmogenic radionuclides extend back tens to thousands of years in the past. They show many grand maxima and grand minima, hence providing us with valuable information about the history of solar activity. This makes cosmogenic radionuclides optimal proxies to answer the question of whether the next grand minimum in solar activity may be forecast.

The plan of the paper is as follows. In section 8.2 we present the solar modulation potential, ϕ , which was reconstructed basically from ^{10}Be abundances in the GRIP¹ ice core, and discuss the long-term modulation of solar activity. In section 8.3 we carry out a statistical analysis of our data set. We shall not restrict ourselves to presenting a long-term prediction of solar activity; in section 8.4 we hypothesize/speculate about the possible origin of *grand minima* in solar magnetic activity and interpret our data within a specific dynamo framework based on the assumption of two separate dynamo processes taking place inside the Sun, one responsible for large-scale magnetic fields (sunspots) and another one responsible for the generation of weak, irregular fields. The idea was first put forward by Schmitt *et al.* (1996) and further developed by the authors. Our conclusions are presented and discussed in section 8.5.

8.2 Long-term modulation of solar solar activity

In the record of sunspot numbers one recognises that the eleven year (Schwabe) cycle is modulated by a longer ~ 90 -year cycle (Gleissberg). Although it cannot be excluded that there could be further modulations on longer time scales, the sunspot record is too short to see them. Fortunately, alternative solar activity proxies can be reconstructed from cosmogenic

¹Greenland Ice Core Project

radionuclides expanding the history of solar activity for several thousand of years. In the present work we used as a proxy for solar activity the so-called *modulation potential* ϕ , which was first introduced by Gleeson and Axford (1968). The modulation potential ϕ is a measure of the role of the open solar magnetic field in deflecting cosmic rays. Here we have used the same composite of ϕ as we did in Abreu *et al.* (2008); the modulation potential was constructed by combining the GRIP record (Vonmoos *et al.* 2006) with the ^{10}Be record from the South Pole, spanning the interval from 1619 to 1950 (which has itself been filtered using a 22 year running mean, McCracken *et al.* 2004) and the record derived from direct measurements of cosmic rays by neutron monitors from 1950 to 2004 (Usoskin *et al.* 2005). The latter records have been corrected in order to account for the different Local Interstellar Spectrum Models –*i.e.*, for the cosmic ray flux outside the heliosphere– that had been used by the various authors and in order to ensure compatibility with the specific Local Interstellar Spectrum Model that was used to derive the GRIP time series (Steinhilber *et al.* 2008). Shown in Fig. 8.1 are the run of ϕ (green curve) and of the ^{14}C production rate (broken blue line). Additionally we show the ^{10}Be flux (red curve) as determined from a new record from the Greenland NGRIP data (Berggren *et al.* 2009). We observe that all time series show excellent agreement with the sunspot numbers R (solid blue line; <http://sidc.oma.be/sunspot-data>): They display the same increasing trend, starting from the end of the Maunder minimum until present. The Dalton minimum around 1800, as well as the small minimum around 1900, are both well represented in our data. Note that the relative amplitudes are also in good agreement. A spectral analysis of the time series of the reconstructed potential modulation ϕ shows three prominent periodicities, *viz.* at 2200 (Hallstatt cycle), at 205 years (de Vries cycle) and at 980 years, respectively; see Table 8.1. These three periods are the main contributors to the long-term oscillation in the time series of ϕ . The red curve in Figs. 8.3 and 8.4 describes this oscillation. It was obtained by fitting a sum of harmonic functions at those periods to the original data. The amplitudes and phases were estimated by applying Bayesian probability theory (Bretthorst 1988a,b). The time series of ϕ shows that the solar activity has increased since the end of Spörer’s minimum (1420 to 1570 A.D.) till present. Looking at the whole set of ϕ data we see not only many maxima and minima, but also notice that the minima tend to form clusters which are separated approximately by intervals of 2300 years.

8.3 Statistical analysis

An extrapolation of the fitted long-term trend into the future, as illustrated in Fig. 8.5, shows that the mean-level activity will reach values similar to those of the *little ice age* (1250 to 1850 A.D.) around the year 3500. However, we also observe in Table 8.1, that the level of solar activity is also modulated at higher frequencies, such as the Gleisberg cycle. In order to account for these higher frequencies we have employed the same method that we used in Abreu *et al.* (2008) to predict the end of the current ‘grand maximum’. We use the same definition of a ‘grand extremum’ as in Abreu *et al.* (2008), *viz.* the variable ϕ should spend 60% of the time outside grand extrema, with 20% in a grand maxima and 20% in a grand minima. Therefore, a ‘grand minimum’ is an event with $\phi < \phi_{min} = 340$, while a ‘grand maximum’ is an event with $\phi > \phi_{max} = 616$. Next we consider the distribution of the waiting times between consecutive ‘grand minima’ of the function ϕ and fit a gamma distribution to the waiting times distribution in order to calculate the life expectancy of the

current time span between *today* (whereby today means the year 2004) and the end of the last minimum.

The gamma distribution is given by

$$f(x; a, b) = \frac{x^{a-1} \exp(-x/b)}{b^a \Gamma(a)}, \quad (8.1)$$

By employing the maximum likelihood method we estimate the parameters a and b to be $a = 1.24$ and $b = 96.86$. Binned values for this distribution are shown in Fig. 8.6. We carry out a χ^2 goodness of fit test on the binned distributions and find that the fit is highly significant at the 5% level. From this gamma distribution we find that the life expectancy of the random variable ‘waiting time between grand minima’ is 286 years (taking into account that the last grand minimum ended in 1821 A.D.). Thus we expect the next ‘grand minimum’ to happen around the year 2100. Note that such a prediction is relative to the given filtered data as well as to our arbitrary definition of a *grand extremum* (see, Abreu *et al.* 2008). We note that this result is in good agreement with the prediction presented by Clilverd *et al.* (2003), whose calculations are based on different proxies such as ^{14}C , the geomagnetic *aa index* and sunspots. As can be seen in Fig. 8.5, the long-term curve (in red) shows a minimum at the predicted year too.

8.4 A solar dynamo model: Data interpretation in the framework of dynamo theory.

Theoretical considerations suggest that the toroidal magnetic flux tubes which erupt at the solar surface in form of sunspots are stored, prior to eruption, in a thin layer of overshooting convection at the boundary between the convection zone proper and the radiative region (see *e.g.*, Spiegel & Weiss 1980; Galloway & Weiss 1981; van Ballegoijen 1982; Schüssler 1983). The most relevant among the theoretical arguments in favour of this idea is probably the role of magnetic buoyancy. Since a magnetic field gives rise to an effective magnetic pressure, a flux tube surrounded by almost field-free plasma becomes buoyant. Parker (1955a) and Jensen (1955) suggested that magnetic flux is brought to the solar surface through the action of magnetic buoyancy. Buoyancy can be a very efficient mechanism in expelling magnetic flux to the solar surface and this was pointed out by Parker (1975), who showed by means of a simple model that a flux tube with an initial field strength of 100 G (and in thermal equilibrium with the surroundings) would leave the convection zone within 1 or 2 years.

Many solar physicists think that the field strength of the stored magnetic field prior to eruption is close to 10^5 G, a value which is much larger than the equilibrium value between the kinetic energy density of turbulent convective and the magnetic energy density (the *equipartition value* is roughly 10^4 G for the conditions at the bottom of the solar convection zone). There are, at least, three independent arguments leading to this value of 10^5 G: (i) Flux tubes with weaker fields would erupt at too high latitudes due to the action of the Coriolis force (see *e.g.*, Choudhuri & Gilman 1987). (ii) Large fields are required to account for the observed tilt angles of active regions (*e.g.* Caligari *et al.* 1995), to avoid excessive weakening of rising flux tubes and also to give account of the coherence of sunspots (*e.g.*, Moreno-Insertis *et al.* 1995). (iii) This value consistently comes out from the linear stability analysis of flux tube equilibria (Ferriz-Mas & Schüssler 1993, 1995). If the toroidal flux

system that eventually produces active regions is located at the bottom of the convection zone, how does it move to the surface to originate sunspots? The answer is that this magnetic field must first become unstable. The onset of instability occurs for a *critical value* of the magnetic field strength, the precise value depends on the exact depth within the overshoot layer (through the properties of the stratification, whereby the superadiabaticity is the most relevant parameter), on the angular velocity distribution and on latitude. For conditions in the solar overshoot layer, the stability analysis of toroidal flux tubes yields that this critical value is close to 10^5 G. A linear stability analysis provides the proper initial conditions for numerical simulations of the emergence of magnetic flux loops through the convection zone. Once an unstable loop has entered the superadiabatic part of the convection zone, the subsequent evolution becomes nonlinear and very fast, so that numerical simulations are necessary to follow its rise towards the surface. It is generally accepted that the solar activity cycle is the result of a hydromagnetic dynamo and that sunspots are the result of the emergence at photospheric levels of large bundles of toroidal magnetic flux, but here the consensus among solar physicists ends. Even on the apparently simple question of ‘where the solar dynamo process is located’ there is no agreement (Brandenburg 2005).

The *conventional approach* is the so-called ‘mean-field dynamo theory.’ In this approach, the two basic ingredients are differential rotation plus turbulent convection in the presence of rotation. Differential rotation regenerates the toroidal field from the poloidal field (this is the so-called Ω -effect), while cyclonic convection regenerates the poloidal field from the toroidal field (α -effect). Since Parker (1955b) first put forward the idea of the inductive effect of cyclonic convection, the dynamo mechanism has been typically located in the bulk of the solar convection zone, but since the beginning of the eighties the seat of the dynamo is a permanent topic of discussion. Given the arguments presented above in favour of very strong (*i.e.*, ‘super-equipartition’) fields prior to eruption, it seems clear that the dynamo mechanism responsible for the flux ropes which emerge to originate bipolar active regions cannot be located in the bulk of the solar convection zone. The concentration of magnetic flux into filamentary structures has important consequences for understanding the solar dynamo, since dynamical aspects such as buoyancy and drag force must be taken into account. Does this mean that the solar dynamo is located in the overshoot region? Of course, first of all we must make clear what we understand by ‘solar dynamo.’ Sunspots are possibly the most prominent manifestation of solar activity, but they are not the only one. Although the small-scale magnetic fields associated with bright X-ray points and ephemeral active regions do not show polarity preferences (Golub *et al.* 1981), sunspots obey Hale’s polarity rules. The weak, irregular field observed at the surface may be due to dynamo action in subphotospheric layers (Cattaneo 1999.)

On the base of these facts, the following picture for the solar dynamo was tentatively sketched by Schmitt *et al.* (1996) and Schmitt *et al.* (1998) (see also Ferriz-Mas *et al.* 1994 and the review paper by Schüssler & Ferriz-Mas 2003):

(A) A boundary layer, strong-field dynamo (*i.e.*, with $B > 10^5$ G) is located in the overshoot region (with a depth of the order of 10^4 km) and operates with super-equipartition fields concentrated into flux tubes. Ferriz-Mas *et al.* (1994) showed on the basis of the stability analysis how buoyancy-driven instabilities of toroidal flux tubes may yield a ‘dynamic α -effect’. **(B)** A turbulent weak-field dynamo (*i.e.*, with $B < 10^4$ G) operates in the convection zone. This turbulent dynamo can probably be described in its essentials by means of the classical mean-field approach, with an α -effect due to the combination of Coriolis force

and turbulent convection. Each dynamo would be responsible for different aspects of the solar activity cycle: The ‘strong-field dynamo’ is responsible for the magnetic activity in the form of sunspots, while the ‘weak-field dynamo’ generates a more irregular field. Such weak fields would not disappear during a grand minimum and would maintain a reduced level of activity, as can be seen in the ^{10}Be records (Beer *et al.* 1998) and confirmed by the analysis of the NGRIP data (Berggren *et al.* 2009). Both dynamos are somehow coupled with each other and interchange magnetic flux: the convection zone feeds the overshoot layer with the weak magnetic field ($B < 10^4$ G) dragged downwards by convective cells and possibly by meridional circulation too, while the overshoot region expels magnetic flux tubes into the convection zone in the form of rising, buoyantly unstable tubes. In this model, the intermittency arises as a consequence of the threshold property of a dynamo driven by flux tube instabilities. The data plotted in Fig. 8.1 support the hypothesis of magnetic threshold. We see in the figure that whenever the open magnetic field (as represented by the cosmogenic radioisotopes) becomes too weak, sunspots disappear and a grand minimum takes place. Additionally, visual inspection of the data depicted in Fig. 8.4 and spectral analysis, show that the grand minima tend to form clusters, which are separated approximately by intervals of 2200 years. This could be explained if we admit that the critical value of the magnetic field is modulated at such time scales. Note that the minimum levels of the yearly averaged sunspot numbers also show a long term modulation (Werner Schmutz, personal communication).

8.5 Conclusion

We have performed an statistical analysis of a composite record of the solar modulation potential ϕ , reconstructed principally from the proxy record of cosmogenic ^{10}Be abundances in the GRIP ice core from Greenland. This is a measure of the open solar magnetic field, and extends back for almost 10,000 years, showing many grand maxima and grand minima. We find that the next grand minimum in solar activity will probably occur around the year 2100. This is consistent with the results presented in Abreu *et al.* (2008), namely that the current grand maximum will end in 15-36 years. It is also consistent with the analysis of the long-term modulation displayed by the ϕ record, and it is in good agreement with the prediction given by Clilverd *et al.* (2003). We predict therefore a decrease in solar activity reaching its minimum within aprox. 100 years. Indeed, there are suggestions, both from the activity record and from measurements of total solar irradiance (Fröhlich 2009), that this decline has already begun.

On the basis of these results we find observational support for the idea of (at least) two different dynamo mechanisms operating in the solar interior, as suggested by Schmitt *et al.* (1996) (see also Schmitt & Ferriz-Mas 2003; Schüssler & Ferriz-Mas 2003). The idea is that two distinct (but coupled) dynamos may be operating in two separate regions: a strong-field dynamo operating in the overshoot layer at the bottom of the solar convection zone would be responsible for the large scale toroidal flux system which eventually emerges at the solar surface to form bipolar active regions, while a weak-field dynamo located throughout the convection zone would account for more irregular, weak fields. The possible decoupling between both dynamos could be the explanation for activity minima such as the Maunder minimum from 1645 to 1715. The observed fact that grand minima tend to form clusters is interpreted as an indication for a time variation in the stability of the flux tubes.

We would like to conclude by stressing that the long term behaviour shown in the ϕ composite is an intrinsic part of the solar variability, which should be considered in future solar dynamo models.

Table 8.1: First nine most dominant spectral lines obtained from the spectral analysis of ϕ . The period, phase and amplitudes were estimated by using Bayesian probability theory as described in Bretthorst (1988b). This table illustrates that the solar activity is modulated on longer time scales than the eleven year cycle. The three first lines are the main contributors to the long-term oscillation in the ϕ time series. They were used to generate the red curve in Fig. 8.4 and Fig. 8.5. The last line is the Gleissberg cycle which is also seen in the sunspots record.

Period (yeas)	Phase (rad)	Amplitude (MV)
2204	0.89	70.7
207	1.49	62.2
986	0.75	59.9
350	1.94	-44.6
707	0.89	-39.0
500	1.94	-38.8
105	1.64	38.6
130	2.99	37.9
86	1.79	-37.1

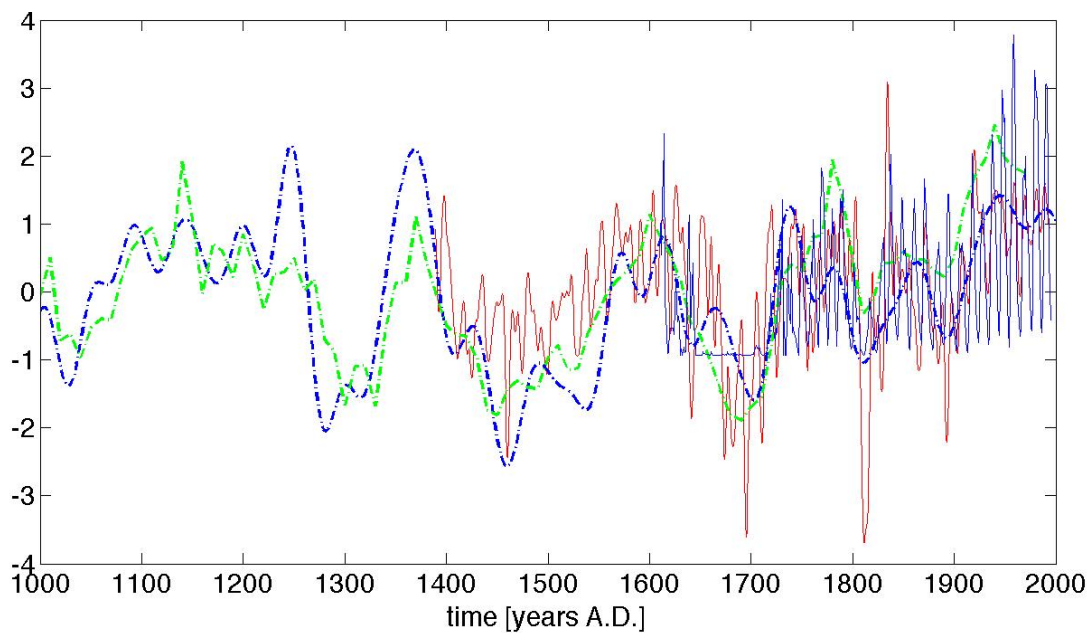


Figure 8.1: Records of solar activity. The green curve shows the composite of the solar modulation potential ϕ (Steinhilber *et al.* 2008). Shown in red is the NGRIP data (Berggren *et al.* 2009) after being linear interpolated to 0.4 y and smoothed with binomial filter over 61 points. The dash-dotted blue curve shows the ^{14}C production rates, while the solid blue curve depicts the sunspot numbers.

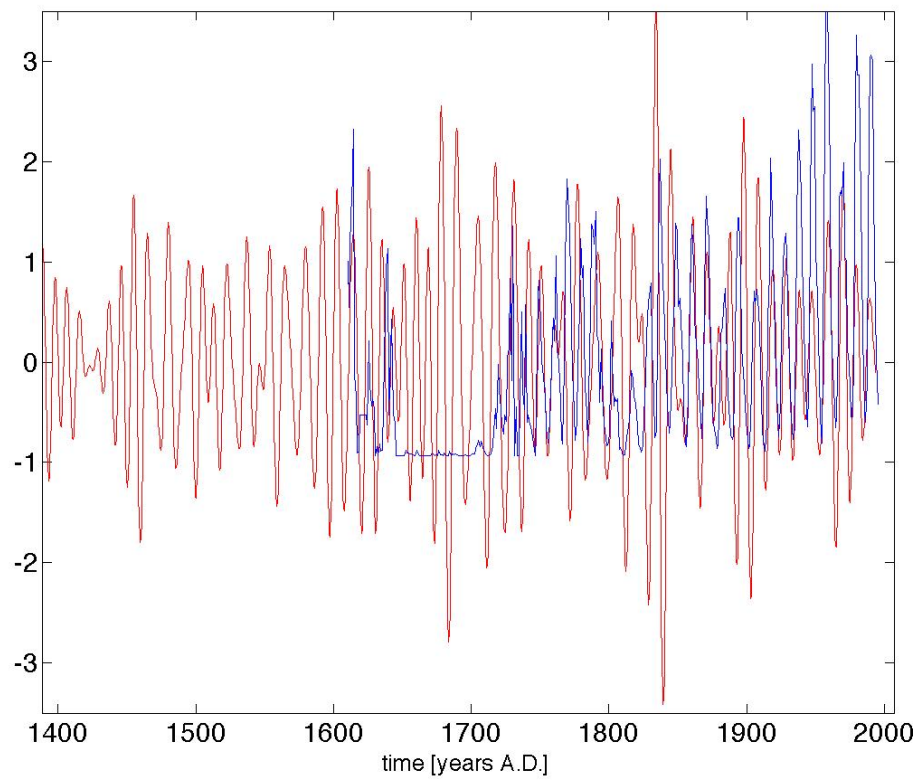


Figure 8.2: Band-pass filtered ^{10}Be fluxes from NGRIP ice core (Berggren *et al.* 2009). The solid blue curve depicts the sunspot numbers.

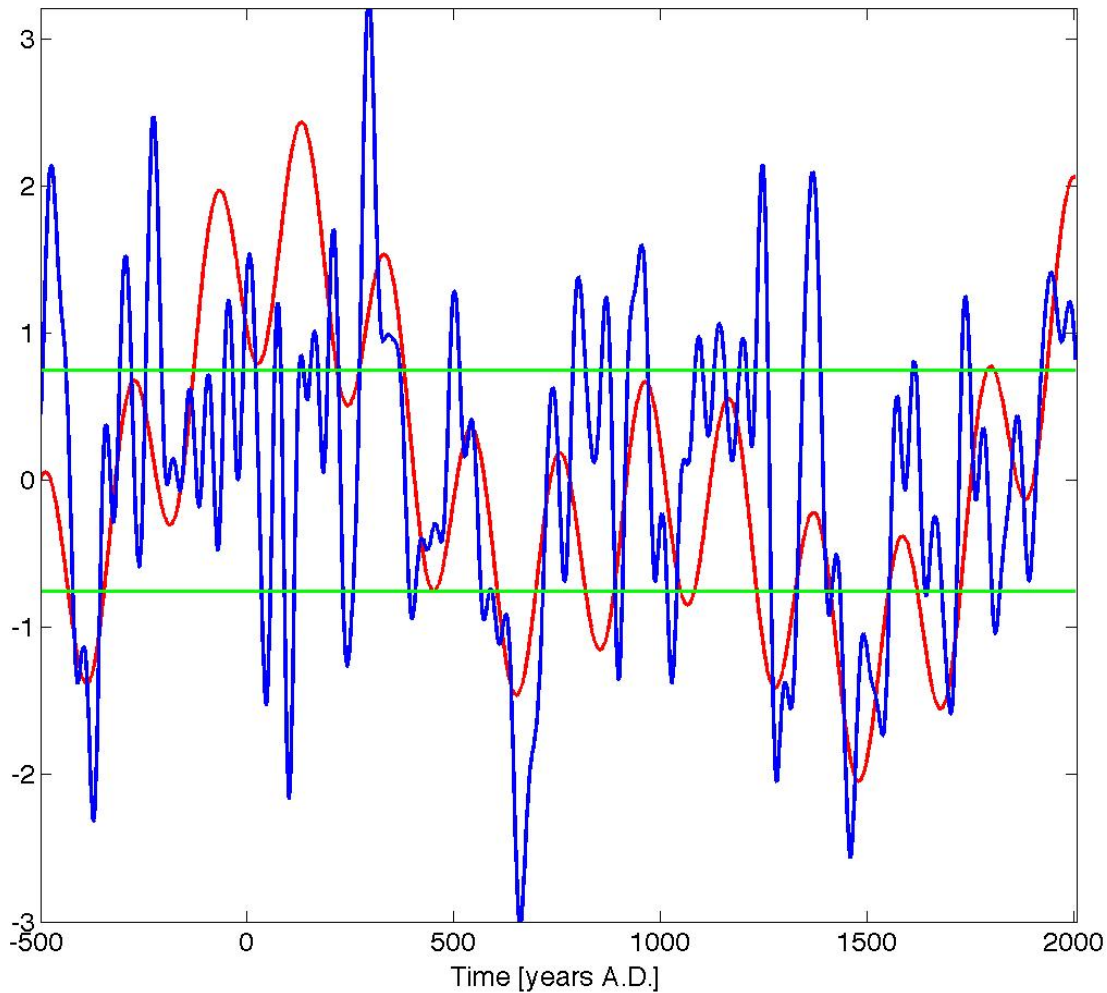


Figure 8.3: The red curve shows the time evolution of the long-term in solar modulation potential ϕ and is given by the superposition of the three most significant frequencies found in the spectral analysis (Table 8.1) (standardized data). The blue curve shows the ϕ composite. The two horizontal green lines correspond to the maximum/minimum levels used to define a grand maximum/minimum as explained in the text.

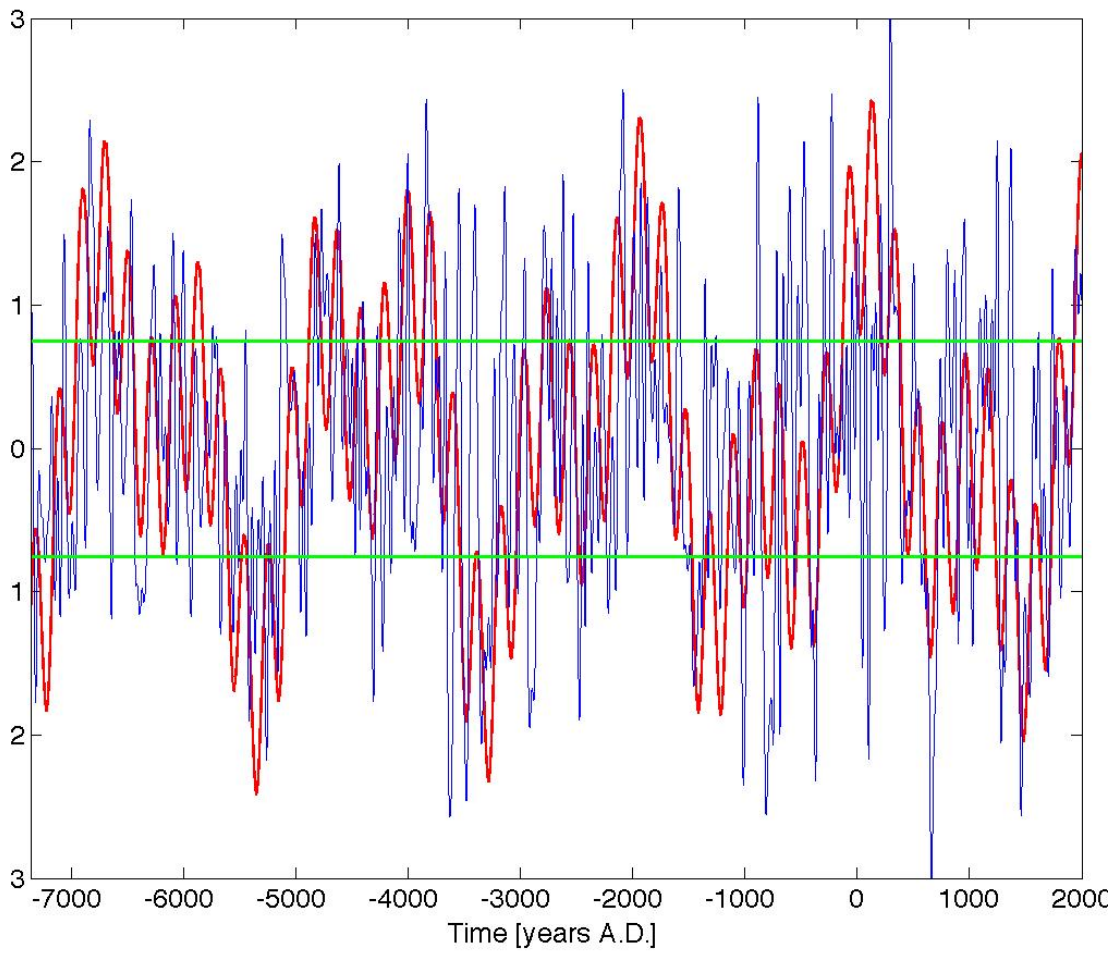


Figure 8.4: Same as Fig. 8.3 but covering the entire time span of ϕ to show the long-term modulation.

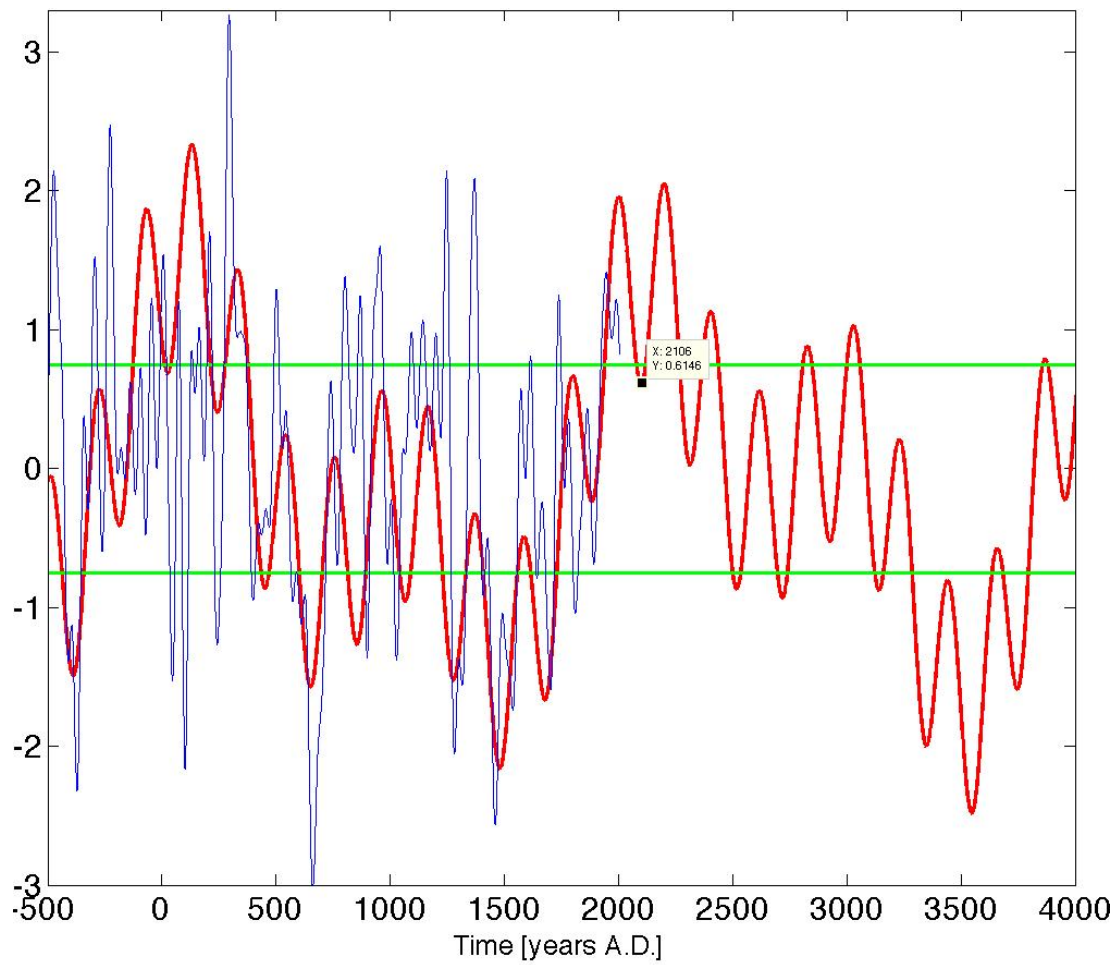


Figure 8.5: An extrapolation into the future of the fitted long-term curve. It shows that mean level activity will reach levels similar to the *Little ice age* around 3500. Note the decrease in recent dates around 2107.

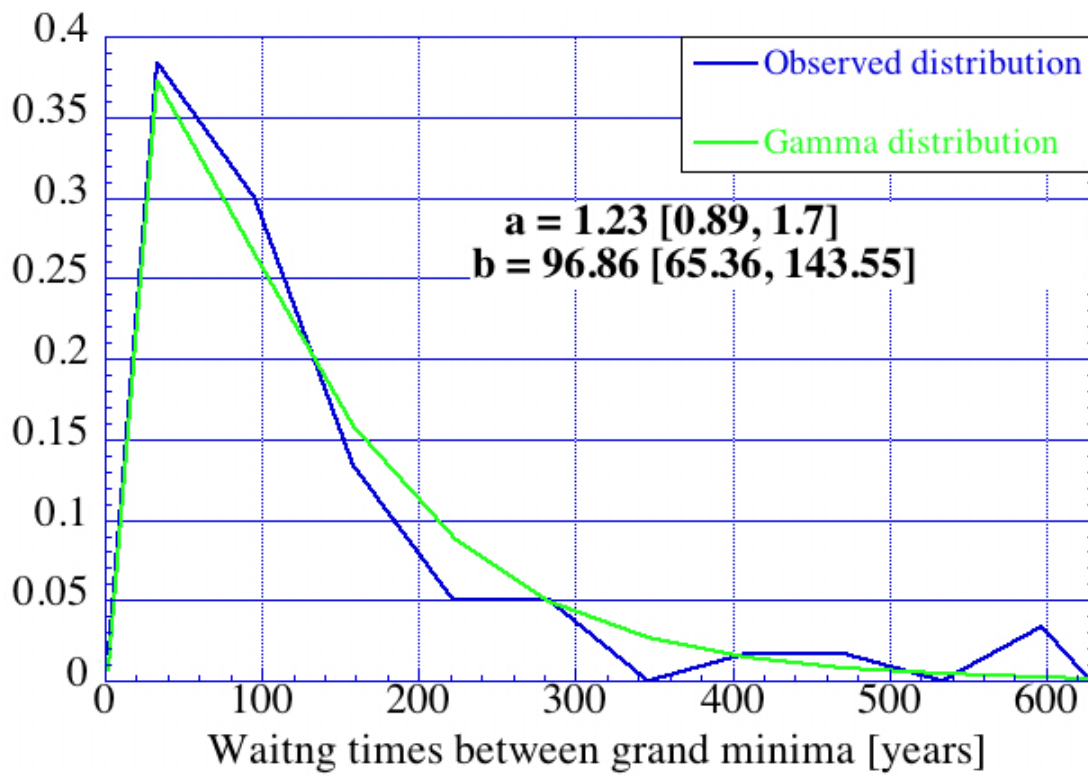


Figure 8.6: Binned distribution for waiting times between grand minima. Superimposed is the fitted gamma (green) distribution.

Chapter 9

Conclusion and Outlook

9.1 Conclusion

In this study we showed by means of the method of principal components (PCA) that it is possible to distinguish between climate induced variations and solar/geomagnetic ones by comparing both radionuclides ^{14}C and ^{10}Be . We also confirmed, based on this mathematical technique the results found by (Heikkilä *et al.* 2008). They applied a GCM to study the relationship between production and meteorology induced changes of cosmogenic radionuclides concentrations in ice cores and found that the production signal is indeed the dominant factor. The ϕ composite used in this work extends back for almost 10,000 years, hence providing us with valuable information about the history of the solar activity. We carry out a statistical analysis of this record and calculate the life expectancy of the current grand maximum. We find that it is only expected to last for a further 15–36 years. We also estimate the probability that the current grand maximum will be followed by a (Maunder-like) grand minimum, hence we expect the next grand minimum occurring around 2100. We therefore predict a decrease in the mean solar activity level reaching a minimum around the year 2100. Our results are consistent with the results both from the activity record (sunspot numbers) and from measurements of total solar irradiance (Fröhlich 2009), that this decline has already begun. This may represent a good example which illustrates the potential of cosmogenic radionuclides for astrophysical applications. Beryllium data from Dye3 ice core, and recently data from NGRIP ice core, show that the mechanism responsible for the solar magnetic activity was still at work during the Maunder minimum, whereas the sunspots disappeared (Beer *et al.* 1998; Berggren *et al.* 2009).

Based on these “observed” facts we suggest two separate full dynamos operating in two separate layers. The possible decoupling between both dynamos could be the explanation for activity minima such as the Maunder minimum from 1645 to 1715.

9.2 Outlook

Next I would like to mention some issues which are worth being investigated in the future.

- A spectral analysis of ϕ shows prominent periodicities like 2200 (Hallstatt cycle), 205 (De Vries), 90 (Gleisberg) and 980 years which are also found in ^{14}C record. We believe that they are of solar origin, therefore dynamo theories should be able to explain why these numbers, exactly as the “eleven” year cycle must be explained as well.

- From the distribution of duration of grand maxima as well as intervals between grand minima. They follow certain distributions, namely, gamma/lognormal distributions. This is telling us something about the physical processes which have generated the data. It should be investigated the reasons why these distributions.
- Some dynamo models are able to reproduce grand minima (Brandenburg & Spiegel 2008). Although this is of course good indication that the models are able to mimic the basic physics involved, we believe, however, that this is not enough because, as pointed above, the grand minima follow certain distributions. This is an important and valuable constrain for that dynamo models.
- The application of PCA to separate production and system effects will help to improve the reconstructions of past solar variability and/or changes in the geomagnetic field. Using an inverse approach, it has the potential to detect large changes in the carbon cycle in general and in the thermohaline circulation in particular.

To conclude, I would like to make some comments on the implications of the solar contribution to climate change. The term “solar activity” is a not well defined term, and its meaning is easily misinterpreted. The Sun manifests its magnetic activity in many different processes and time scales. In 1848 Rudolph Wölf introduced the relative sunspot numbers as a measure of solar activity. Therefore “solar activity” is often used as a synonym of solar activity. However when this term is employed, we should make clear which proxy for magnetic activity we are considering. Therefore if we are using, say the modulation potential, the results can not be interpreted directly in terms of sunspots, because these two indices, although related, their relationship is not known yet. We also must bare in mind that the solar irradiance is related to the solar modulation potential and although we are making improvements on their relationship (Steinhilber *et al.* 2009), this relation is not yet well understood. There are evidences found in paleoclimate records which point to a causal relationship between solar irradiance variations and climate changes. However the internal variability of the climate system has played an important role too, for instance, volcanic eruptions can impact the Earth’s surface (Rind & Overpeck 1993). To understand how the sun can affect the climate, there are many questions which need to be answered first. The sensitivity of climate to solar irradiance changes is not well understood, as it is not yet understood the physical processes within the Sun leading to irradiance variations (Lean *et al.* 1995). Hence the results presented in this work, namely, that we expect a decrease in the solar activity within the next decades cannot direct interpreted in climatological terms, that is to expect a global cooling as a consequence of decrease in solar activity.

Appendix A

Influence of the residence time on the amplitude and the phase of the production signal

In this appendix a simple model of the atmosphere is used in order to show the influence of the residence time on the measured nuclide concentrations. We apply the continuity equation to the atmosphere.

$$\left. \frac{\partial \rho_{Be}}{\partial t} \right|_{\mathbf{x}} = Q(\mathbf{x}, t) - \text{div } \mathbf{J}_{Be}(\mathbf{x}, t), \quad (\text{A.1})$$

where:

$\rho(\mathbf{x}, t) \equiv$ atmospheric concentration in the position \mathbf{x} at the time t .

$Q(\mathbf{x}, t) \equiv$ production rate in the position \mathbf{x} at the time t .

$\mathbf{J}(\mathbf{x}, t) \equiv$ mass flux density $\rho(\mathbf{x}, t) \vec{v}(\mathbf{x}, t)$, where \mathbf{v} is the velocity of the radionuclides in the position \mathbf{x} at the time t .

$\left. \frac{\partial}{\partial t} \right|_{\mathbf{x}} \equiv$ spatial time derivate at \mathbf{x} .

$\text{div} \equiv$ divergence operator.

We make the following simplifications and assumptions:

- The atmosphere is well mixed and thus the atmospheric concentration is independent of the spatial variable: $\rho(\mathbf{x}, t) = \rho(t)$.
- The divergence of the velocity field remains constant and positive (there is only deposition). Let us define $\text{div}(\mathbf{v}) = \frac{1}{\tau}$, where τ represents the mean residence time of the nuclide in the atmosphere. We assume τ to be between 1 and 2 years for ^{10}Be .
- The production rate is assumed to be sinusoidal

$$Q(t) = Q_0 \cdot [1 + \alpha \cdot \sin(\omega t)], \quad (\text{A.2})$$

where ω is the angular frequency of the production rate and α is a constant. Note that since the production rate must be a positive number, α must satisfy $0 \leq \alpha < 1$.

- Decay is neglected (^{10}Be is removed from the atmosphere by deposition only).

On these assumptions the equation A.1 transforms into the following equation to be solved:

$$\dot{\rho}(t) = Q(t) - \frac{\rho}{\tau}. \quad (\text{A.3})$$

We impose a restriction on the solution such that $|\rho| \leq \infty$ when $t \rightarrow +\infty$. Then the solution is

$$\rho(t) = \rho_0 \cdot \left[1 + \frac{\alpha}{\sqrt{1 + (\omega \tau)^2}} \sin(\omega t - \phi) \right], \quad (\text{A.4})$$

$$\rho_0 = Q_0 \tau, \quad (\text{A.5})$$

$$\phi = \arctan(\omega \tau), \quad (\text{A.6})$$

where ρ_0 is the mean atmospheric radionuclide concentration. In the next step we analyze and compare the amplitudes of the relative production rate and relative atmospheric concentration, namely

$$\frac{Q(t) - Q_0}{Q_0} = \alpha \sin(\omega t), \quad (\text{A.7})$$

$$\frac{\rho(t) - \rho_0}{\rho_0} = \frac{\alpha}{\sqrt{1 + (\omega \tau)^2}} \sin(\omega t - \phi). \quad (\text{A.8})$$

These equations show that the atmosphere acts as a filter. Since $\omega, \tau \geq 0$, we can deduce from equations A.7 and A.8 that:

1. $\phi = \arctan(\omega \tau) \geq 0 \Rightarrow$ The measured signal has the same frequency as the original but is delayed by ϕ .
2. $\alpha_a \equiv \frac{\alpha}{1 + (\omega \tau)^2} \Rightarrow \alpha_a < \alpha$. The atmospheric concentration displays an amplitude smaller than the amplitude of the original signal. In addition, it can be seen that for a constant frequency ω the atmospheric amplitude decreases with the mean residence time τ . The larger the τ , the smaller the α_a .

Finally, we apply equations A.7 and A.8 to two specific particular cases of sinusoidal ^{10}Be production rate, oscillating with periodicities of 10 and 300 years. In addition, we use the same ^{14}C production rate and use a carbon cycle model (Muscheler 2000) in order to calculate the corresponding $\Delta^{14}\text{C}$. The results are depicted in figures A.1, A.2, A.3 and A.4. These figures illustrate the fact that ^{10}Be shows changes in the production rate more directly than ^{14}C .

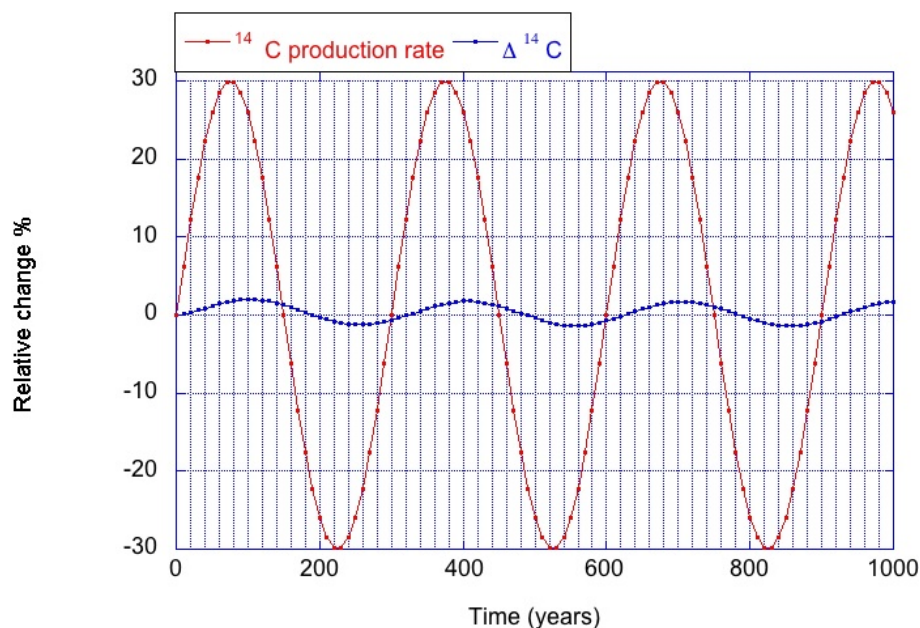


Figure A.1: Relative change of ^{14}C production rate and $\Delta^{14}\text{C}$ against time. The red line depicts a sinusoidal production rate with a periodicity of 300 years. The blue line represents the corresponding atmospheric $\Delta^{14}\text{C}$, which was calculated using a carbon cycle model. The original amplitude is very strongly attenuated. In addition, the $\Delta^{14}\text{C}$ curve is delayed by ~ 25 years.

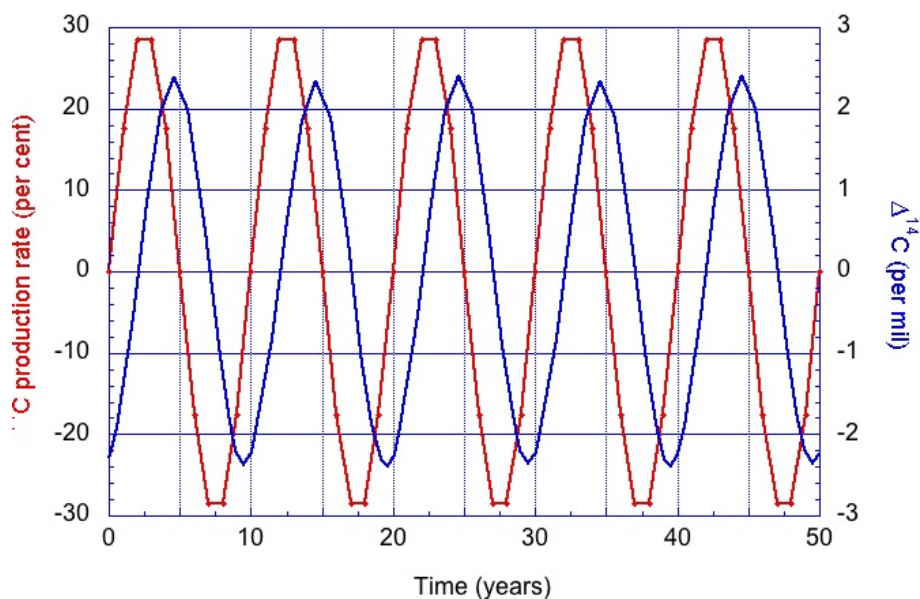


Figure A.2: Relative change of ^{14}C production rate and $\Delta^{14}\text{C}$ against time. The red line depicts a sinusoidal production rate with a periodicity of 10 years. The blue line represents the corresponding atmospheric $\Delta^{14}\text{C}$, which was calculated using a carbon cycle model. The atmospheric amplitude is even more strongly attenuated than in the previous figure. The $\Delta^{14}\text{C}$ curve is delayed ~ 3 years. Note the different scales.

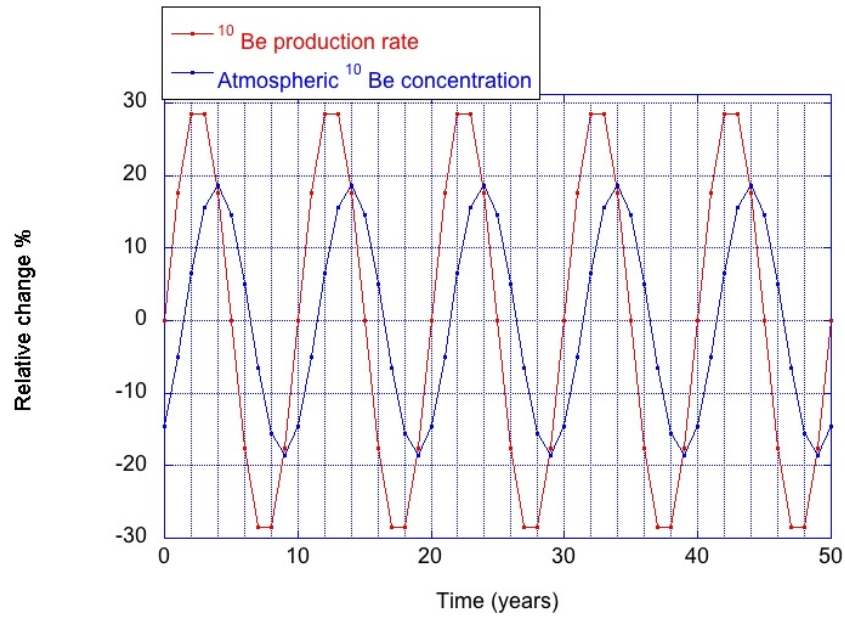


Figure A.3: Relative change of ^{10}Be production rate and atmospheric ^{10}Be concentration against time. The red line depicts a sinusoidal production rate with a periodicity of 10 years. An atmospheric residence time of 2 years for ^{10}Be was assumed. The blue line represents the corresponding atmospheric ^{10}Be concentrations. It can be observed how the amplitude of the atmospheric ^{10}Be concentration is attenuated and delayed by ~ 2 years. However, these two effects for ^{10}Be concentrations are less important than for the ^{14}C concentrations.

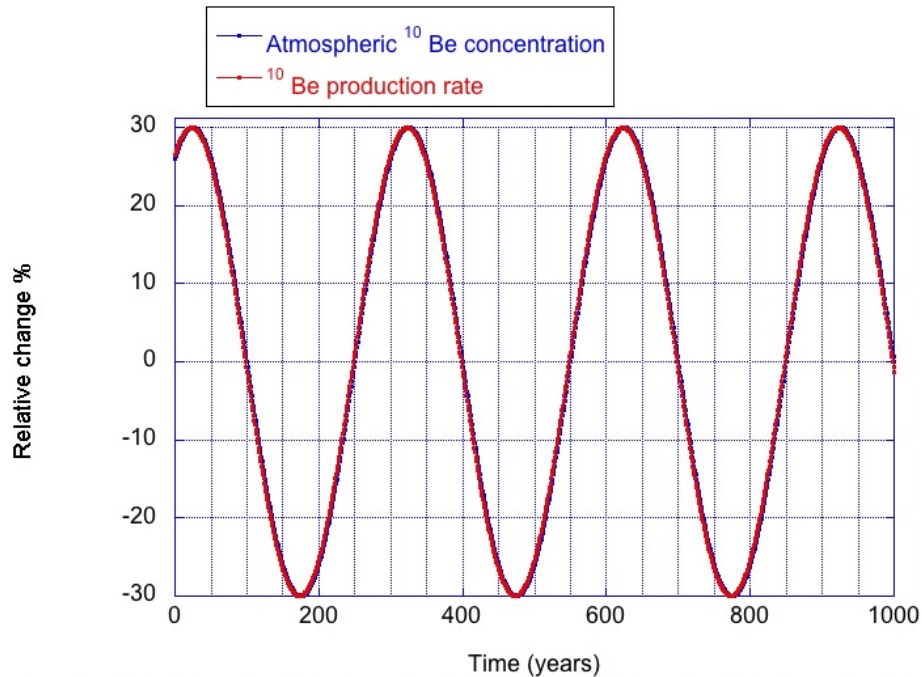


Figure A.4: Relative change of ^{10}Be production rate and atmospheric ^{10}Be concentration against time. The red line depicts a sinusoidal ^{10}Be production rate with a periodicity of 300 years. The blue line represents the corresponding atmospheric ^{10}Be concentration. There are no significant differences between the amplitudes.

Appendix B

Basics on *Principal Component Analysis* (PCA), definitions and notation

On chapter (6) we made use of the method of Principal Components to rewrite three given time series, which were non independent, as linear combination of new set of uncorrelated time series. In this Appendix we briefly explain the PCA method. Each time series represents a set of measurements of a variable X_i on a set of n time points $\{t_j\}$. We may denote by x_{ij} the real value taken by the variable X_i at time t_j . The time series in matrix form is shown in Table (B.1).

Table B.1: Matrix of data

X_i	t_1	t_2	...	t_n
X_1	x_{11}	x_{12}		x_{1n}
X_2	x_{21}	x_{22}		x_{2n}
\vdots	\vdots	\vdots	...	\vdots
X_p	x_{p1}	x_{p2}		x_{pn}

We represent the *matrix of data* in tensorial form as

$$\hat{X} = x_{ij} |e_i \rangle \langle b_j| \quad (\text{B.1})$$

where $|e_i \rangle \in \mathbb{R}^p$ and $|b_j \rangle \in \mathbb{R}^n$ are the canonical basis of the euclidean vectorial spaces \mathbb{R}^p and \mathbb{R}^n , respectively. We represent by $| \rangle$ column vectors and by $\langle |$ their transpose. By $| \rangle \langle |$ we denote the tensorial product.

We will assume that the time series are centered, *i.e.*, they have zero mean¹.

The corresponding *covariance Matrix* is given by

$$\hat{\Gamma} = \frac{1}{n} \hat{X} \hat{X}^t = \Gamma_{ij} |e_i \rangle \langle e_j| \quad (\text{B.2})$$

with $\Gamma_{ij} = \frac{1}{n} \sum_{k=1}^n x_{ik} x_{jk} = \text{Cov}[X_i, X_j]$

¹Otherwise, the must be centered $X_i^c = X_i - E[X_i]/E[X_i] = \frac{1}{n} \sum_{j=1}^n x_{ij}$

point-space: For a given time t_k , the set of p points $\{x_{ik}\}$ can be considered as vectors in the euclidean vectorial space \mathbb{R}^p . We associate to each time t_k a p -dimensional vector

$$|t_k \rangle \equiv \hat{X}^t |b_k \rangle = x_{ij} (|e_i \rangle \langle b_j|) |b_k \rangle = x_{ij} (\langle b_j | b_k \rangle) |e_i \rangle = x_{ik} |e_i \rangle \quad (\text{B.3})$$

where $\{x_{ik}\}$ represents the coordinate of the vector $|t_j \rangle$ on the canonical basis $\{|e_j \rangle\}$ of \mathbb{R}^p , and the scalar product is the ordinary in \mathbb{R}^p . We will refer to this space as *point-space*.

Time-series-space: The set of p time series X_i can be regarded as a non-orthogonal basis of the vectorial subspace \mathbf{V} of the vectorial space of the random variables \mathcal{L}^2 . Since X_i is, in general, a non-orthogonal basis, its dimension is given by the rank of the system $\{X_i\}$, and is $\leq p$. Therefore every vector of \mathbf{V} can be written as:

$$\forall |U \rangle \in \mathbf{V} \quad |U \rangle = \sum_{i=1}^p u_i |X_i \rangle \quad (\text{B.4})$$

The vectorial subspace \mathbf{V} will be referred as *time-series space*. The scalar product in the time-series space is given by:

$$\forall (|U \rangle, |V \rangle) \in \mathbf{V} \quad \langle U | V \rangle = E[U, V] \quad (\text{B.5})$$

The *point-space* and the *time-series-space* are linked by:

1. A linear map F from the point-space to the time-series space as

$$\mathbb{R}^p \xrightarrow{F} \mathbf{V}$$

$$\forall |u \rangle \in \mathbb{R}^p, \quad F(|u \rangle) \equiv \hat{X}^t |u \rangle = |U \rangle = \sum_{i=1}^p u_i |X_i \rangle$$

F associate to every vector of the point-space a vector in the time-series space, i.e, a time-series

2. A bilinear form G

$$\mathbb{R}^p \times \mathbb{R}^p \xrightarrow{G} \mathbb{R}$$

$$\forall (|u \rangle, |v \rangle) \in \mathbb{R}^p \times \mathbb{R}^p, \quad G(|u \rangle, |v \rangle) \equiv \langle u | \hat{\Gamma} | v \rangle \quad (\text{B.6})$$

by definition of scalar product in \mathbf{V} (and if the variables are centered) $\langle u | \hat{\Gamma} | v \rangle = E[U, V] = \text{Cov}[U, V]$. Thus, for every two vectors of the point-space, the bilinear form G give us the covariance between their associated time-series-vectors (by F).

Now we are ready to precisely state the PCA problem. We present the problem under two equivalent approaches. The first one is an statistical approach, since the time-series space is indeed the space of time series

1. We desire to find an orthogonal basis of *time-series space* $\{|C_i \rangle\}$, *i.e.* the corresponding time series are uncorrelated.
2. the variance of each C_i is maximal.

This will allow us to decompose $|X_i\rangle$ in the desired form as:

$$|X_i\rangle = \sum_j \alpha_{ij} |C_j\rangle \tag{B.7}$$

the new time-series vectors are known as the *Principal Components*. By F and G the conditions (1)-(2) can be interpreted in geometrical terms in the point-space. This is the geometrical approach.

1. We desired to find a new basis of \mathbb{R}^p , say $\{|c_i \rangle\}$, so that that basis is orthogonal
2. and the projection of point-vectors $\{|t_i \rangle\}$ in this new basis is maximal.

This is an optimization problem, which can be solved by the method of Lagrange Multipliers. We note that in order to avoid that the optimization becomes trivial, we impose that the basis $\{|c_i \rangle\}$ must be orthonormal. Thus the problem reduces to find the maximum of the function $f(c_m) = \langle c_m | \hat{\Gamma} | c_m \rangle$ under the constraint $\langle c_m | c_m \rangle = 1$.

$$f(c_m) = \langle c_m | \hat{\Gamma} | c_m \rangle - \lambda (\langle c_m | c_m \rangle - 1) \tag{B.8}$$

$$\frac{\partial f}{\partial |c_m \rangle} = 0 \Rightarrow \hat{\Gamma} | c_m \rangle = \lambda | c_m \rangle \tag{B.9}$$

We see that the lagrange multipliers λ are indeed, the eigenvalues of the the covariance matrix! Since $\hat{\Gamma}$ is symmetric, all eigenvalues are real and there exist p eigenvalues with their corresponding eigenvectors, which are an orthonormal basis of \mathbb{R}^p . It is easy to show that the corresponding vectors of the time-series space satisfy the required conditions (1)-(2).

B.1 Properties of the Principal Components

Let us summarize some important properties of the principal components

- the new set of variables C_i explain the same amount variance as the original variables X_i .

$$\begin{aligned} \text{tr}(\hat{\Gamma}) &= \sum_i \lambda_i = \sum_i \text{Var}[X_i] \\ \text{Var}[C_i] &= \langle C_i | C_i \rangle = \langle c_i | \hat{\Gamma} | c_i \rangle = \lambda_i \\ \sum_i \text{Var}[C_i] &= \sum_i \text{Var}[X_i] \end{aligned} \tag{B.10}$$

- The percent of the total of variance explained by component k is given by

$$\frac{\text{Var}[C_k]}{\sum_j \text{Var}[C_j]} = \frac{\lambda_k}{\sum_j \lambda_j} \tag{B.11}$$

- The α_{ij} in eq. (B.7) are given by

$$\alpha_{i,j} = \sigma(X_j) \text{Corr}(C_i, X_j) / \lambda_j^{0.5} \quad (\text{B.12})$$

with $\text{Corr}(C_i, X_j)$ coefficient correlation between Component i and original variable j

Appendix C

Error estimation for Paper: Grand maxima in solar activity

There are two sources of error in the prediction presented in chapter (7). Measurement errors on the one hand, and those introduced by fitting a gamma/lognormal distribution on the other. In chapter (7) we took into account only the fit error. We argued that the errors introduced by fitting a gamma/lognormal distribution are dominant. This is illustrated in Fig. (C.1). The broken green curve depicts the observed distribution of durations. To produce this curve, we fitted a gamma distribution and obtained parameters $a = 2.2$ and $b = 13.1$ and corresponding confident intervals $[1.6, 3]$, $[9, 18.8]$. The red curves A and B represents the corresponding pdf distributions of the extreme intervals, respectively. Then by Monte Carlo technique we simulated 1000 ϕ curves assuming that the measurement errors are normal distributed, so that the solid green curve represents the mean duration (of 1000 runs) in each class interval and the black error bars depict the corresponding $1-\sigma$ deviations. However, a more accurate result can be obtained by taking into account both errors. This is the topic of the next section.

C.1 Measurement error & fit error

The next 1 to 8 steps were repeated 1000 times. They explain the procedure to estimate the error corresponding to the gamma distribution.

1. We started with the tree ϕ reconstructions (Usoskin, McCracken, Vonmoos) say ϕ_1^0 , ϕ_2^0 , ϕ_3^0 and their corresponding measurement errors $\Delta\phi_1^0$, $\Delta\phi_2^0$, $\Delta\phi_3^0$ (60, 40 and 80 MV respectively).
2. Then, by assuming that measurement errors are normal distributed, we generated a new set of time series so that $\phi_i(t) = N(\phi_i^0(t), \Delta\phi_i^0)$.
3. The previous set of three time series were merged to generate a $\phi(t)$ composite.
4. The composite was linearly interpolated to 1y, linearly detrended and band-pass filtered (40-3000)y.
5. Since we found each $\phi \in N(\sigma, \mu)$ we defined boundaries $\phi_{max} = 0.85\sigma + \mu$ $\phi_{min} = -0.85\sigma + \mu$. so that the Sun (or ϕ) spent 20% of the time in *grand maximum* and 20

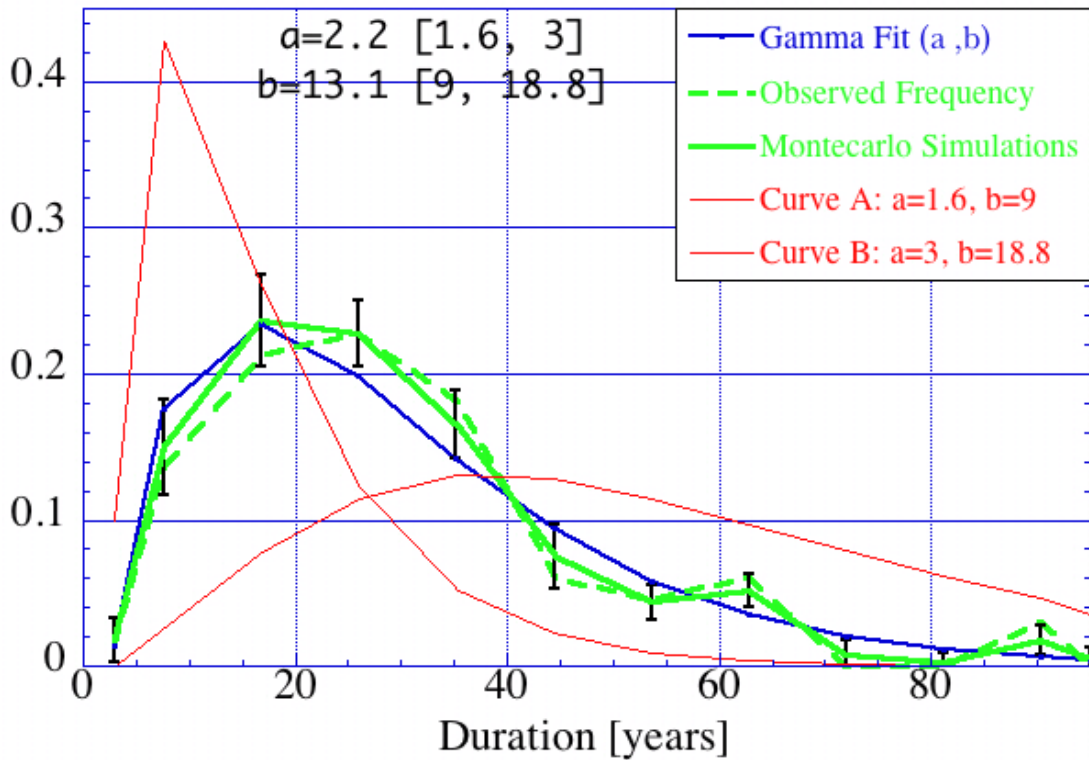


Figure C.1: Blue points represents the best gamma fit with parameters (a,b) . Red curves A and B represents the corresponding gamma distributions by taking as parameters the extreme values $(1.6, 9)$ and $(3, 18.8)$ respectively. The solid green curve, was obtained by assuming that the $\phi(t)$ measurement errors are normal distributed. The black error bars depict the $1-\sigma$ deviations (see explanation in text)

in a *grand minimum* (in case of the published paper $\phi_{min} = 340$ MV). Based on these boundaries we calculate the number of grand maxima, their durations (I will refer to this random variable as \mathcal{M}), as well as the “duration of current maximum” = t_0 ¹.

6. In doing so, we got a distribution of *durations of grand maxima*, *i.e.* \mathcal{M} . Next we proceeded to the fit of a gamma distribution to \mathcal{M} and consider the corresponding *fit error*.

- (a) We fitted a gamma distribution to \mathcal{M} . This distribution depends on two parameters gamma (α, β). The fit was made by the maximum likely hood method. Let be a and b the maximum likely hood values for α, β respectively². In addition we get the corresponding 95% confidence intervals *i.e.* $\alpha \in [a_0, a_1]$, $\beta \in [b_0, b_1]$ I will refer to this in what follows as “fit error”.
- (b) The gamma fitted distribution was used to estimate the life “life expectancy of the current maximum $ex(t_0)$ ” as explained in (7.3). Then we estimate the “remaining time” as $r(t_0) = ex(t_0) - t_0$. Because our prediction depends on the parameters α and β , we must estimate the influence of fit error on our prediction, *i.e.*, $\Delta r(t_0)$ ($\Delta r(t_0)$ follows a new distribution)
- (c) Estimation of the fit errors: Assuming that the parameters are lognormal distributed, in their confidence intervals, *i.e.* $\alpha \in \text{Lognormal}(\mu_a, \sigma_a)$ and $\beta \in \text{Lognormal}(\mu_b, \sigma_b)$ with,

$$\mu_a = \text{Ln}(a), \sigma_a = \text{Ln}\left(\frac{a_1}{a}\right)^{0.5} = -\text{Ln}\left(\frac{a_0}{a}\right)^{0.5}, \quad (\text{C.1})$$

$$\mu_b = \text{Ln}(b), \sigma_b = \text{Ln}\left(\frac{b_1}{b}\right)^{0.5} = -\text{Ln}\left(\frac{b_0}{b}\right)^{0.5}, \quad (\text{C.2})$$

we let the parameters to vary randomly in their confidence intervals and then we calculate the corresponding “remaining time” $r(t_0)$. We repeated this process thousand times.

- (d) This provides us with a distribution of $r(t_0)$ ’s. We found that in 98% $r(t_0)$ is Lognormal distributed. Therefore we choosed as a measure of the error $\Delta r(t_0)$ the standard deviation of that distribution, and as a measure of $r(t_0)$ its mean value, say $\bar{r}(t_0)$.

7. As an output of previous calculations we get thousand distributions for $r(t_0)$, as well as their corresponding $\bar{r}(t_0)$ and $\Delta r(t_0)$.

8. Figure (C.2) depicts the pairs $\{\bar{r}(t_0), \Delta r(t_0)\}$ for each of the thousand runs.

C.2 conclusions

We see from Fig. (C.2) that $\bar{r}(t_0)$ as well $\Delta r(t_0)$ seems to be stationary oscillating around 13 years and 3 years respectively. Note that errors given in chapter (7), which are based on fit errors only, correspond to just 1 run of the 1-8 steps with $\Delta\phi_i^0 = 0$. The resulting

¹Note that the value of t_0 changes with ϕ

²We use the Matlab function `gamfit()`.

distribution of remaining times is depicted in Fig. (C.3). This shows that result given in chapter (7) corresponds to an upper limit and indicates that both errors must be taken into account. Therefore, according to this procedure, we expect that the current maximum will end in ≈ 13 , *i.e.* around 2017, with rms error of about 3 years.

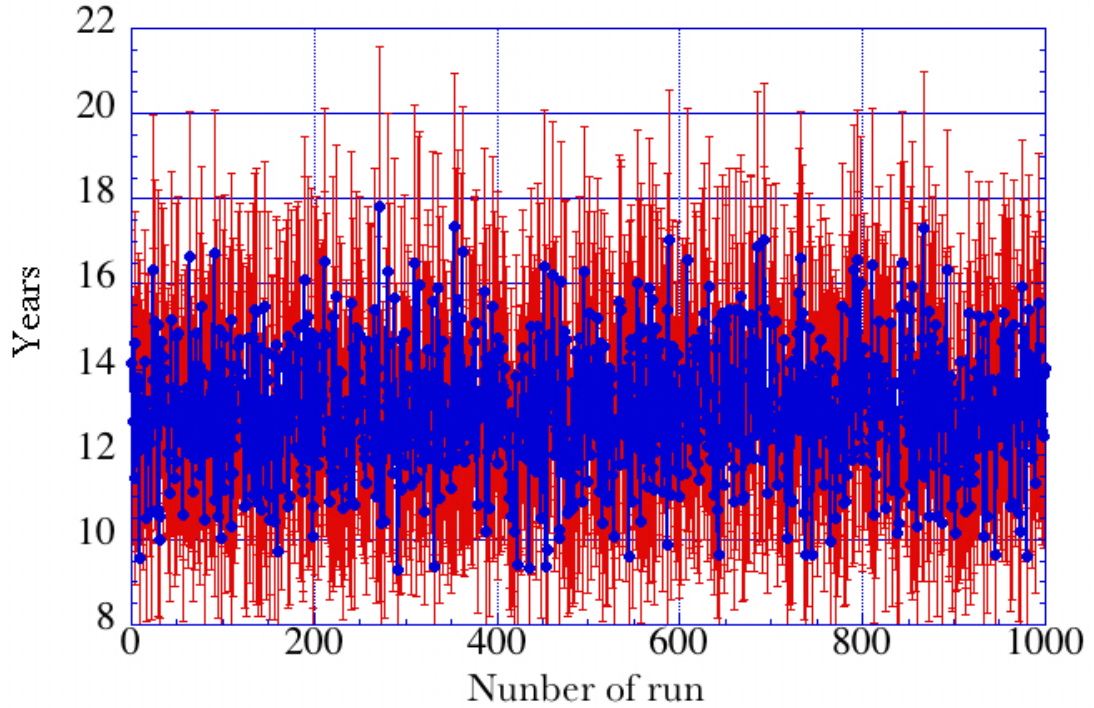


Figure C.2: Blue points depict $\bar{r}(t_0)$ and red error bars depict $\Delta r(t_0)$ for each run

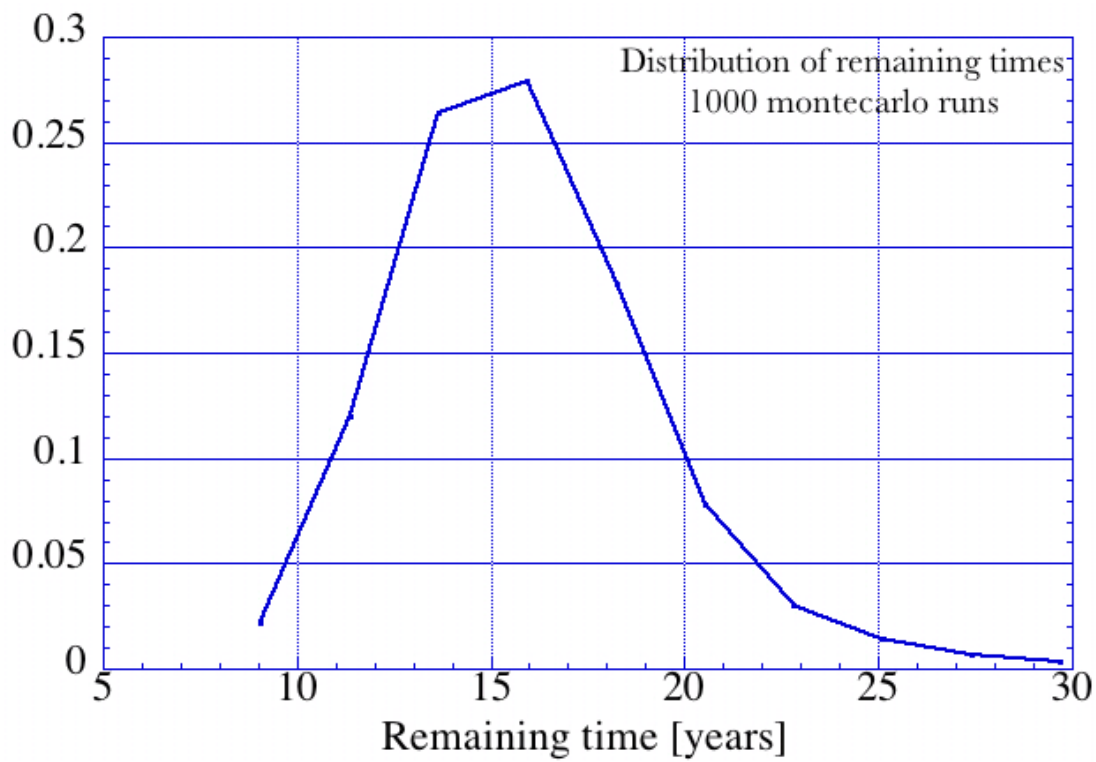


Figure C.3: Distribution of remaining times corresponding to the gamma distribution. The parameters of gamma distribution $a \in [1.60, 3.02]$ and $b \in [9.18, 18.79]$ were assumed to be lognormal distributed in their respective intervals. Here we took into account the fit errors only

Bibliography

- Abreu, J. A., Beer, J., Steinhilber, F., Tobias, S. M., Weiss, N. O. (2008), “For how long will the current grand maximum of solar activity persist?”, *Geophys. Res. Lett.* **35**, L20109.
- Beer, J., Tobias, S., Weiss, N. (1998), “An active Sun throughout the Maunder Minimum”, *Solar Physics* **181**(1), 237–249.
- Beer, J., Mende, W., Stellmacher, R. (2000), “The role of the sun in climate forcing”, *Quat. Sci. Rev.* **19**, 403–415.
- Berger, A. & Loutre, M.F. (1991), “Insolation values for the climate of the last 10 million years”, *Quat. Sci. Rev.* **10**(4), 29–317.
- Berggren, A.-M., Beer, J., Göran Possnert, G., Aldahan, A. A., Kubik, P., Christl, M., Johnsen, S., Abreu-Castañeira, J. A., Vinther, B. (2009), “A 600-year annual ^{10}Be record from the NGRIP ice core, Greenland”, *Geophys. Res. Lett.* **36**(11), CiteID L11801.
- Brandenburg, A. (2005), “The Case for a Distributed Solar Dynamo Shaped by Near-Surface Shear”, *ApJ.* **625**, 539.
- Brandenburg, A. & Spiegel, E. A. (2008), “Modeling a Maunder minimum”, *Astron. Nachr.* **329**, 351–358.
- Bretthorst, G. L. (1988a), “Excerpts from Bayesian Spectrum Analysis and Parameter Estimation”, in *Maximum-Entropy and Bayesian Methods in Science and Engineering*, **1**, G.J. Erickson and C.R. Smith eds., Kluwer Academic Publishers, Dordrecht, Holland, pp. 75–145.
- Bretthorst, G. L. (1988b), “Bayesian Spectrum Analysis and Parameter Estimation”, in *Lecture Notes in Statistics* **48**, Springer-Verlag, New York, New York.
- Bushby, P. J. & Tobias, S. M. (2007), “On predicting the solar cycle using mean-field models”, *ApJ.* **661**, 1289–1296.
- Caballero Lopez, R. & Moraal, H. (2004), “Limitations of the force field equation to describe cosmic ray modulation”, *J. Geophys. Res.* **109**, A01101.
- Caligari, P., Moreno-Insertis, F., Schüssler, M. (1995), “Emerging flux tubes in the solar convection zone. 1: Asymmetry, tilt, and emergence latitude”, *ApJ.* **441**, 886–902.
- Cattaneo, F. (1999), “On the Origin of Magnetic Fields in the Quiet Photosphere”, *ApJ.* **515**, L39–L42.

- Choudhuri, A. R. & Gilman, P. A. (1987), “The influence of the Coriolis force on flux tubes rising through the solar convection zone”, *ApJ*. **316**, 788–800.
- Choudhuri, A. R., Chatterjee, P., Jiang, J. (2007), “Predicting solar cycle 24 with a solar dynamo model”, *Phys. Rev. Lett.* **98**, 131103.
- Clilverd, M. A., Clarke, E., Rishbeth, H., Clark, T. D. G., Ulich, T. (2003), “Solar cycle: Solar activity levels in 2100”, *Astron. Geophys.* **44**(5), 20–22.
- Dansgaard, W. & Johnsen, S. (1969), “A flow model and a time scale for the ice core from Camp Century, Greenland”, *Journal of Glaciology* **8**, 215–223.
- Dikpati, M., de Toma, G., Gilman, P. A. (2006), “Predicting the strength of solar cycle 24 using a flux-transport dynamo-based model”, *Geophys. Res. Lett.* **33**, L05102.
- Ferriz-Mas, A. & Schüssler, M. (1993), “Instabilities of magnetic flux tubes in a stellar convection zone. I. Equatorial flux rings in differentially rotating stars”, *Geophys. Astrophys. Fluid Dynam.* **72**, 209–247.
- Ferriz-Mas, A., Schmitt, D., Schüssler, M. (1994), “A dynamo effect due to instability of magnetic flux tubes”, *Astron. Astrophys.* **289**, 949–956.
- Ferriz-Mas, A. & Schüssler, M. (1995), “Instabilities of magnetic flux tubes in a stellar convection zone. II. Flux rings outside the equatorial plane”, *Geophys. Astrophys. Fluid Dynam.* **81**, 233–265.
- Fröhlich, C. (2000), “Observations of irradiance variability”, *Space Science Reviews* **94**, 15–24.
- Fröhlich, C. (2009), “Evidence of a long-term trend in total solar irradiance”, *Astron. Astrophys.* **501**, L27–L30.
- Fröhlich, C. & Lean, J. (2004), “Solar radiative output and its variability: evidence and mechanisms”, *The Astronomy and Astrophysics Review* **12**, 273–320.
- Galloway, D. J. & Weiss, N. O. (1981), “Convection and magnetic fields in stars”, *ApJ*. **243**, 945–953.
- Gleeson, L. J. & Axford, W. I. (1968), “Solar Modulation of galactic cosmic rays”, *ApJ*. **154**, 1011.
- Godwin, H. (1962), “Half-life of Radiocarbon”, *Nature* **195**, 984.
- Golub, L., Rosner, R., Vaiana, G. S., Weiss, N. O. (1981), “Solar magnetic fields - The generation of emerging flux”, *ApJ*. **243**, 309–316.
- Haigh, J. D. (1994), “The role of stratospheric ozone in modulating the solar radiative forcing of climate”, *Nature* **370**, 544–546.
- Hammer, C. U., Clausen, H. B., Dansgaard, W., Gundestrup, N., Johnsen, S. J., Reeh, N. (1978), “Dating of Greenland ice cores by flow models, isotopes, volcanic debris, and continental dust”, *Journal of Glaciology*, **20**(82), 3–26.

- Hathaway, D. H. & Wilson, R. M. (2006), “Geomagnetic activity indicates large amplitude for sunspot cycle 24”, *Geophys. Res. Lett.* **33**, L18101.
- Hays, J.D., Imbrie, J., Shackleton, N.J. (1976), “Variations in the Earth’s Orbit: Pacesetter of the Ice Ages”, *Science* **194**(4270), 1121–1132.
- Heikkilä, U., Beer, J., Feichter, J. (2008), “Modeling cosmogenic radionuclides ^{10}Be and ^7Be during the Maunder Minimum using the ECHAM5-HAM General Circulation Model”, *Atmos. Chem. Phys.* **8**, 2797–2809.
- Hughen, K. A., Baillie, M. G. L., Bard, E., Beck, J. W., Bertrand, C. J. H., Blackwell, P. G., Buck, C. E., Burr, G. S., Cutler, K. B., Damon, P. E., Edwards, R. L., Fairbanks, R. G., Friedrich, M., Guilderson, T. P., Kromer, B., McCormac, G., Manning, S., Ramsey, C. B., Reimer, P. J., Reimer, R. W., Remmele, S., Southon, J. R., Stuiver, M., Talamo, S., Taylor, F. W., Plicht, J. V., Weyhenmeyer, C. E. (2004), “Marine04 Marine Radiocarbon Age Calibration, 0–26 Cal Kyr BP”, *Radiocarbon* **46**(3), 1059–1086.
- Imbrie, J. (1993), SPECMAP Archive #4., NOAA/NGDC Paleoclimatology Program, Boulder CO, USA.
- Jensen, E. (1955), “On tubes of magnetic forces embedded in stellar material”, *Ann. d’Astrophys.* **18**, 127.
- Lean, J., Beer, J., Bradley, R. (1995), “Reconstruction of Solar Irradiance Since 1610: Implications for Climate Change”, *Geophys. Res. Lett.* **22**(23), 3195–3198.
- Lockwood, M., & Fröhlich, C. (2007), “Recent oppositely-directed trends in solar climate forcings and the global mean surface air temperature”, *Proc. R. Soc. Lond. A* **463**, 2447–2460.
- Lundstedt, H. (2006), “Solar activity modelled and forecasted: a new approach”, *Adv. Space Res.* **38**, 862–867.
- Masarik, J. & Beer, J. (1999), “Simulation of Particle Fluxes and Cosmogenic Nuclide Production in the Earth’s Atmosphere”, *J. Geophys. Res.* **104**(D10), 12 099–12 111.
- Masarik, J. & Beer, J. (2009), “An updated simulation of particle fluxes and cosmogenic nuclide production in the Earth’s atmosphere”, *J. Geophys. Res.* **114**, D11103.
- McCracken, K. G., McDonald, F., Beer, J., Raisbeck, G., Yiou, F. (2004), “A phenomenological study of the long-term cosmic ray modulation, 850–1958 AD”, *J. Geophys. Res.* **109**, A12103.
- Moreno-Inseris, F., Caligari, P., Schüssler, M. (1995), ““Explosion” and Intensification of Magnetic Flux Tubes”, *ApJ.* **452**, 894.
- Muscheler, R. (2000), *Nachweis von Änderungen im Kohlenstoffkreislauf durch Vergleich der Radionuklide ^{10}Be , ^{36}Cl und ^{14}C* , Diss. ETH Nr. 13941.
- Muscheler, R., Beer, J., Kubik, P., Synal, H.-A. (2005), “Geomagnetic field intensity during the last 60,000 years based on ^{10}Be and ^{36}Cl from the Summit ice cores and ^{14}C ”, *Quat. Sci. Rev.* **16–17**(24), 1849–1860.

- Oeschger, H., Siegenthaler, U., Gugelmann, A. (1975), "A box diffusion model to study the carbon dioxide exchange in nature", *Tellus* **27**(2), 168–192.
- Parker, E. N. (1955a), "The Formation of Sunspots from the Solar Toroidal Field", *ApJ.* **121**, 491.
- Parker, E. N. (1955b), "Hydromagnetic Dynamo Models", *ApJ.* **121**, 293.
- Parker, E. N. (1965), "The passage of energetic particles through interplanetary space", *Planet. Space Sci.* **13**, 9.
- Parker, E. N. (1975), "The generation of magnetic fields in astrophysical bodies. X - Magnetic buoyancy and the solar dynamo", *ApJ.* **198**, 205–209.
- Peixoto, J. P. & Oort, A. H. (1992). *Physics of climate*, New York: American Institute of Physics.
- Peristykh, A. N. & Damon, P. E. (2003), "Persistence of the Gleissberg 88-year solar cycle over the last $\sim 12,000$ years: Evidence from cosmogenic isotopes", *J. Geophys. Res.* **108**(A1), 1003.
- Reimer, P.J., Baillie, M. G. L., Bard, E., Bayliss, A., Beck, J. W., Bertrand, C. J. H., Blackwell, P. G., Buck, C. E., Burr, G. S., Cutler, K. B., Damon, P. E., Edwards, R. L., Fairbanks, R. G., Friedrich, M., Guilderson, T. P., Hogg, A. G., Hughen, K. A., Kromer, B., McCormac, G., Manning, S., Ramsey, C. B., Reimer, R. W., Remmele, S., Southon, J. R., Stuiver, M., Talamo, S., Taylor, F. W., Plicht, J. V., Weyhenmeyer, C. E. (2004), "INTCAL04 terrestrial radiocarbon age calibration, 0-26 cal kyr BP", *Radiocarbon* **46**(3), 1029–1059.
- Ribes, J. C. & Nesme-Ribes, E. (1993), "The solar sunspot cycle in the Maunder minimum AD 1645 to AD 1715", *Astron. Astrophys.* **276**, 549–563.
- Rind, D. & Overpeck, J. (1993), "Hypothesized causes of decade-to-century climate variability: Climate model results", *Quat. Sci. Rev.* **12**, 357–374.
- Ruth, U., Barnola, J.-M., Beer, J., Bigler, M., Blunier, T., Castellano, E., Fischer, H., Fundel, F., Huybrechts, P., Kaufmann, P., Kipfstuhl, S., Lambrecht, A., Morganti, A., Oerter, H., Parrenin, F., Rybak, O., Severi, M., Udisti, R., Wilhelms, F., Wolff, E. (2007), "EDML: a chronology for the EPICA deep ice core from Dronning Maud Land, Antarctica, over the last 150 000 years", *Climate of the Past* **3**, 75–84.
- Ryan, D. A. & Sarson, G. R. (2007), "Are geomagnetic field reversals controlled by turbulence within the Earth's core?", *Geophys. Res. Lett.* **34**, L02307.
- Schatten, K. (2005), "Fair space weather for solar cycle 24", *Geophys. Res. Lett.* **32**, L21106.
- Schmitt, D., Schüssler, M., Ferriz-Mas, A. (1996), "Intermittent solar activity by an on-off dynamo", *Astron. Astrophys.* **311**, L1–L4 .

Schmitt, D., Schüssler, M., Ferriz-Mas, A. (1998), “Variability of Solar and Stellar Activity by Two Interacting Hydromagnetic Dynamos”, ASP Conf. Ser. 154, The Tenth Cambridge Workshop on Cool Stars, Stellar Systems and the Sun, Edited by R. A. Donahue and J. A. Bookbinder, p. 1324.

Schmitt, D. & Ferriz-Mas, A. (2003), “Variable Solar and Stellar Activity by a Flux Tube Dynamo”, In: *Contributions to NATO Advanced Research Workshop Turbulence, Waves, and Instabilities in the Solar Plasma; Hungary, 16-20 September 2002; Publications of the Astronomy Department of the Eötvös University (PADEU)*. Edited by E. Forgács-Dajka, K. Petrovay and R. Erdélyi, 2003, ISBN 963 463 557, **13**, 89.

Schüssler, M. (1983), in *Solar and Stellar Magnetic Fields: Origins and Coronal Effects*, Stenflo J. O. (ed), ESA, SP-220, 67.

Schüssler, M. (2007), “Are solar cycles predicatable?”, *Astron. Nachr.* **328**, 1087.

Schüssler, M. & Ferriz-Mas, A. (2003), in *Advances in nonlinear Dynamos*, eds. A. Ferriz-Mas and M. Núñez, Taylor & Francis (chapter 5).

Sello, S. (2001), “Solar cycle forecasting: A nonlinear dynamics approach”, *Astron. Astrophys.* **377**, 312-320.

Siegenthaler, U., Heimann, M., Oeschger, H. (1980), “ ^{14}C variations caused by changes in the global carbon cycle”, *Tellus* **27**(2), 168–192.

Solanki, S. K., Usoskin, I. G., Kromer, B., Schüssler, M., Beer, J. (2004), “Unusual activity of the Sun during recent decades compared to the previous 11,000 years”, *Nature* **431**, 1084–1087.

Spiegel, E. & Weiss, N. O. (1980), “Magnetic activity and variations in solar luminosity”, *Nature* **287**, 616–617.

Steinhilber, F., Abreu, J. A., Beer, J. (2008), “Solar modulation during the Holocene”, *Astrophys. Space Sci. Trans.* **4**, 1–6.

Steinhilber, F., Beer, J., Fröhlich, C. (2009), “Total solar irradiance during the Holocene”, *Geophys. Res. Lett.* **36**, L19704.

Stuiver, M. & Polach, H. A. (1977), “Discussion Reporting of ^{14}C Data”, *Radiocarbon* **19**(3), 355–363.

Stuiver, M. & Braziunas, T. F. (1988), “The solar component of the atmospheric ^{14}C record”, in *Secular Solar and Geomagnetic Variations in the Last 10,000 Years*, edited by F. R. Stephenson & A. W. Wolfendale, Springer, New York, pp. 245–266.

Tobias, S. M., Weiss, N. O., Beer, J. (2004), “Long-term prediction of solar activity”, *Astron. Geophys.* **45**, 2.6.

Tobias, S. M. & Weiss, N. O. (2007), “Stellar dynamos”, in *Mathematical Aspects of Natural Dynamos*, edited by E. Dormy and A. M. Soward, pp. 281–311, CRC Press, Baton Rouge.

- Usoskin, I. G., Alanko-Huotari, K., Kovaltsov, G. A., Mursula, K. (2005), “Heliospheric modulation of cosmic rays: monthly reconstruction for 1951–2004”, *J. Geophys. Res.* **110**, A12108.
- Usoskin, I. G., Solanki, S. K., Korte, M. (2006), “Solar activity reconstructed over the last 7000 years: The influence of geomagnetic field changes”, *Geophys. Res. Lett.* **33**, L08103.
- Usoskin, I. G., Solanki, S. K., Kovaltsov, G. A. (2007), “Grand minima and maxima of solar activity: new observational constraints”, *Astron. Astrophys.* **471**, 301–309.
- van Ballegooijen, A. A. (1982), “The overshoot layer at the base of the solar convective zone and the problem of magnetic flux storage”, *Astron. Astrophys.* **113**, 99–112.
- Vogt, S., Herzog, G. F., Reedy, R. C. (1990). “Cosmogenic nuclides in extraterrestrial materials”, *Reviews of Geophysics* **28**, 253–275.
- Vonmoos, M., Beer, J., Muscheler R. (2006), “Large variations in Holocene solar activity: constraints from ^{10}Be in the Greenland Ice Core Project ice core”, *J. Geophys. Res.* **111**, A10105.
- Wanner, H., Beer, J., Bütikofer, J., Crowley, T. J., Cubasch, U., Flückiger, J., Goosse, H., Grosjean, M., Joos, F., Kaplan, J. O., Küttel, M., Müller, S. A., Prentice, I. C., Solomina, O., Stocker, T. F., Tarasov, P., Wagner, M., Widmann, M. (2008), “Mid- to Late Holocene climate change: an overview”, *Quat. Sci. Rev.*, **27**(19–20), 1791–1828.
- Willson, R. C., Janssen, M., Chapman, G. A. (1981), “Observations of solar irradiance variability”, *Science* **211**, 700-702.

Acknowledgements

An erster Stelle möchte ich mich bei meinem Doktorvater Prof. Jürg Beer herzlich bedanken. Er hat mir die Chance gegeben, an diesem spannenden Projekt teilzunehmen. Von seinen Ideen habe ich mich immer inspirieren lassen. Ohne die wäre diese Arbeit einfach nicht möglich gewesen. Immer wenn ich Fragen oder Probleme hatte, hatte er für mich Zeit. Es war ein Vergnügen mit ihm lange Diskussionen über die Physik zu führen.

Mein grösster Dank geht an Prof. Antonio Ferriz Mass. Seine Vorlesungen an der Uni waren aussergewöhnlich ausführlich. Er hat uns mit grösster Eleganz die schwierigsten Konzepte der Physik beigebracht. Er hat mich immer unterstützt und er ist auch Schuld, dass ich in die Schweiz gekommen bin, da er mich in Kontakt mit Prof. Jürg Beer gebracht hat.

Ebenso möchte ich meinen BürokollegInnen Ulla Heikkilä und Friedhelm Steinhilber ganz herzlich danken. Es war immer eine Freude mit ihnen das Büro zu teilen. Ulla hat mir stets bei meiner Arbeit sowie mit der deutschen Sprache geholfen und Friedhelm mit seiner guten Laune und seiner äusserst grossen Hilfsbereitschaft. Er hat meine Entwürfe immer rasch durchgelesen und nützliche Vorschläge gemacht. Mit den beiden habe ich auch die wunderschöne Schweiz entdeckt und genossen. Dank an euch beide.

Stickstoff nicht vergessen! Danke an Erwin Grieder, Irene Brunner und Silvia Bollhalder für die Einführung ins "Schwizerdütsch". Es war eine Freude mit Erwin auf die Probenahme gehen, die Schweiz kennenzulernen und ein "Gipfeli" ein bei einem gemütlichen Kaffee zu geniessen. Irene und Silvia danke ich, für Ihre sorgfältige Laborarbeit bei der Probenaufbereitung. Auch wenn ihre Namen nicht auf den Papers stehen, hinter jeder einzigen theoretischen Aufrechnung versteckt sich ihre ausgezeichnete Arbeit.

Dank gilt Peter Kubik, Marcus Christl, Vasili Alfimov und Hans-Arno Synal, die an der ETH Höggerberg für die ^{10}Be und ^{36}Cl Messungen verantwortlich sind. Ich möchte ihnen so wie allen anderen DoktorandInnen und Mitarbeitenden der Gruppe ganz herzlich danken für die geleisteten Tages- und Nachtschichten.

An dieser Stelle möchte ich mich bei allen anderen Kollegen an der EAWAG bedanken die mir auf irgendeiner Art und Weise geholfen haben. Besonders erwähnen möchte ich Alex, Petra, Mathias, Michi, Matteo, Lukas und Flavio. Die Stimmung auf dem ganzen D-Stock im Bürogebäude der EAWAG war sehr angenehm.

Im privaten Bereich möchte ich natürlich an erster Stelle meinen Eltern danken, Argentina und Roberto. Ohne Sie wäre die ganze Arbeit wirklich gar nicht möglich!

Non quixera rematar este traballo sen adicar unhas agarimosas palabras na minha lingua nai á minha familia. Este traballo adícolho aos meus pais Argentina e Roberto. Esquecer non hei tampouco aos meus irmáns, Rober, Bea e Davi, aínda que lonxe, sempre os levo connigo. Desexo rematar lembrando á minha avoa Carme, quen xa se atopa na ilha en compañía dos seus devanceiros. Prométoche que non che han faltar nunca as castanhas nen o vinho novo sempre que nos venhas visitar, garda das nosas tradicións, líder do meu clán!

Gallaecia Fulget

CURRICULUM VITAE

JOSÉ ÁNGEL ABREU CASTIÑEIRA

9/1991–06/1995 Secondary Education, consisting of a three-year baccalaureate and one pre-university year at Gonzalo Torrente Ballester School, Pontevedra, Galiza.

10/1995–07/2001 Five-year MPhys (*Licenciatura en Física*) at the University of Vigo, Ourense, Galiza.
Specialization: Atmospheric and Environmental Physics

05/2004–05/2009 PhD student at the EAWAG in the Department of Surface Waters in the Department of Environmental Sciences of the ETH Zurich.

Title of PhD Thesis:

^{10}Be in polar ice cores and ^{14}C in tree rings: Separation of production and system effects, comparison with past climate changes and implications for solarphysics
under the supervision of Prof. Dr. Jürg Beer.